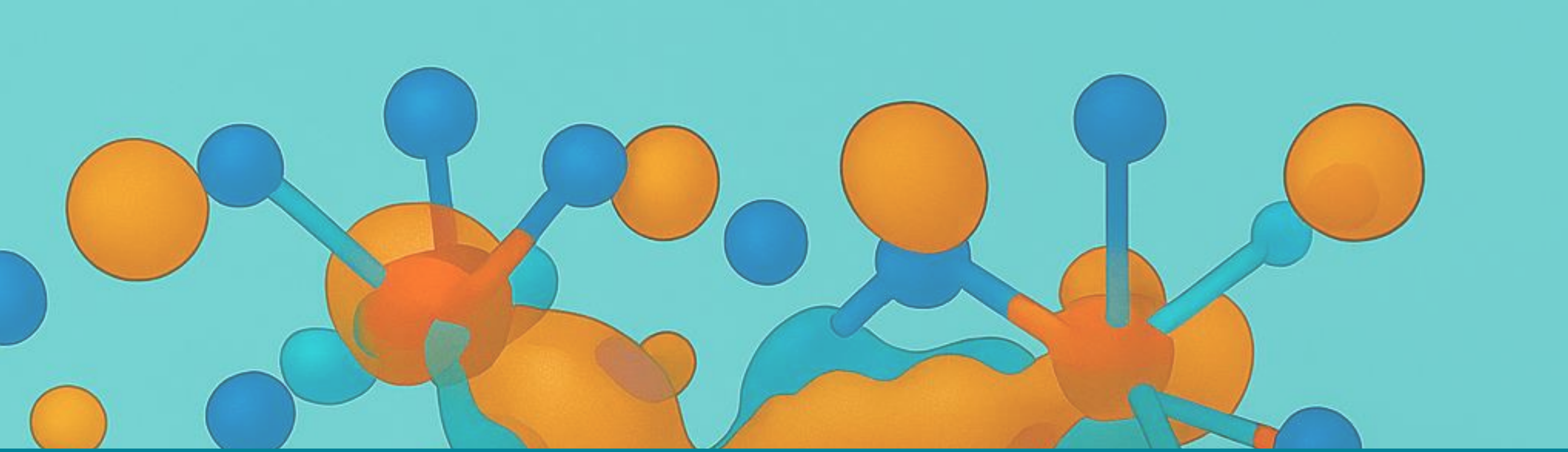

Engineering Low-Potential Stability in Zirconium(IV)-Based Halide Solid Electrolytes

Alinda Dersjant

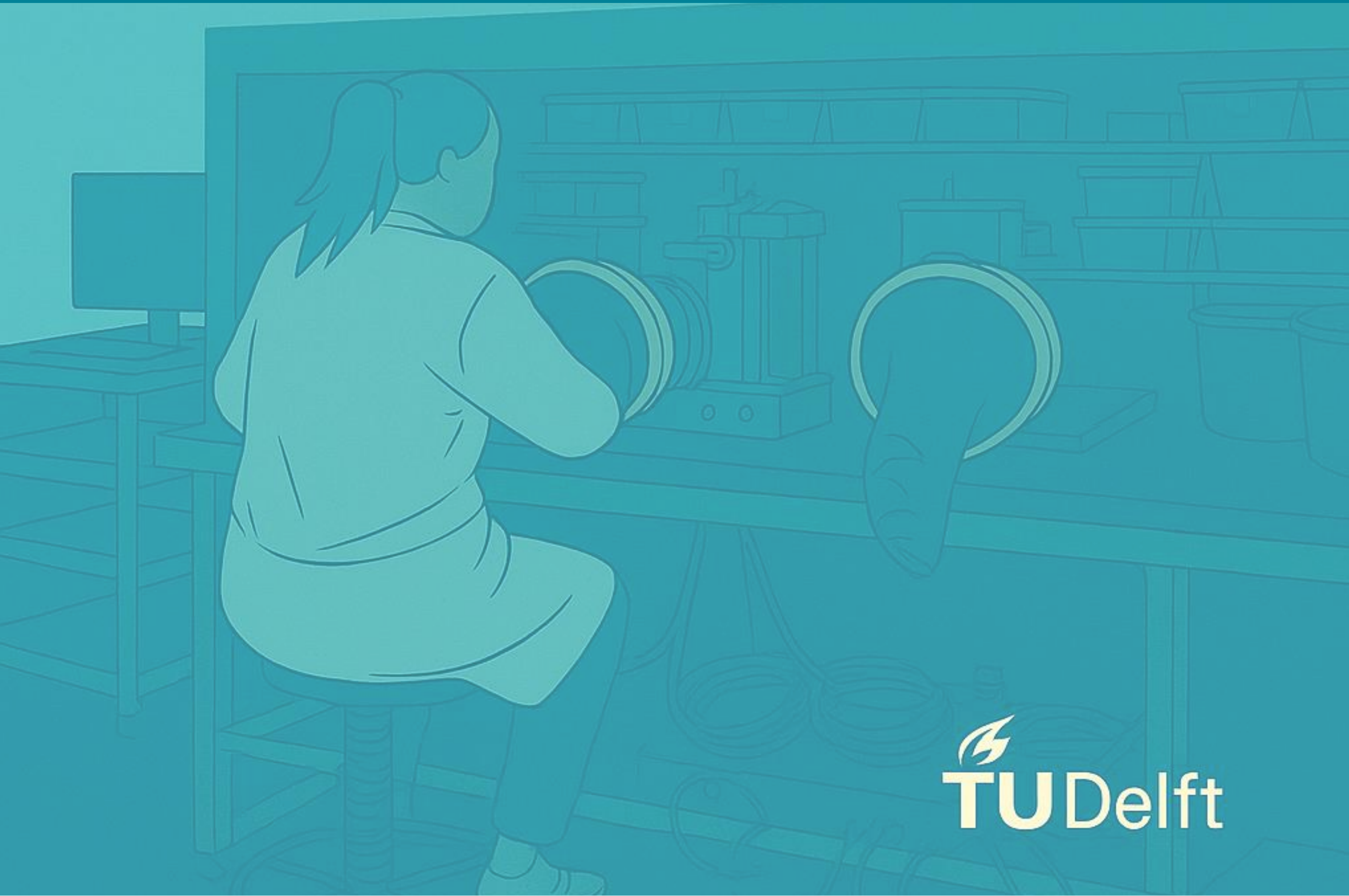

Engineering Low-Potential Stability in Zirconium(IV)-Based Halide Solid Electrolytes

by

Alinda Dersjant

to obtain the degree of Master of Science
at the Delft University of Technology,
to be defended publicly on Thursday June 26, 2025 at 13:30.

Student number:	5568056	
Project duration:	September, 2024 – June, 2025	
Thesis committee:	Prof. dr. ir. M. Wagemaker,	TU Delft, supervisor
	Dr. A. Vasileiadis,	TU Delft, daily supervisor
	Dr. Z. Cheng,	TU Delft, daily supervisor
	Dr. S. Ganapathy,	TU Delft
	Dr. S. Eijt,	TU Delft

Abstract

Solid-state batteries are a promising next-generation energy storage technology due to their improved safety and potential for higher energy density–especially when paired with high-capacity anodes such as lithium metal. However, many solid electrolytes suffer from instability at the low operating potentials of these next-generation anodes, leading to irreversible capacity loss. This challenge is particularly relevant for halide electrolytes, which, despite their good cathodic stability and high ionic conductivity, often exhibit poor anodic stability. The incorporation of zirconium has been shown to enhance ionic conductivity, but its influence on low-potential electrochemical stability remains insufficiently explored.

In this work, we address this gap by engineering zirconium(IV)-based halide electrolytes and studying their behaviour across three distinct chemical environments: (i) an isolated zirconium system (Li_2ZrCl_6), (ii) an aliovalently substituted compound ($Li_{2.5}In_{0.5}Zr_{0.5}Cl_6$), and (iii) a multi-cation high-entropy compound ($Li_{2.75}MCl_6$, M = Sc, Lu, Yb, Zr). Using density functional theory (DFT) and *ab initio* molecular dynamics (AIMD) simulations, we predict electrochemical behaviour at low voltages and validate our predictions experimentally. We distinguish between the intrinsic electrochemical stability window, where no redox activity occurs, and an extended lithiation/delithiation region, where redox activity can proceed without structural decomposition.

Our findings show that Li_2ZrCl_6 exhibits such reversible redox activity beyond its intrinsic stability window, offering enhanced compatibility with low-voltage anodes and additional storage capacity. However, this beneficial behaviour does not translate to the other systems: $Li_{2.5}In_{0.5}Zr_{0.5}Cl_6$ undergoes decomposition via the formation of metallic indium, while the multi-cation compound exhibits severe capacity loss in practice, despite being computationally predicted to resist destructive reduction. This discrepancy between theoretical predictions and experimental outcomes highlights the challenges of modelling complex chemistries and underscores the need for rigorous experimental validation.

Overall, this work lays the groundwork for understanding how zirconium influences redox behaviour in halide electrolytes and reveals the complex interplay between composition, structure, and electrochemical stability–guiding future strategies for the design of reduction-tolerant solid electrolytes.

Acknowledgements

Thanks to Zhu for setting me up to master the skill of working in a glovebox, and teaching me to be patient during the often tedious journey of experimental discovery.

To Alexandros for introducing me to the magical world of computational chemistry, and to push me to always dig deeper for conclusions without losing the big picture out of sight.

To Anastasiia for answering all of my dumb questions and guiding me around my first computations with immense patience.

To my housemates and friends for keeping me sane by always giving me a reason to laugh out loud.

To my parents for never being too busy to provide me with a listening ear.

Contents

Nomenclature

Listed in alphabetical order.

Abbreviation	Defenition
AIMD	(Ab initio) molecular dynamics
BM	Ball-milling
BG	Band gap
CBM	Conduction band minimum
ccp	Cubic close-packed
CV	Cyclic voltammetry
DC	Direct current
DFT	Density Functional Theory
DOS	Density of states
EIS	Electrochemical impedance spectroscopy
ESW	Electrochemical stability window
GGA	Generalised gradient approximation
H4	$Li_{2.75}Sc_{0.25}Zr_{0.25}Yb_{0.25}Lu_{0.25}Cl_6$
H5	$Li_{2.8}Sc_{0.2}Zr_{0.2}Yb_{0.2}Lu_{0.2}In_{0.2}Cl_6$
hcp	Hexagonal close-packed
HG	Hand-ground
HOMO	Highest occupied molecular orbital
LDA	Local density approximation
LIC	Li_3InCl_6
LIZC	$Li_{2.5}In_{0.5}Zr_{0.5}Cl_6$
LPSC	Li_6PS_5Cl, argyrodite
LZC	Li_2ZrCl_6
LSV	Linear-sweep voltammetry
LUMO	Lowest unoccupied molecular orbital
PAW	Projected augmented wave
PBE	Perdew-Burke-Ernzerhof
PBEsol	Perdew-Burke-Ernzerhof adapted for solids
PEIS	Potentiostatic electrochemical impedance spectroscopy
RDF	Radial distribution function
Redox	Reduction-oxidation
SCF	Self-consistent field
SEI	Solid electrolyte interface
SSB	Solid-state battery
SE	Solid electrolyte
VASP	Vienna Ab initio Simulation Package
VBM	Valence band maximum
VGCF	Vapour growth carbon fibre
XRD	X-ray diffraction

1

Introduction

1.1. The need for energy storage

The large-scale burning of fossil fuels since the onset of the Industrial Revolution in the 18th century has enabled a rapid increase in energy demand, accompanied by a corresponding rise in carbon dioxide emissions. The result is an overall increase in global temperatures with devastating effects to humanity and the environment. Severe drought episodes have doubled over the recent decades, while heavy precipitation events are becoming increasingly more common[1]. Further, as oceans warm and land ice melts, coastal areas face increasing threats from flooding and erosion. Meanwhile, nature struggles to keep up with the rapid environmental changes, resulting in a decline of biodiversity and loss of vulnerable ecosystems[2]. In order to minimise further environmental damage, a sequel is required to the Industrial Revolution, namely a shift from fossil fuels to renewable energy sources: the energy transition[1],[3].

Anno 2024, fossil fuels still supply 80 percent of global energy demand[3]. Increasing the portion of renewable energy relies on the implementation of storage techniques such as batteries, which accommodate for the intermittent nature of wind and solar power. A larger energy storage capacity is thus required to achieve grid stability and energy security. In addition, the transport sector, responsible for roughly a quarter of global CO_2 emissions, is especially dependent on batteries for electrification[1]. In fact, 90 percent of batteries end up in electric vehicles and it is expected that this remains true until at least 2030[4].

1.2. Solid-state batteries and halide solid electrolytes

To date, lithium-ion batteries have dominated the market of electric vehicles and portable electronics, owing to their long cycle life, relatively high energy density and reasonable cost[4]. However, their flammable liquid electrolyte continues to be a safety concern and the improvement in energy density appears to stagnate[4],[5]. Replacing the flammable liquid electrolyte by a solid version has given birth to the solid-state battery (SSB) with improved inherent safety. In addition, the SSB promises a higher energy density, especially when made compatible with high-capacity anodes[6].

Different solid electrolyte (SE) chemistries have been explored, including oxide-, sulphide-, and halide-based. The latter has received increasingly more traction over the past years owing to its good lithium-ion conductivity, scaling potential and excellent oxidation stability, as can be observed from Figure 1.1[7].

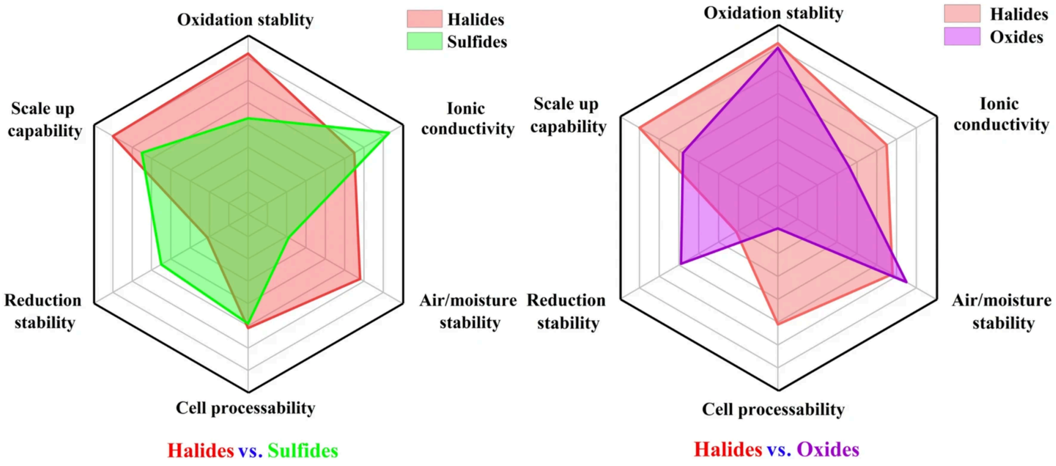

Figure 1.1: Spider plot comparing the performance of various solid electrolyte chemistries (halides, sulphides, and oxides). Reproduced from Tuo *et al.* [8]

Within the family of halide SEs, zirconium is commonly incorporated, as it has been shown to enhance lithium-ion conductivity and oxidation stability–an effect largely attributed to its tetravalent state (Zr^{4+}) in contrast to the more commonly used trivalent cations (M^{3+})[9],[10]. Moreover, recent computational work within the research group has indicated that zirconium(IV)-based halide SEs can show excellent reduction stability. This is of great importance, since reduction stability, i.e. stability against the low potentials at the anode, is generally poor in halide-based SEs (see Figure 1.1).

1.3. Goals of this work

This work aims to answer the following research question:

How does the incorporation of zirconium(IV) affect the low-potential stability of halide monoclinic solid electrolytes?

To answer this research question, three distinct zirconium-based halide electrolytes were engineered and were studied under low-potential conditions. The study begins with monoclinic Li_2ZrCl_6, representing an isolated zirconium system. It then progresses to studying the aliovalently substituted compound $Li_{2.5}In_{0.5}Zr_{0.5}Cl_6$. Finally, zirconium is incorporated into a high-entropy, multi-cation environment to assess its effect in a more complex configuration.

1.4. Methodology

The research question is answered through a combination of computational and experimental methods. Computationally, density function theory (DFT) and *ab initio* molecular dynamics (AIMD) are deployed to predict electrochemical stability windows. On the experimental side, zirconium(IV)-based SEs are first synthesized by means of ball-milling and annealing. Galvanostatic discharge is employed to evaluate electrochemical stability windows, while electrochemical impedance spectroscopy (EIS) and direct current (DC) polarisation find values for ionic and electronic conductivity, respectively. In addition, X-ray diffraction (XRD) is used to confirm structure and phase composition, providing insights into material stability and decomposition products.

Experimental and computational methods are thus combined to evaluate the behaviour at low potentials of zirconium(IV)-based SEs. To support this investigation, Chapter 2 first provides a theoretical background, covering solid-state batteries, halide solid electrolytes, the electrochemical stability window, and the computational foundations of the study. Next, Chapter 3 explains the applied methodologies, providing computational specifications and experimental set-ups. Chapter 4 presents the results and discusses them within the broader context of existing literature. Finally, Chapter 5 provides conclusions and offers recommendations for future research.

2

Theoretical Background

2.1. Working principle of (solid-state) batteries

A battery is a device that stores chemical energy, which can be converted to electrical energy by means of chemical reactions. It consists of three main parts: the electrodes (i.e. the anode and the cathode), and the ion-transporting electrolyte. The driving force of the battery is the difference in chemical potential between the anode and the cathode. The anode has a high chemical potential and thus releases its electrons easily. The opposite is true for the cathode: its low chemical potential leads to electrons being accepted very easily. Upon discharge, electrons are thus naturally freed at the anode, generating ions within the battery that travel through the electrolyte to the cathode. The electrons travel to the cathode through the external circuit, generating an electrical current. The driving force of the current is thus the energetically favourable movement of electrons from the high chemical potential region at the anode to the low chemical potential region at the cathode. A schematic overview is provided in Figure 2.1.

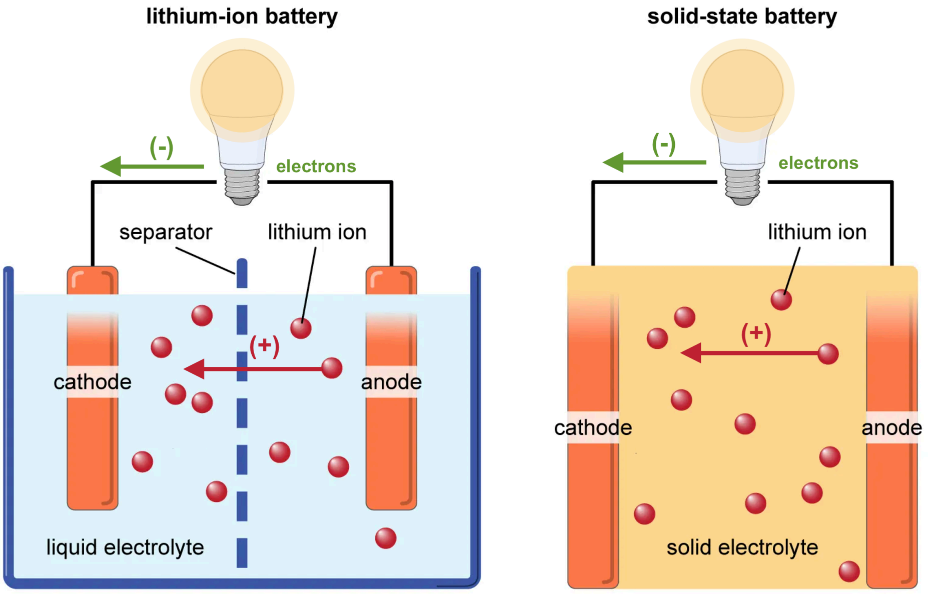

Figure 2.1: The working principle of a battery. Left: A conventional lithium-ion battery with a liquid electrolyte. Right: a solid-state battery. Both batteries are depicted during discharge. The direction of electrons and lithium ions is reversed upon charging. Adapted from Maas *et al.* [10].

Over 90 percent of the batteries currently in use are based on lithium-ion technology, of which the vast majority use a liquid electrolyte[4]. However, there are major safety concerns regarding this flammable liquid electrolyte. Batteries caused 6 percent of house fires in 2023 in the Netherlands–an increase of 50 percent with respect to 2022[11]. These safety concerns combined with the ongoing quest for higher energy densities have led to the exploration of the application of solids as electrolytes in batteries. The resulting batteries not only have a solid anode and cathode, but also a solid electrolyte (SE), as shown in Figure 2.1.

Like liquid electrolytes, these candidates must first demonstrate good ionic conduction ($>10^{-4}$ S/cm) to enable facile lithium-ion transport[12]. In addition, electrolytes need to be electrically resistive–with electronic conductivity ideally under 10^{-10} S/cm–to prevent self-discharge and limit structural breakdown[13]. Furthermore, the electrolyte must be electrochemically stable at the electrolyte-electrode interfaces within their respective working potential ranges to prevent decomposition.

Three main types of solid electrolytes have been explored: organic polymer-based, inorganic, and organic-inorganic composite solid electrolytes[14]. The inorganic SEs generally outperform the organic polymer-based types in terms of ionic conductivity, mechanical strength, and electrochemical stability[15]. The field of inorganic SEs mainly explored oxides and sulphides as candidates, until Asano *et al.* [16] introduced halides as a potential candidate for SEs, showcasing high Li^+-conductivity and excellent oxidation stability.

2.2. Halide solid electrolytes

Halide electrolytes owe their high ionic conductivity primarily to the weaker coulombic interactions between lithium ions and monovalent halogen anions (F^-, Cl^-, Br^- and I^-) compared to divalent anions (S^{2-} and O^{2-})[17]. Moreover, the ionic radii of halogen anions are larger than those of oxide and sulphide, leading to longer ionic bond lengths and thus better Li^+-mobility[17].

A second key advantage of halide electrolytes is their excellent oxidation stability, often exceeding 4.2 V vs. Li/Li^+, attributed to the highly electronegative halide anions[18]. Figure 2.2 compares the electrochemical stability windows of several commonly studied solid-state electrolyte chemistries, highlighting the oxidation stability of halide systems.

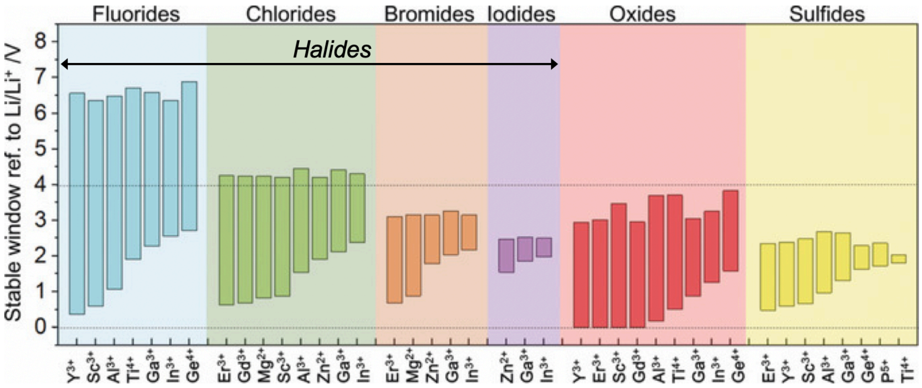

Figure 2.2: Comparing the stability of various solid electrolyte chemistries. Adapted from Wang *et al.* [19].

In fact, the oxidation potential of halide electrolytes depends primarily on the inherent oxidation potential of the halogen anions, which increases with increasing electronegativity: $I^- < Br^- < Cl^-$ « F^-[7]. This trend, along with the resulting compatibility of chlorides and fluorides with 4 V cathodes, can be observed in Figure 2.2.

However, the main challenge associated with halide SEs is their limited stability at low potentials, i.e. against the anode. Ideally, the halide SE remains stable down to–or beyond–0 V against Li/Li^+ in order to be compatible with a lithium metal anode. Remember that an anode in lithium-ion batteries primarily serves to provide lithium ions upon discharging and store lithium metal upon charging, which means that the use of pure lithium metal will thus result in the highest energy density anode: lithium metal (3860 mAh/g)[18]. As shown in Figure 2.2, most currently researched halide SEs do not reach this potential. The reduction potential–and thus compatibility with high-capacity anodes–is largely determined by the electronegativity of the central metal cation and generally ranges from 0.6 to 2.4 V vs. Li/Li$^+$, with lower electronegativities correlating to lower reduction potentials[20]. For example, electrolytes containing Group 3 transition metals with low electronegativities such as Li_3YCl_6 and Li_3ScCl_6, have been found to be stable until 0.59 and 0.91 V vs. Li/Li$^+$, respectively[20]. In contrast, halide electrolytes with Group 13 metals have higher reduction potentials, owing to the larger electronegativity of their central metal cations, such as Li_3InCl_6 (2.38 V vs. Li/Li$^+$) and Li_3TlCl_6 (3.45 V vs. Li/Li$^+$)[20]. Furthermore, it was found that in multi-cation halide electrolytes, the reduction potential is generally determined by the more electronegative metal[20].

An in-depth study of halides as solid electrolytes requires further investigation of its structure. Halide solid-state electrolytes form anionic lattices of the Li_aMX_6 type, in which M is a metal cation [M^{3+} or M^{4+}], X = [F^-, Cl^-, Br^-, or I^-] and a = 2 or 3 for tetravalent or trivalent metal cations, respectively. Of these anions, Cl^- is most widely explored because its intermediate electronegativity achieves the right balance between sufficient ionic conductivity and a suitable electrochemical stability window[18]. The anionic lattices are categorized as either hexagonal close-packed (hcp) or cubic close-packed (ccp) types. The crystal structures are further distinguished into space groups, of which three are the most common: the P3m1 trigonal structure with hcp lattice, the Pnma orthorhombic structure with hcp lattice, and the C2/m monoclinic structure with ccp lattice (see Figure 2.3). Typically, small cationic radii result in a monoclinic structure, intermediate radii in an orthorhombic structure, and large cationic radii in a trigonal structure[18],[20].

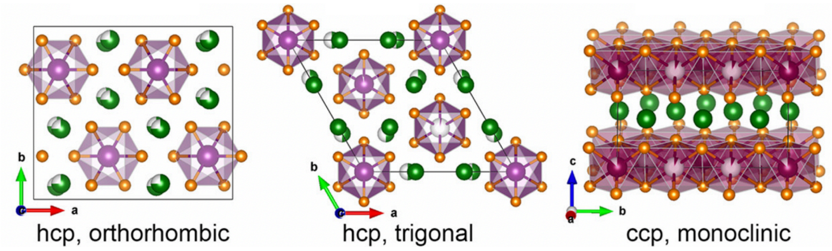

Figure 2.3: Crystal structures of halide solid-state electrolytes illustrating various packing structures and symmetries. From left to right: hexagonal close-packed (hcp) orthorhombic, hcp trigonal, and cubic close-packed (ccp) monoclinic. Adapted from Wang *et al.* [17].

The monoclinic structure generally shows better ionic mobility compared to the other structures, due to the greater number of 3D ion diffusion pathways it offers, making this structure the most promising SE candidate[17],[18]. In the monoclinic structure ($\alpha = \gamma = 90° \neq \beta$ and $a \neq b \neq c$) the chlorine anions (Cl^-) form an anionic structure of the cubic close-packed (ccp) configuration, in which the crystal layers repeat in ABCA fashion, as presented in Figure 2.4.

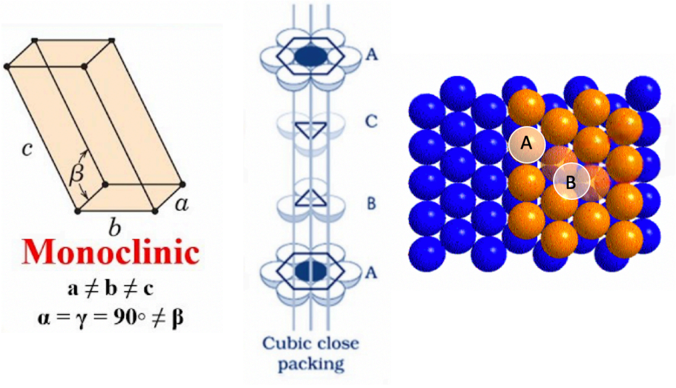

Figure 2.4: The monoclinic ccp lattice. The ABCA stacking pattern leaves two different types of interstitial sites: tetrahedral sites (A) lay directly underneath an atom in the orange layer, octahedral sites (B) are located where gaps can be observed through both the orange and blue layer. Adapted from Enaki *et al.* [21]

In this negatively charged framework, positively charged cations (M^{x+} or Li^+) can occupy free interstitial sites, which occur in two forms: tetrahedral and octahedral. As shown in Figure 2.4, tetrahedral sites (A) are situated between three atoms in the blue layer and one atom directly above in orange layer, resulting in a coordination number of four. Octahedral sites (B) are positioned between three atoms in the blue layer and three atoms in the orange layer, resulting in a coordination number of six.

Octahedral sites are energetically more favourable for cation placement due to their larger size and higher coordination number. As a result, metal cations (M^{x+}) occupy some of these sites. The smaller lithium cations (Li^+) occupy remaining octahedral and tetrahedral interstitial sites, until charge balance is achieved.

2.3. The use of zirconium in solid electrolytes

Li_2ZrCl_6 (LZC) is recognised for its relatively low cost of raw material and good moisture stability[22]. In addition, it shows excellent oxidation stability (beyond 4.0 V vs. Li/Li^+), making it a promising candidate for next-generation batteries with enhanced energy density, as it is compatible with high-voltage cathode materials such as NMC or $LiCoO_2$[23],[24]. Further, incorporating the tetravalent zirconium cation (Zr^{4+}) into halide SEs has been demonstrated to enhance ionic conductivity, while offering cost advantages over many other rare-earth-metal cations used in halide electrolytes[6].

2.3.1. Effect of zirconium on ionic conductivity

Zirconium has been found to specifically improve ionic conductivity through aliovalent substitution, where M^{3+} cations are partially replaced by Zr^{4+}. This substitution increases the number of available interstitial sites for Li^+ atoms, thereby enabling more diffusion pathways and improving lithium-ion diffusivity[10]. This strategy has been successfully applied to Li_3InCl_6[10],[25], Li_3YbCl_6[26] and Li_3ScCl_6[25]. For example, substituting 30% of indium in Li_3InCl_6 has been shown to improve ionic conductivity by a factor of 1.6, reaching 2.02 mS/cm at room temperature[10]. Computational work by Park *et al.* [27] supports these findings, showing enhanced conductivity in $Li_{2.5}In_{0.5}Zr_{0.5}Cl$ and $Li_{2.5}Sc_{0.5}Zr_{0.5}Cl$ with respect to their zirconium-free configurations, by factors of 1.25 and 4.5, respectively. This aligns with findings of Liu *et al.* [28], who concluded that lowering cation concentration and thus lithium content in Li_xMCl_6 generates lithium vacancies that are beneficial for fast Li^+ conduction. Moreover, the zirconium substitution strategy may also increase the degree of preferred orientation, thereby improving transport kinetics[29]. However, this strategy requires careful optimisation, as excessive substitution results in a decrease in ionic conductivity due to a reduced number of charge carriers (Li^+)[10].

In the specific case of LZC, structural polymorphism also plays a key role in ionic transport. While LZC has primarily been studied in its trigonal form, Kwak *et al.* [6] reported the existence of two distinct phases: a monoclinic (ccp) and a trigonal (hcp) structure. Interestingly, although monoclinic structures typically exhibit higher ionic conductivities in halide systems, the opposite is observed in LZC. The trigonal structure achieves a conductivity of 0.40 mS/cm, whereas the monoclinic form reaches only 0.0057 mS/cm[6].

2.3.2. Effect of zirconium on electrochemical stability

The reduction stability of LZC is relatively limited, with previous studies reporting a reduction onset of 2 V versus Li/Li^+[22],[30]. This limited reduction stability has been reported to transfer to compounds in which Zr^{4+}-substitution was applied: $Li_{3-x}Er_{1-x}Zr_xCl_6$[31] and $Li_{3-x}Sc_{1-x}Zr_xCl_6$[29] showed worse reduction stability than their zirconium-free configurations. Computational studies by Tham *et al.* [32] also predicted the narrowing effect on the electrochemical stability window of Zr^{4+}-substitution in the compounds $Li_{2.5}M_{0.5}Zr_{0.5}Cl_6$ (M: Lu, Sc, In, and Y). Specifically, the onset reduction potential was found to be approximately equal to the highest value of the reduction potential of Li_2ZrCl_6 or Li_3MCl_6. This matches the observation of Wu *et al.* [20], who reported that in halide solid-state electrolytes, the reduction potential is typically governed by the more electronegative cation.

However, it is important to distinguish between the thermodynamic reduction onset and the practical reduction stability during cycling–as further discussed in section 2.5. Notably, Cheng *et al.* [33] recently demonstrated that trigonal LZC can be cycled well beyond onset reduction potential–down to 1.4 V vs. Li/Li^+–without undergoing structural breakdown. This indicates that, although Zr-based halide electrolytes may undergo reduction at relatively high onset potentials, they may still offer an expanded practical electrochemical window, enabling stable operation over a wider voltage range.

2.4. High entropy as a strategy to enhance electrolyte properties

Introducing configurational entropy into SEs has emerged as a widely adopted strategy to enhance Li^+-conductivity and improve electrochemical stability, particularly against high-voltage cathodes[7]. High-entropy (HE) halide SEs are of the general form Li_aMX_6 and ideally contain four or more metal cations (M^{x+}) in (near-)equimolar ratios[34]. The combination of various metal cations significantly increases configurational entropy, which in turn reduces the Gibbs free energy of the system and stabilizes the structure thermodynamically[34]–[36]. Although this thermodynamic stabilisation could, in principle, enhance both high- and low-voltage stability, its impact on stability at low-voltage anodes remains largely unexplored.

Beyond thermodynamic stabilisation, the variation in ionic radii among the mixed cations introduces local lattice distortions, which can enable percolating diffusion pathways for lithium ions and can thus improve ionic conductivity[34]. Studies on oxide-based SEs claim that improved conductivity arises not from the intrinsic properties of specific elements, but from the degree of lattice distortion, which is primarily governed by cation size mismatch[37]. Lattice distortion resulting from configurational entropy has also been identified as a cause for improved characteristics in HE halide SEs. Song *et al.* [38] for example concludes that lattice distortions in $Li_{2.75}Y_{0.16}Er_{0.16}Yb_{0.16}In_{0.25}Zr_{0.25}Cl_6$ lead to spatial confinement of chlorine anions, which kinetically limits oxidation and thus improves high-voltage stability. The authors further attribute the observed improvement in Li^+-conductivity to lengthening of Li-Cl bonds stemming from lattice distortions.

Further, configurational entropy has been demonstrated to greatly affect morphology, which could further improve Li^+-transport properties. A study by Wang *et al.* [7] showed that $Li_{2.8}MCl_6$, where M = In^{3+}, Sc^{3+}, Yb^{3+}, Lu^{3+}, and Zr^{4+} in equimolar ratios, exhibits an improved ionic conductivity of 2.1 mS/cm compared to 1.2 mS/cm for Li_3InCl_6. This enhancement is attributed to increased cationic disorder introduced by high configurational entropy, which narrows the distribution of surface energies. As a result, anisotropic growth is suppressed, and the material adopts a more spherical morphology, characterized by smaller and smoother particles. The spherical morphology enhances densification by reducing interfacial resistance, thereby contributing to better Li^+-transport properties.

While entropic effects and lattice distortions resulting from variations in in ionic size are often called upon to explain improved electrolyte properties, the influence of intrinsic cation properties–such as electronic configuration and valence state–remains largely unexplored. Such considerations could perhaps also account for the limited gains observed when further increasing configurational entropy through the addition of a sixth cation, which only marginally enhanced ionic conductivity[7].

In parallel, high-entropy design is often highlighted as a route towards more resource-accessible battery materials, due to the possibility of partially substituting rare-earth elements with more abundant alternatives[34]. Despite this potential, many HE electrolytes studied to date continue to rely on rare-earth metals such as erbium, ytterbium, and scandium, which are associated with high environmental and socio-economic costs[39]. Figure 2.5 presents a comparison of the relative abundance and market cost of elements commonly investigated in the development of solid state electrolytes.

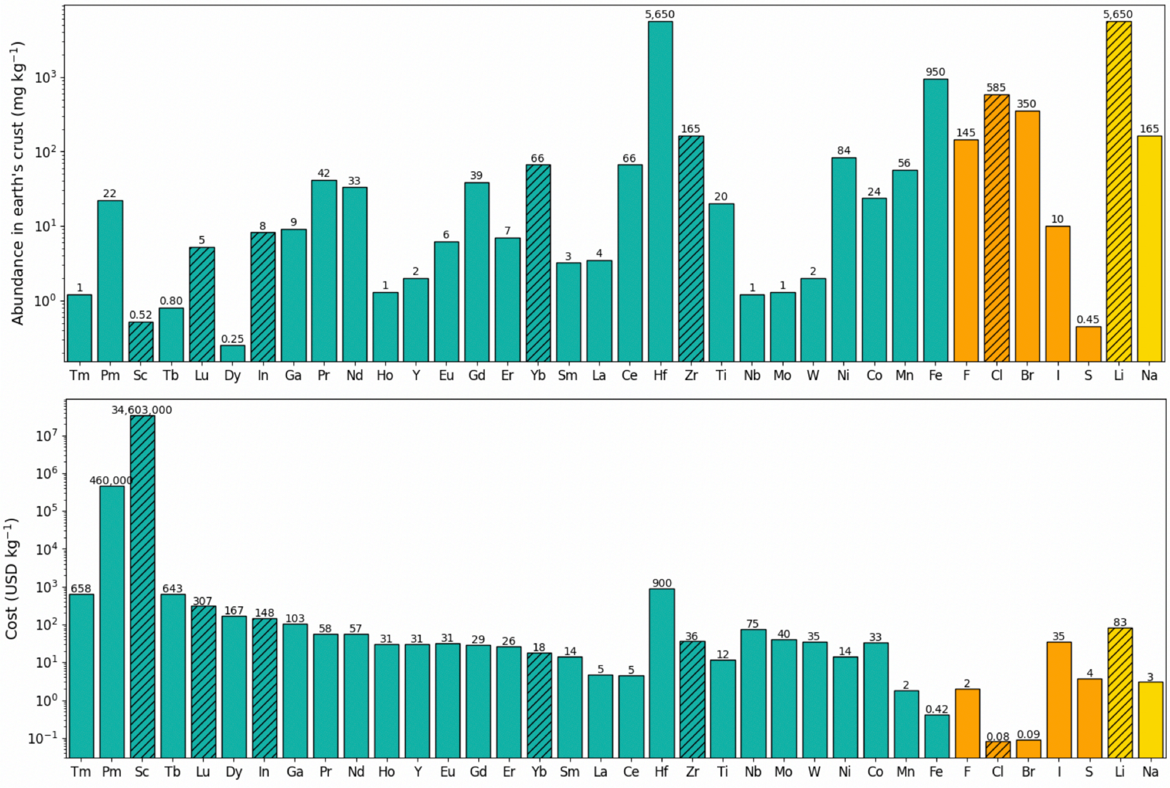

Figure 2.5: Elemental abundance and cost of materials used in halide SEs. The relative abundance is pictured on the top and the market cost on the bottom. Elements are grouped per category: lanthanides and (post) transition metals (turquoise), halides (orange), and alkali metal cations (yellow). Elements with hatched patterns are used in experimental work in this study. Adapted from Wang *et al.* [17]

.

The elements with a hatched pattern in Figure 2.5 deserve specific attention, as they are utilised in this work. Of these elements, scandium is especially rare, with its price peaking at a staggering 34 million USD per kg. Moreover, lithium and indium appear on the list of most critical materials for the global energy transition, highlighting that while they might currently not be the most costly elements, they are indispensable metals for the energy transition that are subject to supply constraints[40].

2.5. Stability of solid electrolytes

A solid electrolyte needs to show both high ionic conductivity and sufficient stability under operating conditions. More specifically, an electrolyte can be stable in multiple ways[41]:

- A **thermally stable** electrolyte can resist decomposition at elevated temperatures.
- A **mechanically stable** electrolyte is able to continue to function under mechanical stress, either from external or internal sources.
- A **chemically stable** electrolyte does not undergo chemical reactions under storage conditions.
- An **electrochemically stable** electrolyte is stable against the electrochemical conditions at the electrolyte-electrode interface.

The electrochemical stability of an electrolyte is usually quantified by its electrochemical stability window (ESW), which is the range of voltages that an electrolyte can sustain without undergoing decomposition or side reactions[42]. The ESW should be sufficiently wide to tolerate the low voltages at the anode and the high voltages at the cathode. Table 2.1 tabulates commonly used and/or researched anodes and their associated voltages.

Table 2.1: Various widely used and/or researched anode materials with their associated voltages.

Anode	Operating voltage (V) vs. Li/Li$^+$	Source
Lithium Titanate ($Li_4Ti_5O_{12}$, LTO)	1.6	Nzereogu *et al.* [43]
Titanium Dioxide (TiO_2)	1.5	Lu *et al.* [44]
Tin (Sn)	0.6	Lu *et al.* [44]
Silicon Dioxide (SiO_2)	0.5	Khan *et al.* [45]
Silicon (Si)	0.4	Feng *et al.* [46]
Graphite (C)	0.1	Asenbauer *et al.* [47]
Lithium (Li)	0.0	Lu *et al.* [44]

Note that the low voltages to which the electrolyte is exposed at the anode promote electron uptake, thereby inducing reduction of the electrolyte. In this case, lithium ions and their accompanying electrons are inserted into the structure. Conversely, the high potentials near the cathode favour the removal of lithium ions along with electrons, leading to oxidation of the electrolyte. Thus, lithiation at the anode is associated with reduction, while delithiation at the cathode corresponds to oxidation, reflecting the gain and loss of electrons, respectively.

2.5.1. Electrochemical stability window: intrinsic and extended window

Frequently, an electrolyte is cycled in a battery to voltages higher than its oxidation potential and lower than its reduction potential without undergoing detrimental decomposition[48]. Therefore, the ESW can be expanded into two windows, namely (1) the **intrinsic ESW** , and (2) the **extended ESW**, as visualised in Figure 2.6.

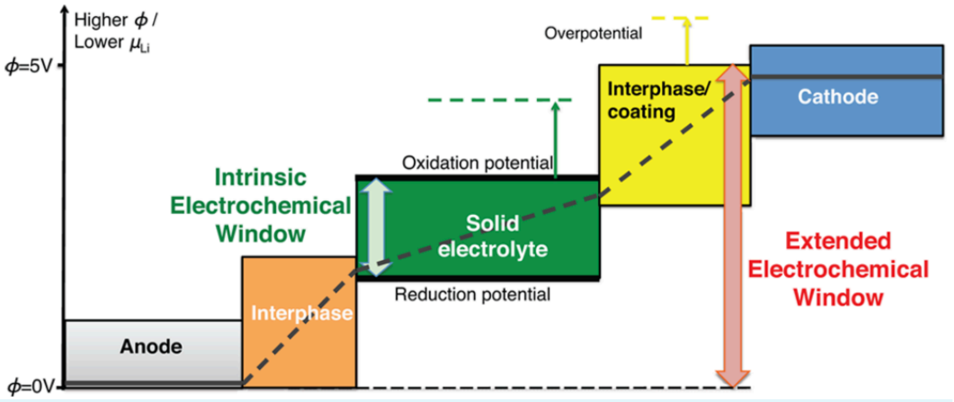

Figure 2.6: Schematic depiction of the voltage profile (ϕ) within a solid-state battery. The intrinsic electrochemical window (green) is extended by the interphases (orange and yellow) to obtain the extended electrochemical window (red arrow). Reproduced from Zhu *et al.* [48]

.

The intrinsic window is thus the range of potentials over which an electrolyte does not undergo any redox reactions, whereas the extended stability window is an extended range of potentials in which redox reactions take place which do not result in the detrimental degradation of the electrolyte. Several behaviours can lead to an observed extended ESW:

1. A **solid electrolyte interface** (SEI) may form at the electrode-electrolyte interface. This thin, insulating layer–composed of decomposition products–blocks electron transfer into the bulk of the electrolyte, thereby passivating the interface and preventing further degradation[48],[49].
2. The electrolyte may undergo **reversible decomposition reactions** in the ESW, but the original structure can be (partially) restored when cycling back into the intrinsic ESW[33].
3. The electrolyte may undergo **lithiation/delithiation** without structural decomposition[50],[51]. The redox activity in the extended electrochemical window corresponds to the insertion or extraction

of Li^+ and electrons into or from the crystal structure, while the overall crystal structure remains intact.

Zhu *et al.* [48] demonstrated an extended electrochemical window enabled by SEI formation for the solid electrolyte lithium phosphorous oxynitride (LiPON or Li_2PO_2N)–it decomposes into a stable passivating layer composed of Li_3P, Li_3N, and Li_2O. In some cases, the volumetric expansion associated with the formation of these decomposition products induces mechanical stress, which has been shown to contribute to the suppression of further degradation by significantly reducing ionic diffusivity at the interface[49]. However, halide SEs typically do not form a passivating SEI layer, as their decomposition products are their respective elemental metals, which are electrically conductive[18]:

$$\mathrm{Li}_a\mathrm{MCl}_6 + (6\text{-x})\,\mathrm{Li} \longrightarrow 6\,\mathrm{LiCl} + \mathrm{M}^0 \tag{2.1}$$

Consequently, the formation of a potential SEI layer is typically not self-limiting in halide solid electrolytes because it fails to electrically isolate the bulk of the electrolyte from the electrode. This facilitates the continued transport of electrons throughout the electrolyte, which ultimately leads to its complete degradation. An interesting exception to this rule was reported for $Li_3YCl_4Br_2$, where, unsurprisingly, yttrium metal formed at the lithium anode[52]. However, upon cycling, yttrium metal migrated to the electrode surface, with LiCl and LiBr remaining facing the electrolyte, thereby preventing further degradation and creating a stable interface[52].

An observed extended electrochemical window may, in some cases, also result from the reversible decomposition of the electrolyte. Chen *et al.* [53] demonstrated that the halide solid electrolyte $Li_{2.5}Zr_{0.5}Y_{0.5}Cl_6$ undergoes partial decomposition at low voltages, with Zr^{4+} and Y^{3+} being reduced to their metallic states (Zr^0 and Y^0). Their findings indicate that these metallic states can be partially reoxidized to form the original crystalline structure, provided that deep discharge (below 1.1 V) is avoided. Discharge beyond this point leads to severe amorphisation and metal aggregation, resulting in irreversible decomposition so that upon recharging, only the oxidized products $ZrCl_4$ and YCl_3 are formed, rather than the pristine crystal structure. Such reports remain rare, and although some reversibility has been observed, metal formation is undesirable–even if reversible–as it increases electronic conductivity and may limit long-term stability under extended cycling or deep discharge[53].

However, reversible lithiation/delithiation reactions outside the intrinsic stability window are more commonly reported and can result in an extended electrochemical window. In this case, lithium reversibly intercalates within the crystal, without destroying the original crystal structure, as presented in the following reaction:

$$\mathrm{Li}_a\mathrm{MCl}_6 + \mathrm{xLi} \longrightarrow \mathrm{Li}_{a+x}\mathrm{MCl}_6 \tag{2.2}$$

Cheng *et al.* [33], for example, demonstrated reversible lithiation/delithiation in both $Li_3YCl_3Br_3$ and trigonal Li_2ZrCl_6. Their findings showed that lithium is inserted without resulting in phase separation, leading the authors to introduce the concept of a *dynamic window*–a pactically extended electrochemical window beyond the material's intrinsic reduction stability. A beneficial side effect of this behaviour is that lithium intercalation effectively increases the cell energy density. Similar behaviour was observed for the halide material Li_3TiCl_6, which demonstrates excellent low-voltage stability beyond its intrinsic thermodynamic limits by supporting a reversible Ti^{2+}/Ti^{3+} redox reaction between 1.7 and 2.6 V vs. Li/Li^+, without inducing phase transitions or structural degradation[54].

Reversible lithiation/delithiation has also been reported for other types of solid electrolytes, including the oxide-based electrolyte lithium aluminium titanium phosphate (LATP, $Li_3Al_{0.3}Ti_{1.7}(PO_4)_3$)[55],[56]. Arbi *et al.* [55] reported that up to 1.6 Li per formula unit can be reversibly intercalated into the crystal under slow potentiostatic conditions. Although insertion into LATP lead to a reduction in crystal symmetry–caused by lithium occupying additional metal sites and slight lattice distortions–the underlying crystal framework remained structurally intact. Importantly, lithiated LATP was demonstrated to preserve its high Li^+-conductivity and low electronic conductivity, crucial for its application as an electrolyte[56].

Having distinguished between the intrinsic stability window and the practically extended window that is generally enabled by lithiation/delithiation in halide solid electrolytes, the following section summarises the computational and experimental methods commonly employed in the literature to quantify them.

2.5.2. Experimental approaches to assessing electrochemical stability

One experimental technique frequently deployed to find the intrinsic ESW is linear sweep voltammetry (LSV)[33],[57]. In this method, a range of voltages is applied to the material and the resulting current is measured. During the negative scan–where applied voltages become progressively lower–current peaks indicate reduction of the electrolyte, while during a positive scan–where applied voltages become increasingly higher–current peaks indicate oxidation. This method is limited to identifying the intrinsic window, since observed redox peaks may indicate decomposition, but may also correspond to the formation of a SEI layer, reversible redox reactions, or lithiation/delithiation behaviour that effectively expands the electrochemical stability window[33],[57].

To assess the reversibility of observed redox reactions–and thereby distinguish between irreversible decomposition and non-destructive redox reactions that extend the electrochemical stability window–cyclic voltammetry (CV) is frequently employed[31],[53],[58]. Unlike LSV, which sweeps the voltage in a single direction, CV involves sweeping the voltage in both positive and negative directions. However, a limitation of this method is that peaks resulting from reversible redox reactions of the original electrolyte and those of decomposition products cannot be readily distinguished if their redox reactions occur at similar potentials. In such cases, additional characterisation techniques are required. Moreover, CV tends to overestimate the electrochemical stability window due to the small electrolyteelectrode contact area and the short time scale of these experiments compared to low-current-density battery cycling[33],[50],[51]. Therefore, accurate CV results require at the very least the addition of a conductive additive to the electrolyte to increase the effective contact area between the electrolyte and the current collector and the use of a very low current density, the latter of which is typically not used in CV[33].

Galvanostatic cycling is another method widely used to investigate the reversibility of redox reactions occurring outside the intrinsic ESW of the SE, by assessing capacity retention over multiple charge-discharge cycles[33],[53],[58]. To evaluate low-voltage stability, a half-cell can be constructed using a cathode composed of the solid electrolyte mixed with carbon, a Li-containing anode, and an electrolyte that is stable at both electrode interfaces[53]. This half-cell is then subjected to repeated charge-discharge cycles at a constant current within a defined voltage range. Reversibility can now be assessed by means of capacity retention and shifts in the voltage profile[33]. However, as with CV, galvanostatic cycling must be complemented with characterisation techniques to capture structural changes. Chen *et al.* [53] for example combined X-ray photoelectron spectroscopy (XPS) and X-ray diffraction (XRD) to probe chemical and structural changes during cycling, and in situ electrochemical impedance spectroscopy (EIS) and distribution of relaxation times (DRT) to track the evolution of ionic conductivity.

2.5.3. Computational approaches to predicting electrochemical stability

The intrinsic ESW of a material can be predicted computationally in addition to being determined experimentally. From a theoretical perspective, a material is oxidised when an electron is removed from its highest occupied molecular orbital (HOMO) and is reduced when an electron is added to its lowest unoccupied molecular orbital (LUMO). Consequently, the energy difference between the HOMO and LUMO–the bandgap (BG)–may provide a rough estimate of the ESW[42],[59]. In crystalline solids, the discrete molecular orbitals of individual atoms merge into continuous energy bands due to long-range periodicity, giving rise to the valence band maximum (VBM) and the conduction band minimum (CBM), which are the solid-state analogues of the HOMO and LUMO, respectively[60]. This method tends to overestimate the stability window, as it neglects interfacial effects such as band bending caused by contact with the electrode[59].

A second method for calculating the ESW is based on the reaction energies associated with the formation of decomposition products. This approach uses a grand canonical phase diagram to identify potential decomposition products and determines the voltages at which these products become thermodynamically favourable, using the formation energy differences between the pristine electrolyte and its decomposition products[42]. This approach was used to calculate the ESW of LZC to equal 1.75 to 4.25 V vs. Li/Li^+[22]. When Richards *et al.* [61] deployed this method to a wide variety of solid electrolytes, they concluded that the "anodic stability is determined primarily by the stability window of the related binary, or, in the case of mixed anion materials, by that of the least stable related binary material." This would imply that the anodic stability of Li_3MCl_6 is determined primarily by the stability of LiCl and is thus largely unaffected by the stability of the central metal cation, which opposes more recent findings[20]. Further, this method tends to underestimate the value of the ESW because it does not consider the energy barriers that may kinetically hinder the formation of decomposition products, even when they are thermodynamically favourable[48],[50],[51].

Therefore, a third approach to determining the ESW is based not on the formation energies of the decomposition products, but on the ground-state formation energies of lithiated and delithiated phases of the electrolyte. In this method, the intrinsic ESW is defined as the average voltage required to add or remove lithium from the compound and thereby reduce or oxidize the electrolyte, respectively[33]. The ground-state energies of different phases are calculated and plotted against the lithium concentration, after which a convex hull is constructed by connecting the lowest energies of formation, as illustrated in Figure 2.7a.

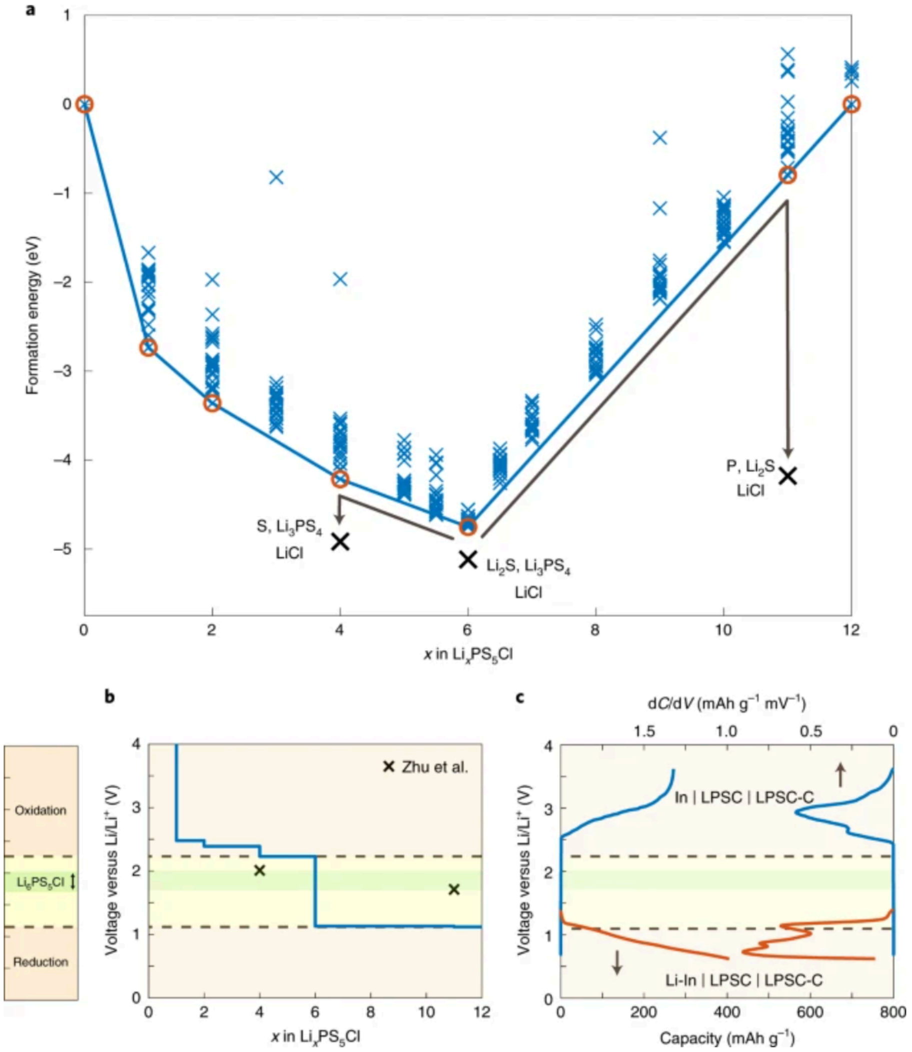

Figure 2.7: Calculating the ESW based on the formation energy of the ground-state energies of the lithiated and delithiated phases. a, Formation energies of Li_xPS_5Cl for various (de)lithiated phases, plotted against the lithium concentration x. Structures on the convex hull are considered stable and are highlighted with red circles. The formation energy of the decomposition products is indicated with black crosses, but reaction to these products is kinetically hindered despite being thermodynamically favourable. **b,** Corresponding voltage profile calculated from the stable structures on the convex hull. The black crosses indicate the predicted ESW based on the formation energy of the decomposition products. **c,** Charge and discharge curves of Li_xPS_5Cl, showing much better agreement with the calculated voltage based on (de)lithiated phases than based on decomposition products. Reproduced from Schwietert *et al.* [51].

Only phases that lie on the convex hull are considered thermodynamically stable. In the case illustrated in Figure 2.7, this implies that during lithiation, Li_6PS_5Cl coexists with $Li_{11}PS_5Cl$, while during delithiation it coexists with Li_4PS_5Cl. The intrinsic ESW is thus determined by the voltage required to form Li_4PS_5Cl at the cathode and $Li_{11}PS_5Cl$ at the anode. Using this approach, Schwietert *et al.* [51] demonstrated that sulphide- and oxide-based electrolytes exhibit a broader stability window by undergoing an indirect decomposition pathway through (de)lithiation. Therefore, the intrinsic ESW is determined by the reaction energies associated with forming these (de)lithiated phases, rather than the direct formation energies of the final–most stable–decomposition products. This interpretation aligns with earlier findings by Zhu *et al.* [48], who noted that the sluggish reaction kinetics between meta-stable compositions to the thermodynamically most stable decomposition product can prevent its decomposition on the timescales used during cycling.

As a final note, lithiation/delithiation can proceed in two ways: via phase separation or by forming a solid solution region[62]. In phase separation, discrete phases coexist–such as Li_6PS_5Cl and $Li_{11}PS_5Cl$ in Figure 2.7–resulting in distinct voltage plateaus. In contrast, solid-solution behaviour is observed when more lithiated phases are energetically accessible along the convex hull, yielding a more sloping voltage profile without pronounced voltage plateaus[62].

Finding the ground-state energies required for the convex hull method requires the use of density functional theory (DFT). The next section summarizes the working principle of DFT and its underlying principles and assumptions.

2.6. Principles of Density Functional Theory

Density functional theory (DFT) is a widely used computational method that calculates material properties that are difficult, costly, or sometimes even impossible to obtain experimentally. In essence, it aims to find the ground-state energy of a system on an atomistic scale, which allows for the assessment of the stability of compounds, predictions of reaction mechanisms, and much more. In its core, DFT is a powerful tool that balances accuracy and computational efficiency to zoom in and make predictions about material properties or explain experimentally observed phenomena on the atomic scale[63].

The small size of atoms makes quantum effects significant and requires particles to be described using wave functions $\psi(\mathbf{r})$. The Schrödinger equation can be used to describe a system of N electrons in terms of wave functions[63]:

$$\hat{H}\psi(\mathbf{r}) = E\psi(\mathbf{r}) \tag{2.3}$$

where E is the ground-state energy of the system and $\hat{H}$ the Hamiltonian operator, which includes the kinetic and potential energy of both the electrons and the nuclei. However, this simple appearing equation quickly becomes a complex many-body problem because the movements of nuclei and electrons are considered simultaneously. These movements can be separated using the Born-Oppenheimer approximation, which relies on the observation that nuclei are nearly static compared to electrons due to their larger mass. The Schrödinger equation can now be rewritten and solved for a static arrangement for N electrons[63]:

$$\left[\underbrace{\frac{\hbar^2}{2m}\sum_{i=1}^{N}\nabla_i^2}_{\text{kinetic energy of electrons}} + \underbrace{\sum_{i=1}^{N} V_I(\vec{r}_i)}_{\text{interaction with nuclei}} + \underbrace{\sum_{i=1}^{N}\sum_{j<i} U(\vec{r}_i,\vec{r}_j)}_{\text{electron-electron interactions}} \right] \Psi = E_e\Psi; \quad \Psi = \Psi(\{\vec{r}_i, s_i\}) \tag{2.4}$$

where $\hbar$ is Planck's constant and m is the electron mass. Solving this equation yields the electronic wave function $\Psi(\{\vec{r}_i, s_i\}$ and the electronic energy E_e for a given arrangement of nuclei. Unfortunately, this equation is still difficult to solve because it contains a many-electron wave function with a high dimensionality. The wave function $\Psi(r_1, r_2, ...r_N)$ depends on the position of all N electrons, which in three-dimensional space leads to a 3N-dimensional wave function.

This problem was solved in the 1960s by Hohenberg and Kohn, who presented a set of mathematical equations and two theorems that laid the foundation of the entire field of DFT[64]. They found that the high-dimensional wave functions can be replaced by the electron density captured in functionals–giving rise to the name *density functional* theory. More specifically, they determined that (1) the electron density uniquely determines the ground-state energy, and (2) the electron density that minimises the energy of the overall functional is the density that describes the ground-state energy of the system. The electron density $n(r)$ is described as

$$n(r) = 2\sum_i \psi_i^*(r)\psi_i(r). \tag{2.5}$$

in which the wave functions ψ_i are treated separately to calculate the final electron density $n(r)$. The Schrödinger equation can now be approximated by a set of Kohn-Sham equations, which treat the movement of each electron separately to find the ground-state electron density of the system:

$$\left[\frac{\hbar^2}{2m}\nabla^2 + V_I(\vec{r}) + V_H(\vec{r}) + V_{\text{xc}}(\vec{r})\right]\psi_i(\vec{r}) = \epsilon_i\psi_i(\vec{r}); \quad V_H(\vec{r}) = e^2\int\frac{n(\vec{r'})}{|\vec{r}-\vec{r'}|}d^3r' \tag{2.6}$$

The left three terms represent the same terms as Equation 2.4, with the Hartree potential $V_H(\vec{r})$ being introduced to represent electron-electron interactions. The exchange-correlation functional V_{xc} is added as the fourth term to estimate the quantum-mechanical effects of the electron-electron interactions. However, the exact value for this functional is unknown and can only be approximated through different functionals, such as the local density approximation (LDA) or the generalized gradient approximation (GGA).

Finally, Equation 2.6 can be used to find the ground-state energy of the system in an iterative self-consistent field (SCF) procedure. This process begins with in initial guess for electron density n(r), which is inputted in the Kohn-Sham equations to find the single-particle wave functions $\psi_i(\vec{r})$. These are then used to find the electron density through Equation 2.5, which is then compared to the initial electron density, and a new guess for n(r) is made. When the difference between two consecutive electron densities is sufficiently small the solution is considered self-consistent, the iteration loop is stopped, and the lowest-energy configuration is found. Thus, density functional theory simplifies the complex many-body problem by reformulating it in terms of electron density rather than the full-wave function and using it to find the ground-state energy of the system.

It should be noted here that DFT is per definition performed at zero Kelvin, which means that temperature-induced movement of the atoms is not considered. Therefore, DFT can only find the ground-state energy of the system, as this is the only state accessible at zero K.

2.7. Principles of *Ab initio* molecular dynamics

While DFT is a powerful method to study the state of systems, it cannot study the evolution of systems over time nor at a non-zero Kelvin temperature. To this end, molecular dynamics simulations are used. Molecular dynamics (MD) is a computational simulation technique that studies the behaviour of a system at the molecular level as it responds to forces acting on its particles. This is done by numerically solving classical Newtonian equations of motion for a system from an initial state, using boundary conditions appropriate to the problem[65]. The output of a simulation is the trajectory: a recorded sequence of positions, velocities, and forces acting on all particles within the system over time.

It is important to realize the difference between MD and experiments. MD simulations study one system configuration of a many-body system as it evolves over time. Experiments, on the other hand, find physical values that are the average of all configurations present in the studied material (i.e. the ensemble average)[66]. The bridge between these two is formed by statistical mechanics, or more specifically, ergodicity. Ergodicity implies that a system will explore all accessible configurations, given enough time. This justifies the equation of the time average of a singular MD simulation to the ensemble average, as the two will converge over a sufficiently long time[66]. Although this work does not directly compare time-averaged physical values that can be obtained from MD simulations to the ensemble-averaged macroscopic quantities measured in experiments, it is nonetheless important to remain aware of the methodological limitations. In this study, MD is instead employed as a predictive tool for assessing structural stability when kinetic energy is introduced into the system by means of a non-zero temperature.

Having established that molecular dynamics (MD) simulations provide valuable insights into the system, we now proceed to examine the underlying principles and operational details of these simulations. MD can study an isolated system using pair-additive forces: the force acting on each particle equals the sum of the forces it exerts on other particles[66]. Thus, the net force acting on particle i equals

$$\vec{F}_i(\vec{r}_i) = \sum_{j \neq i} F(\vec{r}_i - \vec{r}_j)\hat{r}_{ij} \tag{2.7}$$

where $\vec{r}_i$ is the position of particle i, $F(\vec{r}_i - \vec{r}_j)$ a scalar function of the force depending on the distance between particles i and j, and $\hat{r}_{ij}$ a unit vector that provides the direction of the force. Next, we should recognize that the Newtonian equations of motions apply to the system, so that the acceleration of the particle is described by[66]:

$$\frac{d^2\vec{r}_i(t)}{dt^2} = \frac{\vec{F}_i(\vec{r}_i)}{m_i} \tag{2.8}$$

where m_i is the mass of particle i and t the time. A common way to express particle position is by means of a numeric expression called the Verlet algorithm, which clearly shows the particle position as a function of $t + \Delta t$[63].

$$\vec{r}(t + \Delta t) \approx 2\vec{r}(t) - \vec{r}(t - \Delta t) + \frac{\vec{F}(t)}{m}\Delta t^2 \tag{2.9}$$

The choice of force $\vec{F}_i$ now divides the field of MD into classical molecular dynamics and *ab initio* molecular dynamics (AIMD). Classical molecular dynamics uses (semi-) empirically found forces from force fields and does not consider the quantum mechanical effects acting on the atomic scale. AIMD instead uses forces obtained from wave functions in DFT calculations to find the movement of each particle[63]. AIMD is much more computationally demanding and is therefore limited to smaller system sizes and shorter timescales. Yet, it does yield more accurate results because it considers non-negligible quantum effects acting on the atomic scale. This work therefore only uses AIMD.

Crucial for AIMD is the Hellmann-Feynman theorem, which states that forces acting on particles can be expressed directly in terms of the gradient of the electronic potential with respect to the nuclear coordinates, provided the electronic wave function is the ground-state solution and satisfies the Born-Oppenheimer approximation[67]:

$$\mathbf{F}_I = -\frac{\partial E}{\partial \mathbf{R}_I} \tag{2.10}$$

where E is the total energy of the system obtained from DFT, and R_I is the position of particle I. To this end, first, an initial system configuration is defined and its electronic structure is calculated using DFT. Next, the forces acting on each particle are calculated from the electronic structure using Equation 2.10. These forces are then used to update the position of each particle using Equation 2.9 over a short time period Δt. In this next time step, the electronic structure is calculated again and the loop iterates until the desired number of time steps is achieved. Thus, trajectories are generated using forces obtained directly from electronic structure calculations as the simulation progresses[65].

As mentioned before, these time-averaged trajectories can be used to express real-world ensemble averages when a system is assumed to be ergodic. An ensemble is a collection of virtual copies of a system, considered simultaneously, each representing a possible system with three thermodynamic state variables fixed. These variables are energy (E), temperature (T), volume (V), pressure (P), and number of particles (N). A specific ensemble can be picked depending on the bulk property that one wants to extract from the simulation of individual particles.

One commonly used–and in this study deployed–ensemble, is the canonical ensemble (NVT ensemble) in which the temperature, volume, and number of atoms are fixed. This is a very suitable ensemble to study atom migration for a structure which has been relaxed to a stable state with respect to its volume and atomic positions, as is the case in this study. Systems in which significant volumetric changes are expected are better studied using the microcanonical ensemble (NPT), which keeps pressure fixed and allows volume to change over time, yet tends to proceed more slowly.

However, keeping the temperature constant is not trivial and multiple thermostats have been developed to this end. The Nosé-Hover thermostat is a widely deployed method that relies on allowing the temperature to fluctuate around a target value in a smooth and realistic way by introducing a set of equations[66]. It does so by adding an artificial "thermostat" degree of freedom to the system that is coupled to the kinetic energy of the system. This degree of freedom acts as a thermal reservoir, which can absorb or supply energy to the system to adjust the temperature of the system[66].

AIMD can therefore simulate the movement of atoms over time, giving an indication of the stability of the material as temperature is introduced into the system.

Now, having summarized the field of halide solid-state batteries, electrochemical stability windows, and the computational methods underpinning computational studies on low-voltage stability, the next section will dive into the specific methods deployed in this work.

3

Methods

This chapter introduces the experimental and computational approaches employed to examine the halide solid electrolytes under investigation, and outlines the specific parameters applied throughout the study.

3.1. Experimental methods

Halide SEs were prepared via a two-step process involving ball milling followed by annealing. Galvanostatic discharge and cycling, combined with X-ray diffraction (XRD), were employed to determine electrochemical behaviour and monitor structure changes. Potentiostatic electrochemical impedance spectroscopy (PEIS) and direct current (DC) polarisation were used to find ionic conductivities and electronic conductivities, respectively. The halide electrolytes were handled under a continuous argon atmosphere to prevent reaction with moisture, and all experiments were conducted at room temperature.

3.1.1. Synthesis and characterisation

The halide SEs were synthesised using a simple two-step synthesis method: high-energy ball milling–the most widely used technique for the preparation of halide electrolytes[20]–followed by annealing. First, the precursor chlorine salts were mixed in the correct molar ratios. The mixture was then ball milled at 550 rpm for 16.5 hours– alternating between 5 minutes of milling and 5 minutes rest to prevent overheating. Ball milling was carried out in zirconium oxide (ZrO_2) jars with 14 ZrO_2 balls. Following milling, the resulting powder was pressed at 310 MPa for 5 minutes to a pellet with a diameter of 10 mm, which was sealed in a high-temperature-resistant glass vial. This vial was placed in a furnace and annealed at a temperature suitable for the formation of the desired compound, using a heating rate of 2 °C/min, allowing the material to naturally cool down to room temperature. Table 3.1 summarises the annealing parameters employed for each halide electrolyte.

Table 3.1: Annealing parameters used for synthesis of halide SEs. The high-entropy compounds (H4 and H5) were predominantly used in their as-milled form, preceding annealing.

Compound	Temp. [°C]	Time [h]	Reference
Li_3InCl_6 (LIC)	260	12	Ma *et al.* [68], Khoa *et al.* [69]
Monoclinic Li_2ZrCl_6 (LZC)	310	12	Wang *et al.* [22]
$Li_{2.5}In_{0.5}Zr_{0.5}Cl_6$	350	12	Helm *et al.* [9]
$Li_{2.8}Sc_{0.2}Zr_{0.2}Yb_{0.2}Lu_{0.2}In_{0.2}Cl_6$ (H5)	260	12	Song *et al.* [38]
$Li_{2.75}Sc_{0.25}Zr_{0.25}Yb_{0.25}Lu_{0.25}Cl_6$ (H4)	260	12	Song *et al.* [38]

Each electrolyte was subsequently mixed with a conductive additive–anhydrous vapour growth carbon fibre (VGCF)–in a 5:1 ratio for use as a cathode in a half-cell. This mixing was carried out either by (1) hand grinding for 10 minutes with a mortar and pestle, (2) low-speed ball milling at 150 rpm with alternating 2-minute milling and 2-minute rest periods over a total duration of 2 hours, or (3) high-speed ball milling at 400 rpm following the same milling/rest cycle for 3 hours. Increasing the intensity of mixing results in a larger interfacial area between the electrically resistive electrolyte and conductive carbon additive.

3.1.2. Sample preparation

Half-cells were assembled by first pre-compressing 80 mg of argyrodite (Li_6PS_6Cl) at 0.5 tons in a 10 mm diameter cell sleeve. Argyrodite is selected as an electrolyte as it forms a stable interface with the Li-In anode under sufficiently low current densities[70]. Subsequently, 30 mg of the 5:1 mixture halide-carbon mixture was added–unless otherwise specified–and compressed at 2.5 tons for 5 minutes. Each layer was first evenly distributed by hand and lightly compacted before final compression by means of a pellet press at the specified pressure. Manual pre-compaction was carried out by pressing both sides of the cell and rotating in a single direction–rather than using a zigzag motion–to avoid the risk of short circuiting. The Li-In anode alloy was prepared by first removing surface oxidation from a lithium disc through gentle scratching. The disc was then flattened using a metal roller, and a ~2 mg lithium disc was punched out. This lithium piece was manually pressed on a ~55 mg indium disc using the flat side of the metal roller. The Li-In disk was placed on the anode side with indium facing the electrolyte, and was covered with a piece of copper foil which acted as a current collector. The half-cell was subsequently compressed at 0.5 tons to form the Li-In alloy (containing ~3.5 wt% lithium metal) and was secured in place using three insulated screws. A photograph and a cross-sectional schematic of the half-cell assembly are provided in Figure 3.1.

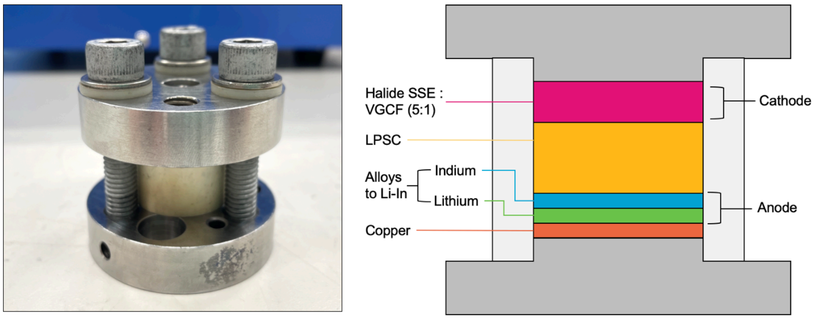

Figure 3.1: Half-cells used in this study. Left: photograph of an assembled cell, with the sleeve pressed in between the cathode and anode that are secured by means of three screws. Right: A cross-sectional schematic depicting the stacking order of the layers in the half-cell assembly (not to scale).

Note that the half-cell employs a Li-In alloy as the anode. Consequently, the measured cell voltage is referenced against the Li-In alloy. According to previous studies, the potential against the Li-In alloy is approximately 0.62 V higher than the standard Li/Li^+ reference potential when the lithium content ranges from >0 to 4.9 wt%[71], as presented in Figure A.1. The lithium concentration remains within this range in all the experiments presented in this work. To ensure consistency and enable comparison with literature, all voltages are reported versus Li/Li^+ by adding 0.62 V to the measured potentials.

SE pellets were prepared by placing 100 mg of the halide SE in a 10 mm diameter cell sleeve and evenly distributing the powder by hand–unless otherwise specified. The powder was then lightly compacted by hand before being pressed at 2.5 tons for 5 minutes and secured in place using three insulated screws. Following the measurement, the pellet was carefully removed by pressing it out from the top of the sleeve using a 10 mm diameter pin and a mechanical press. The pellet thickness was measured using an electronic thickness gauge.

3.1.3. Potentiostatic electrochemical impedance spectroscopy

Electrochemical Impedance Spectroscopy (EIS) is a powerful analytical technique that can be employed to characterise a wide variety of electrochemical material properties. In an EIS experiment, a sinusoidal signal–either AC current or AC voltage–is applied to an electrochemical system over a range of frequencies, while the corresponding sinusoidal response–voltage or current, respectively–of the system is measured[72]. This work uses potentiostatic electrochemical impedance spectroscopy (PEIS), where the system is perturbed with an AC voltage and the AC current response is recorded.

PEIS data are generally presented either as a Bode plot, which shows the impedance magnitude and phase angle as a function of the applied frequency, or as a Nyquist plot, which plots the negative imaginary component of the impedance (Im(Z)) against the real component (Re(Z))[73]. This work employs Nyquist plots to determine ionic conductivities. For this purpose, a pellet of the solid electrolyte is exposed to an AC voltage with an amplitude of 10 mV, across a frequency range from 7 MHz down to 100 mHz. A representative Nyquist plot obtained in this study is shown in Figure 3.2

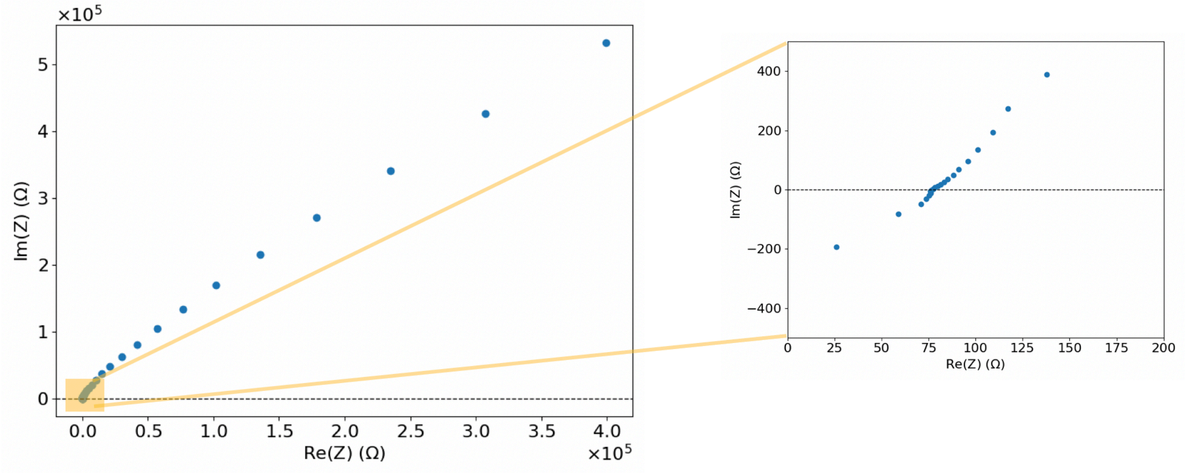

Figure 3.2: Typical Nyquist plot obtained in this study. Frequency decreases along the data points from left to right. The figure on the right provides a magnified view highlighting the high-frequency x-intercept.

PEIS can differentiate between electrochemical processes based on their frequency-dependent response. At sufficiently high frequencies, the influence of capacitive and interfacial behaviour become negligible, so that the measured impedance approaches the system's Ohmic resistance[72]. In the case of a solid electrolyte, this Ohmic resistance is dominated by the bulk ionic resistance of the material, with minor contributions from other resistive elements such as wiring and current collectors[74]. Thus, the ionic resistance can be approximated by the high-frequency intercept on the real axis of the Nyquist plot[74]. This ionic resistance can then be used to find the ionic conductivity (σ_i) using the following relation[75]:

$$\sigma_i = \frac{1}{R} \times \frac{l}{A} \tag{3.1}$$

where R is the ionic resistance in Ω, identified as they high-frequency intercept of the Nyquist plot, l is the sample thickness in m, and A is the cross-sectional area of the sample in m^2.

3.1.4. Direct current polarisation

Direct current (DC) polarisation is employed to determine the electronic conductivity of halide electrolytes. A constant voltage of 2.5 V is applied across an electrolyte pellet, and the resulting current is recorded over time. Initially, mobile lithium ions within the crystal structure Li_xMCl_6 contribute to charge transport. However, as the supply of mobile lithium ions becomes depleted, the current stabilises, with only electrons contributing to the remaining charge transport. In this work, the steady-state current after 5 hours was recorded and used to calculate the electronic conductivity (σ_e) using the following relation:

$$\sigma_e = \frac{I}{U} \times \frac{l}{A} \tag{3.2}$$

where I is the current after 5 hours in Ampere, U the applied potential in V, l the thickness of the pellet in m, and A the area of the pellet in m^2. Figure 3.3 provides a typical DC polarisation plot obtained in this study.

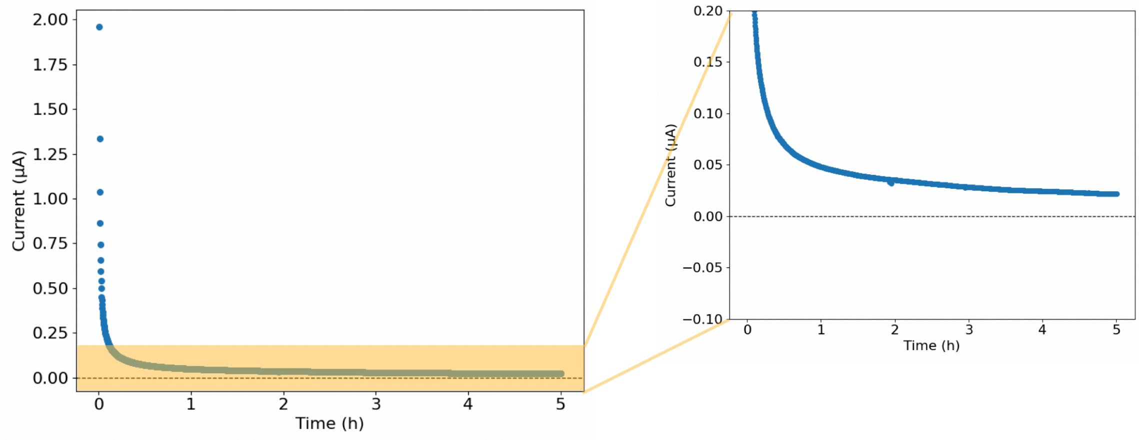

Figure 3.3: Typical DC polarisation plot obtained in this study. The figure on the right provides a magnified view that displays the stabilisation of current over time.

3.1.5. Galvanostatic discharge

During a galvanostatic discharge measurement, a half-cell is discharged at a constant current while the voltage is continuously monitored over time. The resulting voltage profile provides valuable insight into several aspects of cell behaviour, including internal resistance and energy density of the half-cell. It also reveals information about the nature of redox reactions: a sloping voltage profile indicates a solid-solution single-phase mechanism, whereas a voltage plateau indicates a two-phase phase separation process[76].

This work applies galvanostatic discharge to half-cells with an electrolyte-VGCF cathode to assess stability upon lithium insertion. First, the half-cell is rested for 4 hours to allow for the stabilisation of the lithium-indium alloy. Next, the cell is discharged at a current of 100 μA–corresponding to 0.127 mA/cm^2–to the cut-off voltage or cut-off lithiation level. The recorded voltage is plotted against the specific capacity, which corresponds to the amount of charge stored in the cathode per mass unit, and is calculated using the following expression:

$$C_s = \frac{I \times t}{m} \tag{3.3}$$

where C_s is the specific capacity of the capacity in mAh/g, I the discharge current in mA, t the discharge time in hours, and m the mass of the cathode in grams. Further, when lithiation level is used as a cut-off value, the discharge time t in seconds is determined using the following relation:

$$t = \frac{n_{Li} \times F}{I} \tag{3.4}$$

where n_{Li} is the number of moles of lithium, I is the current in Ampere, and F is Faraday's constant of 96,486 C/s. After discharge, the cell is rested for 8 hours prior to any post-discharge characterisation.

3.1.6. Galvanostatic cycling

Galvanostatic cycling involves charging and discharging a cell at a constant current over multiple cycles, providing insight into cycle life, reaction reversibility, capacity retention, and electrochemical stability. In this work, the assembled half-cell is first rested for 4 hours before being discharged to the lower voltage cut-off value. A rest period of 5 minutes follows, before the cell is charged to the upper voltage cut-off value. This is again followed by a 5-minute rest period, prior to the subsequent discharge cycle.

As was the case for the galvanostatic discharge protocol, the battery is rested for 8 hours before any post-cycling characterisation is done.

Unless otherwise specified, a current of 200 μA–corresponding to 0.255 mA/cm^2–is used and the cell is cycled for five cycles. The contribution of VGCF to the observed capacity is neglected, as it exhibits negligible electrochemical activity at the lowest cut-off voltage used in this study (0.6 V vs. Li/Li$^+$), as presented in Figure A.2.

3.1.7. X-ray diffraction

X-ray diffraction (XRD) is an analytical technique used to investigate the crystallographic structure of a material by analysing how incident X-rays interact with the material. During an XRD measurement, X-rays are directed at the crystal across a range of angles, and the intensity of the reflected X-rays recorded, as shown in Figure 3.4.

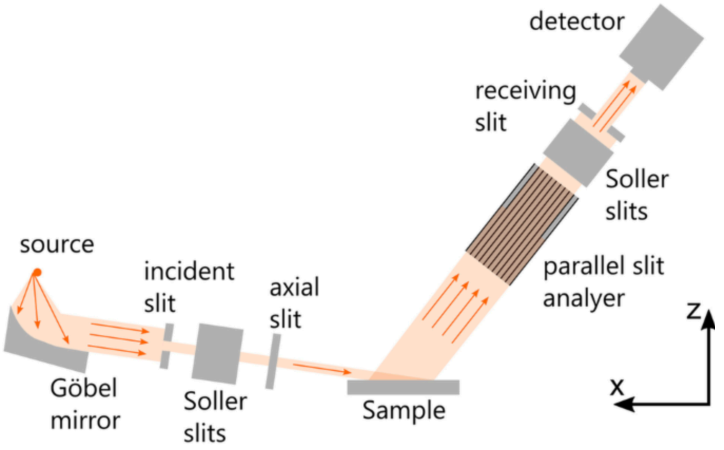

Figure 3.4: Schematic illustration of the experimental setup for an XRD measurement, showing the incident and reflected X-ray beams used to determine crystallographic information. Reproduced from Harrington and Santiso [77].

As X-rays penetrate the material, they interact with regularly spaced crystal planes. More specifically, constructive interference–and thus high-intensity diffraction–occurs when the path travelled between two crystal planes meets the conditions of Bragg's law[78]:

$$n\lambda = 2d \sin\theta \tag{3.5}$$

where n is an integer, λ is the wavelength of the X-rays, d is the distance between lattice planes, and θ is the angle between the X-rays and the lattice plane. Consequently, constructive interference occurs at a larger angle θ for a shorter interplanar spacing d. A visual representation is provided in Figure 3.5.

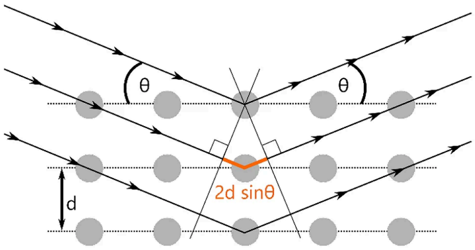

Figure 3.5: Illustration of Bragg's law. Reproduced from Harrington and Santiso [77].

In practice, multiple planes within the crystal can satisfy Braggs law, producing a series of diffraction peaks, each corresponding to a different plane. The orientation of these planes is described using

Miller indices, denoted as (hkl). This is a shorthand notation based on the reciprocals of the fractional intercepts that a given plane makes with the crystallographic axes[79].

This work uses an XPert-Pro diffractometer from PANalytical, equipped with a copper K-α (Cu Kα) radiation source (λ = 1.5406 Å), operating at 40 mA and 45 kV. Powder samples were placed in an airtight holder containing a zero-diffraction silicon wafer to minimise background noise. For XRD analysis of the cathode from a used half-cell, the cell is opened on the cathode side and carefully scratched with tweezers or a spatula to free powder from the cathode and minimise mixing in of other materials from the battery (such as the electrolyte). The powder was scanned over a 2θ range from 10° through 80°. The resulting XRD pattern, with intensity plotted against 2θ, allows for material characterisation, including lattice parameters, phase composition, and purity.

Selected XRD patterns were subjected to Le Bail refinement to obtain refined lattice parameters and cell volumes. This fitting method matches a calculated profile to experimentally observed diffraction data while refining the unit cell and peak-profile parameters, solely requiring the compound's space group as an input[80]. The monoclinic structure of $Li_{2.5}In_{0.5}Zr_{0.5}Cl_6$ reported by Helm *et al.* [9] provided the initial space group and approximate lattice parameters. Refinements were performed with GSAS-II[81].

3.2. Computational methods

Monoclinic 2 × 1 × 2 supercells for LZC, LIC, LIZC and H4 were created with the VESTA[82] software by adapting the C2/m crystallographic data previously reported for LIC[9]. Helm *et al.* [9] found, through Rietveld refinement, a partial occupancy of the *4g* position in LIC (0.05) and LIZC (0.19). Therefore, two structures were studied for the monoclinic crystals: one with full occupancy at the *2a* Wyckoff position (ordered) and one with one of the metal cations located at the *4g* Wyckoff position (disordered), corresponding to a partial occupancy of 0.12. Unless noted otherwise, the disordered structures were used in computational analyses. The locations of the metal cations in the resulting supercells are presented in Figure 3.6.

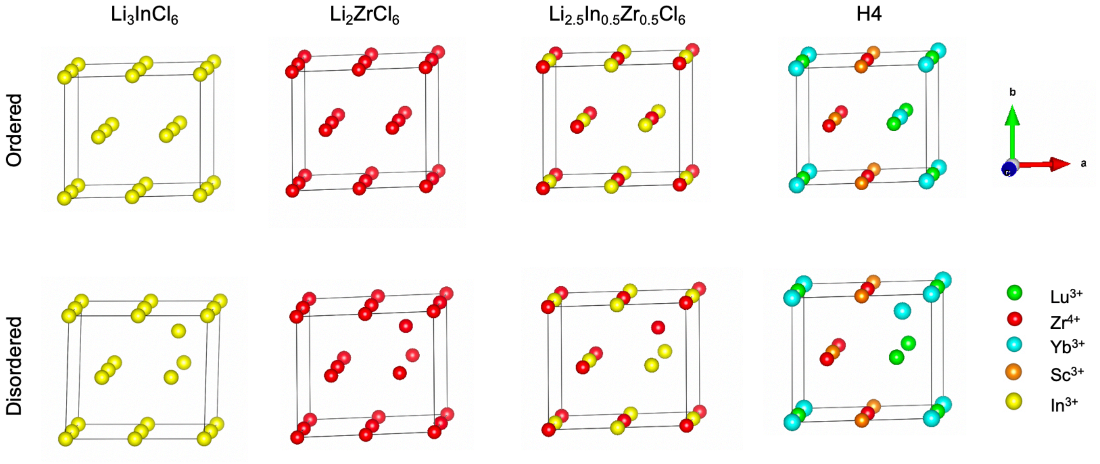

Figure 3.6: Overview of the positions of the metal cations M^{x+} in the monoclinic 2 × 1 × 2 supercells used for computational analysis.

The term "disordered" in the context of the supercells shown in Figure 3.6 refers specifically to a positional disorder in which one cation is relocated to the *4g* site with a lower occupancy within the structure. Due to the limited size of the supercell and the artificial periodicity imposed by periodic boundary conditions in DFT simulations, both structures maintain a high degree of order overall.

The appropriate amount of Li atoms was obtained in the supercell by first generating 100,000 structures in which Li was placed randomly in the 72 available tetrahedral and octahedral sites. From these structures, the 10 structures with the largest Li-Li distance were selected to start DFT relaxations. These structures are expected to be energetically favoured, because Coulombic interactions between positively charged lithium cations are minimised[50].

3.2.1. Density Functional Theory relaxations

DFT calculations were performed using the Vienna Ab initio Simulation Package (VASP 6.3.2)[83]. The Perdew-Burke-Ernzerhof functional for solid-state systems (PBE-sol) was used[84]. This is a widely used generalised-gradient approximation (GGA)[85] functional in which the exchange-correlation energy depends both on the local electron density and its gradient. Projected augmented wave (PAW)[86] potentials were used to reduce computational cost by only considering the atom's valence electrons, which are tabulated in Table 3.2.

Table 3.2: The valence electrons considered in PAW potentials used in this study[83].

Element	Number of valence electrons	Valence electron configuration
Li	1	$2s^1$
Cl	7	$3s^2\ 3p^5$
Lu	9	$5p^6\ 5d^1\ 6s^2$
In	13	$4d^{10}\ 5s^2\ 5p^1$
Sc	11	$3s^2\ 3p^6\ 3d^2\ 4s^1$
Yb	9	$5p^6\ 5d^1\ 6s^2$
Zr	12	$4s^2\ 4p^6\ 4d^3\ 5s^1$

A plane-wave energy cut-off of 400 eV was used and spin-polarisation was considered. The electronic self-consistency loop was converged to an energy threshold of 10^{-5} eV, and the ionic relaxations were considered converged when the maximum force on any atom fell below 0.02 eV/Å. A k-mesh of 3 × 3 × 3 over Γ was used. For the convex hull calculations, the structure was first relaxed with respect to atomic positions, cell volume, and cell shape before a second static relaxation was performed in which only electron densities were relaxed.

Next, the formation energies of the least lithiated and most delithiated structures were equated to zero, and the formation energies of the other relaxed structures were plotted relative to these two endpoints. The formation energy E_{form} was thus calculated by[62]:

$$E_{\text{form}}(x) = E_0(x) - [x_{\text{norm}} \times E_{\text{max}} + (1 - x_{\text{norm}}) \times E_{\text{min}}] \tag{3.6}$$

where E_0 is the formation (ground-state) energy of the compound, E_{min} is the formation energy of the least lithiated structure, E_{max} is the formation energy of the most lithiated structure, and x_{norm} is a normalisation parameter that varies from 0 (least lithiated composition) to 1 (most lithiated composition). The lowest energy structures are connected by means of a convex hull. The formation energy may be interpreted as the Gibbs free energy, since the 0 K temperature used during structural relaxation eliminates entropic contributions[87].

Next, the voltage profile is obtained by comparing the formation energies and lithium concentrations of the compounds on the convex hull. Taking Li_2ZrCl_6 as an example, the reaction upon addition or removal of lithium looks as follows:

$$\mathrm{Li_2ZrCl_6} + \text{(x-2)}\,\mathrm{Li} \longrightarrow \mathrm{Li}_x\mathrm{ZrCl_6} \tag{3.7}$$

where the electrolyte is oxidised for x < 2 (Li is removed) and it is reduced for x > 2 (Li is added). The energy required to add or remove lithium to the electrolyte is described by the difference in Gibbs free energy (ΔG) of the reaction for a specific value of x. This determines the average voltage $\bar{V}$ with respect to the Li/Li^+ redox couple by[51]:

$$\bar{V} = -\frac{\Delta G}{n} = -\frac{E(\mathrm{Li}_x\mathrm{ZrCl_6}) - E(\mathrm{Li_2ZrCl_6}) - (x-2)E(\mathrm{Li})}{x-2} \tag{3.8}$$

where n is the number of electrons transferred, ΔG is the Gibbs free energy of the reaction in eV, and $E(\mathrm{Li}_x\mathrm{ZrCl_6})$ and $E(\mathrm{Li_2ZrCl_6})$ are the formation energies of the stable respective compounds on the convex hull. The intrinsic stability window–the voltage range over which no redox reactions take place–is calculated by taking the first concentration right and left to the stable concentration to find the oxidation and reduction potential.

Density of states

Density of states (DOS) calculations were performed following structural relaxation for some stable structures (i.e. structures on the convex hull) to analyse electronic structures. First, a static relaxation is performed, where the wave functions and charge density are saved. Next, the DOS calculation is performed using the relaxed structure, wave functions, and charge density as inputs. A k-mesh of $5 \times 5 \times 5$ over Γ was used and ionic relaxation was turned off. A dense DOS sampling of 3000 points was used and the partial DOS was calculated using the LORBIT = 11 setting to enable projection onto atomic orbitals. A plane-wave energy cut-off of 400 eV was used, with an energy threshold of 10^{-5} eV.

Charge density

Charge density calculations were performed following structural relaxation to analyse the spatial redistribution of electron density upon lithiation. First, an additional ionic relaxation was performed using the same computational parameters as used in the initial structure relaxation, differing only in that the volume is kept constant and magnetisation is considered. The initial magnetic moments were set to 0 μ_B for lithium, chlorine, and zirconium atoms. Second, a static SCF calculation was performed on the relaxed structure to obtain the electron density, using the same magnetisation settings and a plane-wave energy cutoff of 400 eV, with a k-mesh of $3 \times 3 \times 3$ over Γ. The electronic self-consistency loop was converged to an energy threshold of 10^{-6} eV.

To compute the charge density difference upon lithiation, two reference structures were created: (1) a delithiated structure formed by randomly removing lithium atoms until the undoped concentration is achieved (x = 2 for Li_2ZrCl_6), and (2) a structure composed solely of the removed lithium atoms. Both references were treated with the same static SCF calculation described above. The charge density difference ($\Delta\rho$) could now be found using[88]:

$$\Delta\rho = \rho_{AB} - \rho_A - \rho_B \tag{3.9}$$

where ρ is the charge density in electrons/Å^3, AB corresponds to the lithiated structure, A to the undoped structure, and B to the isolated lithium atoms.

3.2.2. Molecular dynamics simulations

Ab initio molecular dynamics (AIMD) simulations were used to predict the stability of the structures studied beyond their reduction potential by simulating movements of atoms over time when kinetic energy is provided to the structure (i.e. non-zero temperature is introduced). The AIMD simulations were performed in the NVT ensemble with a time step of 2 fs, using the Nosé-Hoover thermostat[89],[90] at 400 K and gamma-point only sampling. The same GGA pseudopotentials, plane-wave energy cut-off and electronic convergence threshold were used as in the DFT calculations. The simulation time was 100 ps, unless otherwise specified. Structural breakdown within the 100 ps simulation is considered a strong indicator of instability, whereas the absence of breakdown only suggests–rather than confirms–that the structure may be stable. The data was interpreted and analysed by the Python packages GEMDAT[91] and Pymatgen[92].

4

Results and Discussion

The broad topic of investigating low-voltage stability of zirconium(IV)-based halide monoclinic solid electrolytes was narrowed down to three main steps. First, the low-voltage behaviour of monoclinic Li_2ZrCl_6 was studied. Second, the effect of Zr^{4+}-substitution in Li_3InCl_6 was evaluated by studying the compound $Li_{2.5}In_{0.5}Zr_{0.5}Cl_6$. Finally, high-entropy materials were explored where Zr^{4+} is part of a multi-cation environment.

4.1. Monoclinic Li_2ZrCl_6: studying zirconium in single-cation system

In this section, the low-voltage stability of monoclinic LZC is studied both computationally and experimentally. First, the results of fine-tuning the synthesis of monoclinic LZC are shared, after which its experimental low-voltage stability is studied by discharging and cycling into the low-voltage region. Computational methods are then employed to explore the material's behaviour at the atomistic level. Finally, a brief note is made on an intriguing observation of phase conversion between monoclinic and trigonal LZC.

4.1.1. Synthesis of monoclinic Li_2ZrCl_6

Li_2ZrCl_6 has been widely explored in its trigonal phase[24],[93] but has only recently been reported in a monoclinic structure[25], which is why synthesis parameters to obtain monoclinic LZC–determined primarily by the annealing temperature–have not been extensively reported in the literature. First, precursors were mixed by means of high-speed ball milling at 550 rpm for 12 hours, before the mixture was annealed. Subsequently, a 5:1 LZC:VGCF composite was prepared for incorporation into the cathode of a half-cell, enabling the evaluation of low-voltage stability. Figure 4.1 presents the X-ray diffraction patterns of the resulting compounds, including samples annealed at two different temperatures: 310 °C and 350 °C.

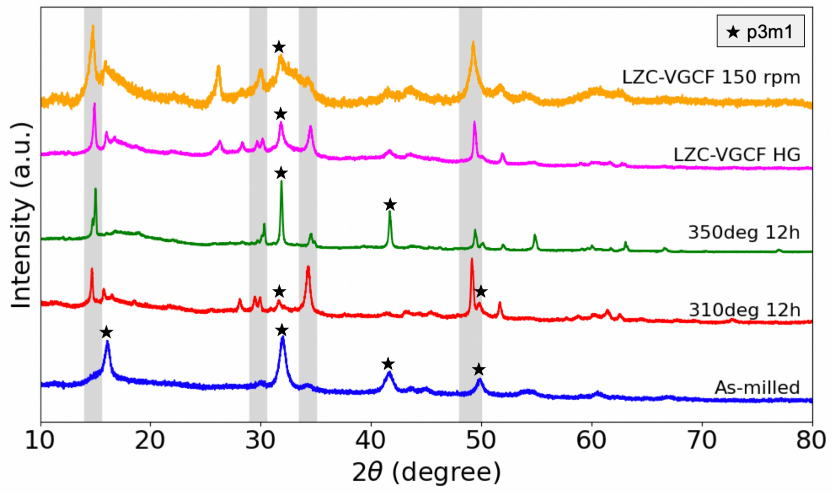

Figure 4.1: X-ray diffraction patterns of LZC at different synthesis stages and under various conditions. Patterns show LZC after ball milling (as-milled) and after annealing at 310 °C and 350 °C. VGCF composites were prepared using the sample annealed at 310 °C, either by hand grinding (HG) or by low-speed ball milling at 150 rpm. The shaded regions indicate typical diffraction ranges for the C2/m phase, while stars indicate reflections indicative of a P3m1 phase[9],[94].

Figure 4.1 shows that low-speed ball milling results in the formation of a trigonal phase, as evidenced by the characteristic peaks at $2\theta = 16.0°$, $32.0°$ and $41.6°$, consistent with previous reports[22]. Although prior work achieved a complete conversion from the trigonal to monoclinic phase by annealing at 350 °C for 5 hours[22], in this study these conditions instead resulted in a more crystalline trigonal structure–evidenced by the sharpening of peaks at the same 2θ positions as those in the as-milled sample. Therefore, a lower annealing temperature of 310 °C was used with a longer annealing time of 12 hours, remaining within the reported conversion range of 277 °C to 350 °C[22]. This treatment resulted in a major monoclinic phase, as indicated by the peaks appearing in the shaded regions. Minor reflections corresponding to a residual trigonal structure remained present, which were also present at lower intensity in the XRD patterns of the monoclinic phase synthesised by Wang *et al.* [22].

The subsequent step of preparing a 5:1 LZC mixture annealed at 310 °C with VGCF presented a notable challenge: the VGCF must be well dispersed to ensure sufficient electronic conductivity in the cathode, while preserving the crystalline monoclinic phase. Achieving good electronic contact typically requires thorough ball milling, but ball milling can, in turn, facilitate the reconversion of the monoclinic phase to the trigonal phase. As shown in Figure 4.1, ball milling at 150 rpm for 2 hours produced a mixed-phase material with reduced crystallinity, evidenced by broad diffraction peaks and reflections corresponding to both the trigonal phase (e.g. $2\theta = 32.0°$) and the monoclinic phase (in the shaded regions). In contrast, hand-grinding the mixture produced a significantly more crystalline and phase-pure spectrum, with minimal conversion to the trigonal structure. Although the hand-ground sample preserves the monoclinic phase more effectively, it may suffer from insufficient surface area between the electrically conductive additive and resistive electrolyte, due to less thorough mixing. Conversely, the ball-milled composite, despite exhibiting a larger fraction of the trigonal phase, is expected to offer a larger surface area and thereby limit transport limitations. Therefore, both mixing methods were investigated in subsequent experiments.

4.1.2. Experimental performance of Li_2ZrCl_6

First, the ionic conductivity of the obtained structures was investigated by means of PEIS (see Figure A.8 and Table A.2). The monoclinic LZC synthesised in this study displays an ionic conductivity of 0.008 mS/cm, which corresponds well with the previously reported value of 0.007 mS/cm[25]. The as-milled trigonal sample displayed a significantly higher ionic conductivity of 0.6 mS/cm–slightly exceeding values reported in literature of 0.3 - 0.4 mS/cm[23],[24]. The difference may stem from more thorough ball milling conditions used by the authors, which typically reduces grain sizes and thereby increases resistance resulting from grain boundaries, consequently reducing ionic conductivity[95]. Although the ionic conductivity of monoclinic LZC is insufficient for use as a solid-state electrolyte, its anodic stability remains of interest for the broader investigation of zirconium(IV)-based SEs that may offer both adequate ionic conductivity and favourable low-voltage stability.

The low-voltage stability of LZC was assessed experimentally by utilising LZC-VGCF as the cathode of a half-cell, using argyrodite as the electrolyte, and a Li/In alloy serving as an anode. First, the half-cell was discharged at a constant current to various depths of discharge–where a higher depth corresponds to a higher lithium concentration (x) in the cathode and a lower cell voltage. XRD measurements were then taken to observe any structural changes. Second, the half-cell was cycled over a voltage window of 0.6-3.6 V. Figure 4.2 presents the discharge and cycling profiles of LZC, along with the associated XRD patterns used to monitor any structural changes.

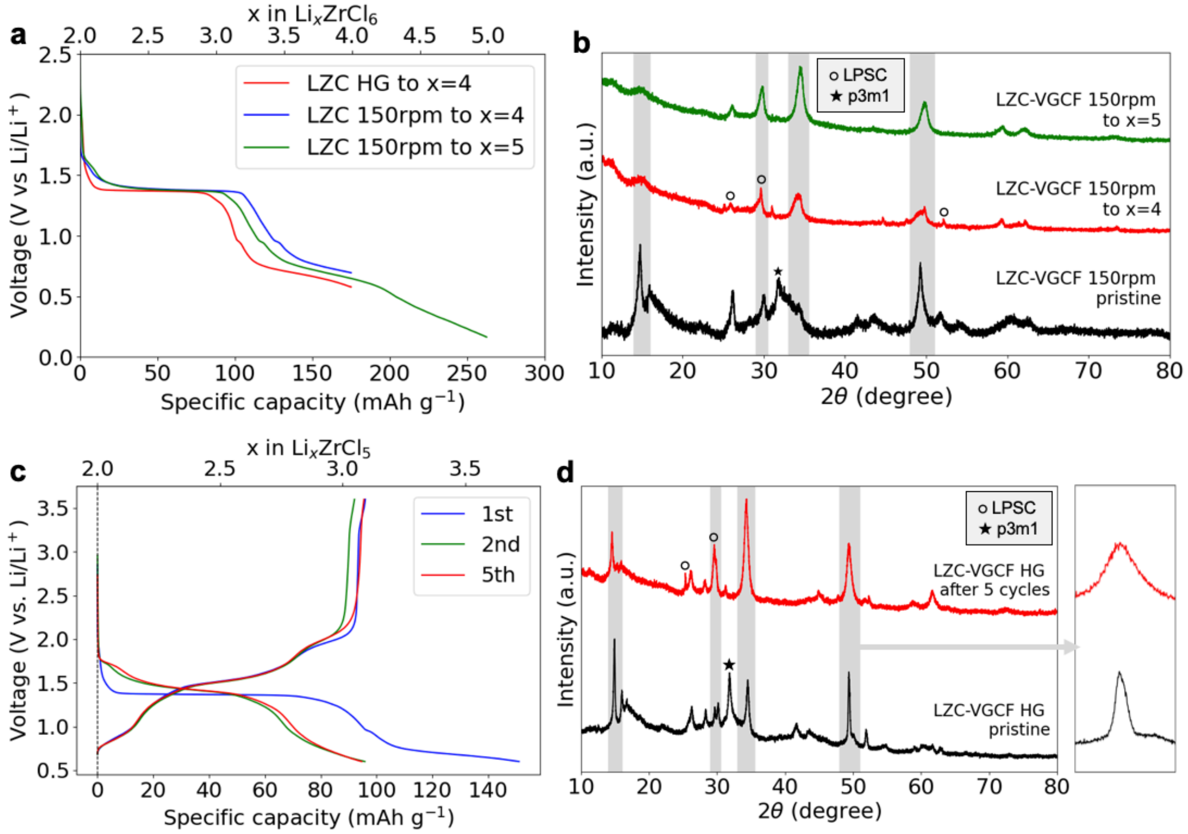

Figure 4.2: Galvanostatic performance of LZC. a,b, Discharge curves of hand-ground (HG) and ball-milled (150 rpm) LZC, with XRD patterns showing the resulting structure at different depths of discharge of the ball-milled sample. **c,d,** Galvanostatic cycling voltage profile of hand-ground LZC, with corresponding XRD patterns of the pristine and cycled materials.

From Figure 4.2a it can be observed that the onset potential of LZC is measured at 1.7 V, indicating the onset of lithium insertion into the halide cathode and the associated reduction process. This marks the reduction limit of the intrinsic electrochemical stability window. Notably, this value is close to the reduction potential of the Zr^{4+}/Zr^0 redox couple of 1.59 V vs. Li/Li$^+$[96] and corresponds well with the computationally found value of 1.75 V[22]. Discharging the half-cell with the ball-milled composite to a lithium concentration of $x = 4$ (0.6 V) and $x = 5$ (0.2 V) retained the monoclinic structure, as evidenced by the characteristic monoclinic peaks in the shaded regions of the XRD patterns (Figure 4.2b). This is further supported by the absence of peaks corresponding to metallic zirconium, suggesting that the material was lithiated without undergoing decomposition. It should be noted that sharp reflections associated with argyrodite (e.g. at $2\theta = 25.6°$, $29.7°$, and $52.6°$) may appear in any XRD pattern obtained from non-pristine samples. This is attributed to unintentional mixing of the electrolyte into the cathode material during sample collection, as the argyrodite phase is easily transferred when scratching the thin electrode layer. The hand-ground composite exhibits comparable discharge behaviour, although with a shorter voltage plateau compared to the ball-milled sample. This difference likely stems from less uniform mixing of VGCF within the halide, resulting in regions of limited electronic connectivity and hence lower lithiation activity.

The cell cycling data presented in Figure 4.2c shows a first-cycle capacity retention of 73%, with the specific capacity dropping from 155 mAh/g to 97 mAh/g. The voltage profile also shows a distinct voltage plateau at 1.4 V during the first discharge, while subsequent cycles exhibit a more sloping voltage profile where the remaining capacity is well retained. At the same time, Figure 4.2b and d reveal that the minor trigonal phase disappeared upon discharge and after cycling. Therefore, the plateau at 1.4 V may correspond to a two-phase reaction involving the structural conversion from the trigonal to the monoclinic phase–which will be further explored in subsection 4.1.4. Alternatively, it could indicate the formation of, for example, a SEI layer–which is either amorphous or very thin so that it is not detected in the XRD pattern.

In subsequent cycles, the sloping voltage profiles are indicative of reversible lithium insertion in a solid-solution fashion, where ~1.0 mole of electrons/lithium can be stored reversibly per mole of LZC. A last observation to make from Figure 4.2b and d is the irreversible peak broadening after discharge, which may be attributed to a reduction in crystallite size or an increase in structural disorder induced by lithium insertion[97].

4.1.3. Computational study of low-voltage behaviour in Li_2ZrCl_6

As a next step, density functional theory and *ab initio* molecular dynamics were deployed as atomistic tools to gain deeper insights into the behaviour of LZC. A 2 × 1 × 2 monoclinic supercell was constructed, with one zirconium cation occupying the *4g* Wyckoff position instead of the *2a* site. Since no experimental studies have been published that provide the occupancy ratio of these specific sites in LZC, the reported site occupancies in related compounds such as Li_3InCl_6 and $Li_{2.5}In_{0.5}Zr_{0.5}Cl_6$ were used as a reference[9]. To evaluate the stability of LZC under increasing levels of lithiation, structures with various lithium contents were relaxed using DFT and subsequently used to construct a convex hull along with the associated voltage profile. The stability of selected structures on the hull was further assessed through 100 ps MD simulations. Figure 4.3 presents the convex hull and voltage profile, the structures after MD simulations, and the radial distribution frequency (RDF) derived from the MD trajectories.

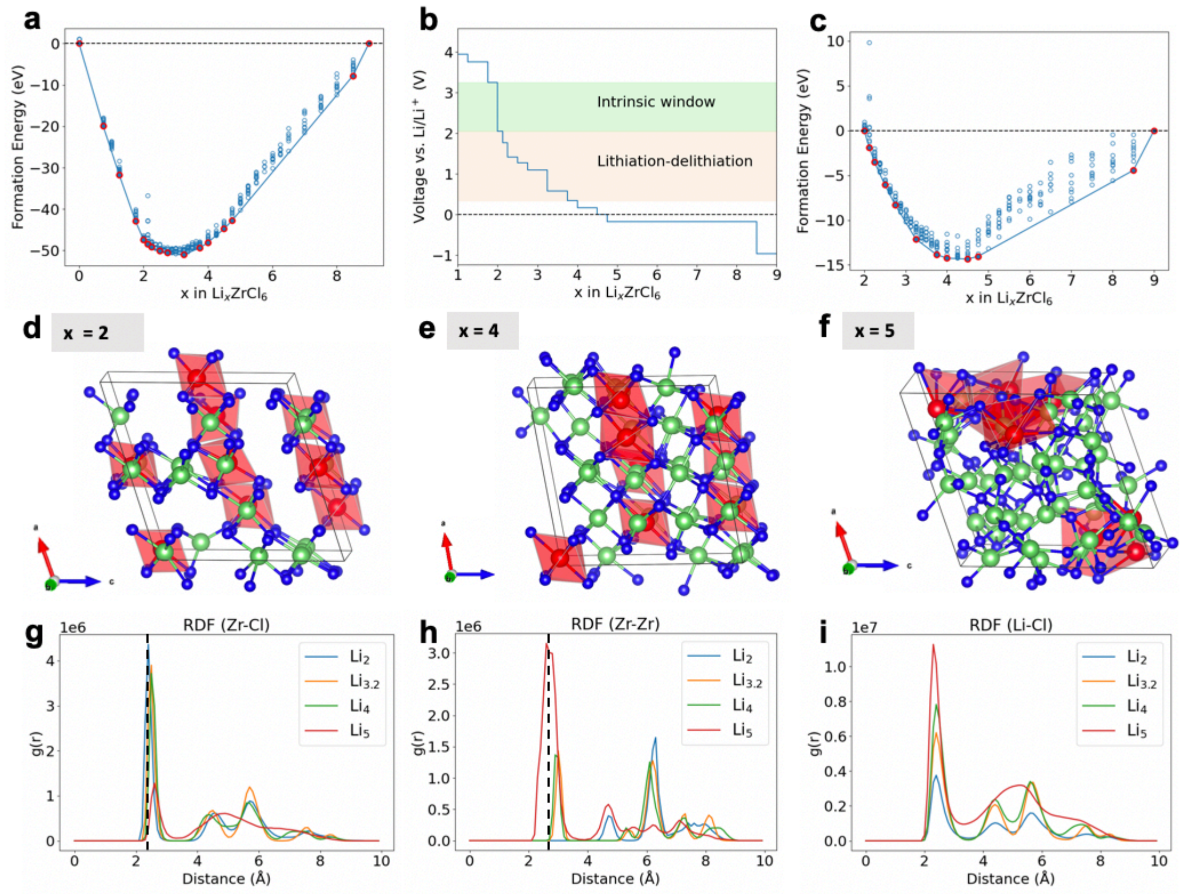

Figure 4.3: Stability window of LZC as defined by DFT and MD calculations. **a,** Formation energies of Li_xZrCl_6 with respect to the completely delithiated and lithiated states. The convex line follows the lowest energy path–indicating the stable configurations along the range. **b,** Corresponding voltage profile indicating the intrinsic window and lithiation/delithiation region, where lithium insertion is possible without destroying the monoclinic structure. **c,** The reduction part of the convex hull, where Li_2ZrCl_6 and Li_9ZrCl_6 are taken as references. **d-f,** Configurations after a 100 ps AIMD simulation at 400 K of the **(d)** unlithiated Li_2ZrCl_6 compound, **(e)** Li_4ZrCl_6 compound in the lithiation/delithiation region, and **(f)** Li_5ZrCl_6 phase that shows structural decomposition. Zirconium is shown in red, chlorine in blue, and lithium in green. **g-i** Radial distribution frequency plots from 100 ps AIMD simulations at 400 K comparing **(g)** Zr-Cl, **(h)** Zr-Zr, and **(i)** Li-Cl distances.

The DFT results shown in Figure 4.3a-c predict an intrinsic electrochemical stability window of 2.0 (reduction limit) to 3.2 V (oxidation limit)–defined by the voltage required to start adding and extracting lithium, respectively. The intrinsic reduction stability of 2.0 V aligns reasonably well with the experimentally observed onset of lithiation at 1.7 V. A possible explanation for the discrepancy could be that LZC, in practice, is more disordered than the disorder reflected in the occupation of one of the *4g* positions by zirconium used in the supercell. Indeed, removing this disordered site in the calculations significantly extends the intrinsic stability window to 1.0 V (see Figure A.3). Although the exact origin of the discrepancy between the ordered and disordered structures remains to be understood, one possibility is that structural disorder introduces localised energy states that destabilise the compound. These states may promote lithium insertion and electron accommodation, thereby reducing the extent to which the voltage must be lowered to initiate reduction.

In addition, it was investigated whether LZC has a lithiation/delithiation region by assessing the structural stability of lithiated phases on the convex hull through 100 ps AIMD simulations at 400 K. As shown in Figure 4.3d-f, zirconium octahedra begin to break at a lithium concentration of x = 5. In contrast, the x = 4 structure (formed at 0.3 V) remained intact throughout the simulation, suggesting it may retain its structure. However, it should be emphasised that AIMD simulations capture only short timescales due to computational constraints, and structural degradation could still occur over longer timescales. Therefore, stability during the AIMD alone does not guarantee long-term stability. The structural difference between the intact x = 4 and broken x = 5 phases is clearly reflected in the radial distribution function plots presented in Figure 4.3g-i. In particular, the clustering of zirconium atoms in the x = 5 structure is evident from the peak at 2.4 Å in the Zr-Zr RDF, and the breakdown of the zirconium octahedra is further indicated by a reduction in peak intensity at 2.2 Å in the Zr-Cl RDF. These findings suggest that the monoclinic structure remains intact at least down to 0.3 V, consistent with experimental results showing successful cycling to 0.6 V.

To investigate the redistribution of electron density in the lithiation/delithiation region of LZC, a charge density difference analysis was performed by comparing the lithiated phase $Li_{3.25}ZrCl_6$ to the unlithiated Li_2ZrCl_6 phase. The resulting charge density difference is illustrated in Figure 4.4.

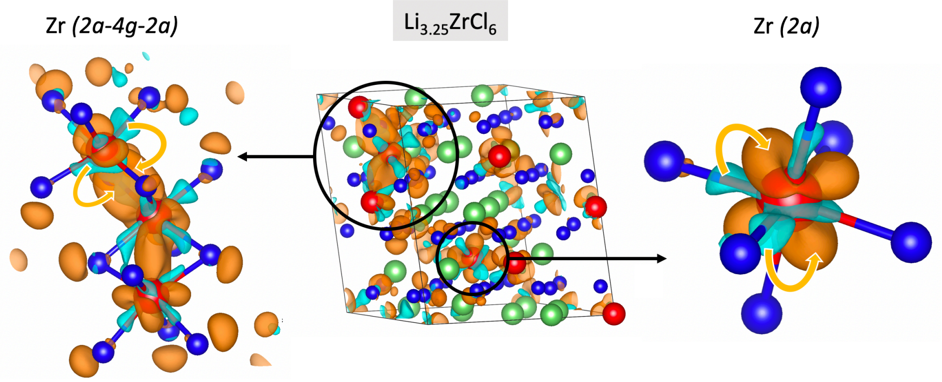

Figure 4.4: Charge density difference plot for a phase within the lithiation/delithiation region ($Li_{3.25}ZrCl_6$). The orange isosurfaces (0.005 $e^-/Å^3$) indicate regions of increased electron density relative to Li_2ZrCl_6, while the blue isosurfaces (-0.005 $e^-/Å^3$) indicate regions of decreased electron density.

Figure 4.4 reveals how the electron density is redistributed upon lithium insertion. At the Zr atoms occupying the *2a* Wyckoff position, electron density is depleted from the Zr-Cl bonding region–where chlorine typically donates electrons from its 3p orbital to the vacant 4d orbital of zirconium–indicating a weakening of the Zr-Cl bond. At the same time, electron density accumulates in non-bonding or anti-bonding d-orbitals on Zr, as evidenced by the orange lobes oriented away from the Zr-Cl bond axes. In the disordered region–featuring a Zr atom in the *4g* Wyckoff position–a similar redistribution is observed. Notably, a pronounced build-up of electron density is observed between the Zr atom in the *4g* site and the neighbouring Zr atoms in the *2a* sites, indicating the formation of Zr-Zr bonding interactions and suggesting the potential for zirconium clustering within the disordered environment. Importantly, this shift in electron density–from Zr-Cl bonding orbitals toward the Zr-Zr region and non-bonding Zr-orbitals–occurs without disrupting the overall crystal structure, as observed from MD simulations and experimental results.

4.1.4. Structural transition from trigonal to monoclinic symmetry at low potentials

As previously briefly noted, an intriguing conversion was experimentally observed in relation to the low-voltage behaviour of LZC: the minor trigonal phase present in the monoclinic LZC sample disappeared when the sample was discharged to 0.6 V and did not reappear upon subsequent recharge (Figure 4.2). To study this conversion in an isolated context, pure trigonal LZC (i.e., the as-milled sample) was subjected to cycling into the low-voltage region, and the structural evolution was examined using XRD, the results of which are presented in Figure 4.5.

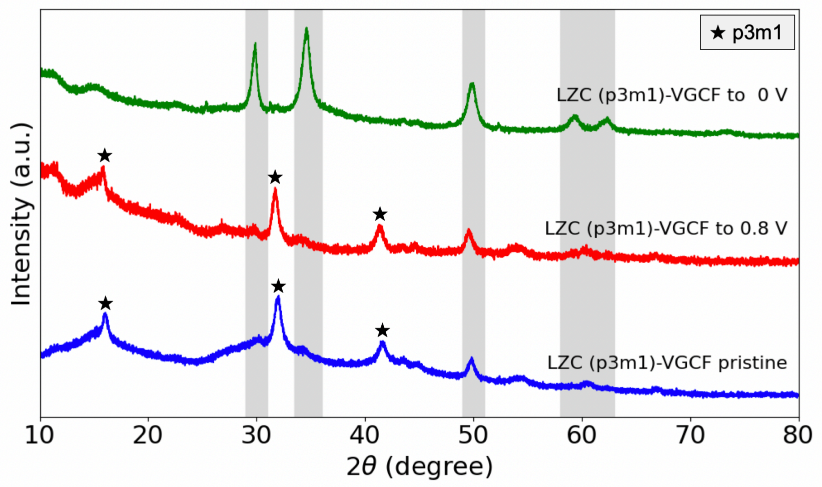

Figure 4.5: X-ray diffraction patterns of trigonal LZC at various states of discharge. Patterns are shown of the pristine sample before discharge, after discharge to 0.8 V, and after discharge to 0 V.

Figure 4.5 shows that the trigonal structure remains intact upon discharge to 0.8 V, with complete conversion to the monoclinic phase having occurred upon discharge to 0 V. This conversion window aligns with the observations of the monoclinic sample containing trigonal impurities in Figure 4.2b, where the trigonal phase had disappeared at voltages of 0.6 V and below. Yet, the hypothesis that the 1.4 V voltage plateau arises from conversion to the trigonal phase is not supported, as this transformation does not occur until the voltage drops below 0.8 V (Figure 4.5). Instead, the voltage plateau may possibly be attributed to a different structural rearrangement within the impure pristine material, contributing to the capacity loss observed during the first cycle (Figure 4.2c).

To gain a deeper insight into the relative energy landscapes of the monoclinic and trigonal structures upon lithiation, their convex hulls were compared. It is worth noting that the 1 × 1 × 2 supercell of trigonal LZC contains more atoms than the 2 × 1 × 2 supercell of monoclinic LZC–six and eight zirconium atoms, respectively. Since the formation energy scales with the number of atoms, Figure 4.6 presents the formation energy per atom to ensure an accurate comparison.

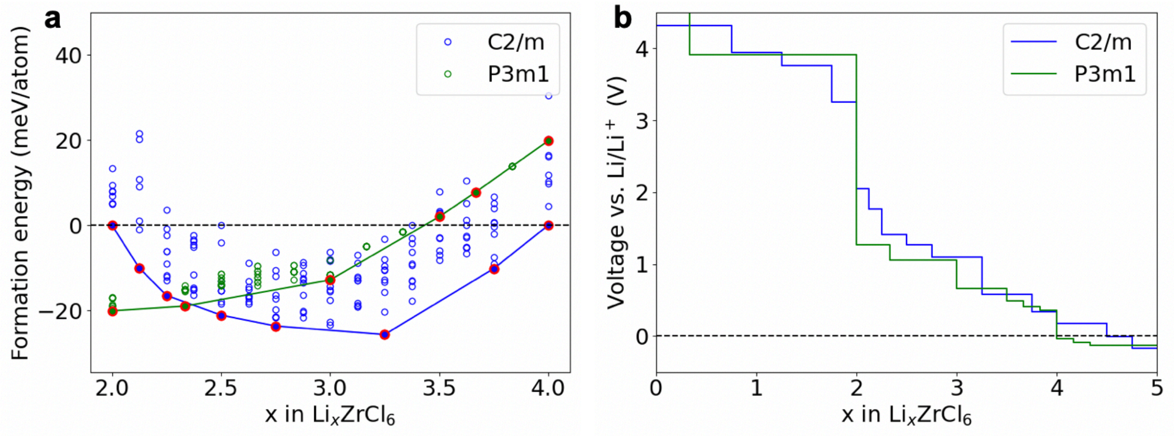

Figure 4.6: Comparison of the thermodynamic energy landscapes for the trigonal and monoclinic structures of LZC upon lithiation. a, Formation energy per atom of monoclinic (C2/m) and trigonal (P3m1) LZC, plotted referenced to the formation energies of monoclinic LZC at x = 2 and x = 4. **b,** Voltage profiles of monoclinic and trigonal LZC as a function of the lithium concentration.

Figure 4.6a demonstrates a thermodynamic driving force that favours the formation of monoclinic LZC at lithium concentrations exceeding x = 2.4, as the formation energy per atom of the monoclinic structure becomes more negative than that of the trigonal structure. This corresponds to a voltage of

~1.3 V (Figure 4.6b)–at least 0.5 V higher than the experimentally observed conversion. This indicates the presence of a kinetic barrier to conversion. While thermodynamically the monoclinic structure might be favoured from 1.3 V onwards, there may be kinetic barriers that hinder its immediate conversion. This kinetic barrier may be overcome by applying lower voltages, which lead to a higher overpotential and therefore provide a stronger driving force that enables the phase transition to proceed.

One feasible explanation for the thermodynamic driving force lies in the number of available lithium sites in each structure. Previous research reports lithium positions in the trigonal phase that allow for the accommodation of lithium up to x = 4, whereas the monoclinic phase has approximately double the available positions reported, equating to hosting lithium up to x = 9[9],[98].

Further investigation of this phase transition mechanism is beyond the scope of this study, which focusses on the comparison of stability amongst monoclinic structures.

4.2. Effects of zirconium(IV) substitution in Li_3InCl_6

While monoclinic LZC exhibits excellent low-voltage stability, its poor ionic conductivity hinders its direct application as a solid electrolyte. In contrast, the monoclinic halide SE Li_3InCl_6 has demonstrated a good ionic conductivity of 1.5-2.0 mS/cm, which was further improved by partial Zr-substitution[36],[99],[100]. Since the impact on Zr-substitution in LIC remains largely uninvestigated[9], the compound $Li_{2.5}In_{0.5}Zr_{0.5}Cl_6$ (LIZC) was synthesised and its low-voltage experimental performance was evaluated and compared to LIC. Next, computational methods are deployed to gain atomistic insights into its behaviour.

4.2.1. Synthesis of LIC and LIZC

Both LIC and LIZC were synthesised using mechanical ball milling followed by annealing. Mixtures in a 5:1 ratio with VGCF were also obtained to allow the implementation of each electrolyte in the cathode. Annealing temperatures were selected based on previous studies: 260 °C for LIC and 350 °C for LIZC[9],[101]. Figure 4.7 presents the XRD patterns of the synthesised materials.

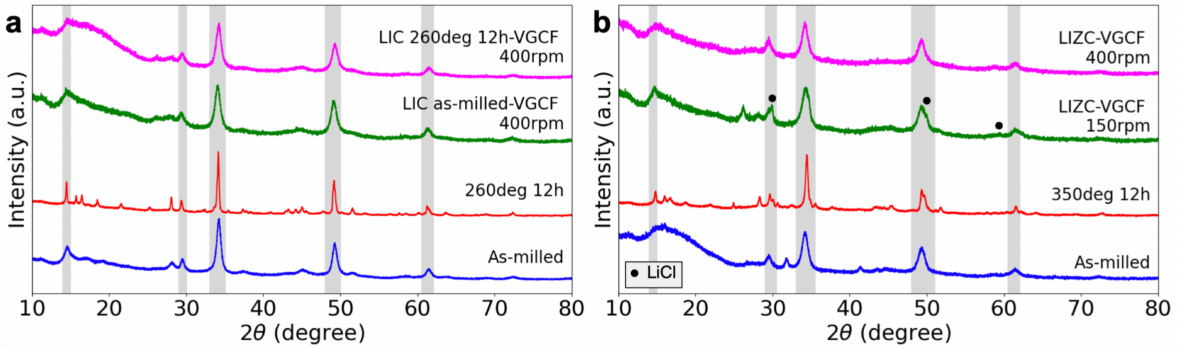

Figure 4.7: X-ray diffraction patterns of LIC and LIZC at various synthesis stages. Samples are shown after ball milling (as-milled), after annealing, and after mixing with VGCF, of **(a)** LIC and **(b)** LIZC.

Figure 4.7 shows that both LIC and LIZC adopt a monoclinic structure after ball milling. Annealing significantly enhances crystallinity in both structures, as evidenced by the narrowing of the diffraction peaks. In the case of LIZC, some minor impurity peaks appear after annealing, which may originate from contamination on the XRD holder or from the ball-mill jars.

Subsequent ball milling of each compound with VGCF maintained the monoclinic structure but reduced crystallinity in both compounds–as evidenced from the broadened peaks–to a degree of crystallinity comparable to the as-milled compounds. This suggests that annealing may be an unnecessary intermediate step–at least for applications that require subsequent ball milling with VGCF.

Furthermore, ball milling LIZC at 150 rpm resulted in the formation of a minor LiCl phase, as evidenced by the appearance of peaks at $2\theta = 34.8°$ and $50.0°$. Given the high electrochemical stability of LiCl, its presence is unlikely to significantly impact the electrochemical behaviour of the compound, although it may contribute to a reduction in specific capacity during galvanostatic measurements. Although samples ball milled at 400 rpm with VGCF do not show clear LiCl peaks, it is possible that these peaks are obscured by the further broadening of the monoclinic diffraction peaks due to more intense ball milling.

4.2.2. Experimental stability of LIC and LIZC at low potentials

First, the ionic conductivity of LIC was determined to be 0.9 mS/cm by means of PEIS (Figure A.8 and Table A.2). While this value is smaller than some reported values of 1.5-2.0 mS/cm[36],[99],[100], it remains consistent with other studies that reported values as low as 0.5 mS/cm[9]. The difference may arise from variations in synthesis conditions, such as ball-milling speed and the temperature profile during annealing, as these are known to greatly affect the structure and properties of halide electrolytes[9]. For example, faster cooling rates reduce structural order and increase grain boundary resistance, which can lower ionic conductivity[102]. The ionic conductivity of LIZC was measured at 0.7 mS/cm (Figure A.8 and Table A.2)–two orders of magnitude larger than monoclinic LZC (0.008 mS/cm) and comparable to LIC.

Second, the LIC-VGCF composite prepared through ball milling at 400 rpm was used as a cathode in a half-cell configuration, and was cycled between 1.4 V and 3.6 V. Changes in crystalline structure were monitored using XRD, the results of which are presented in Figure 4.8.

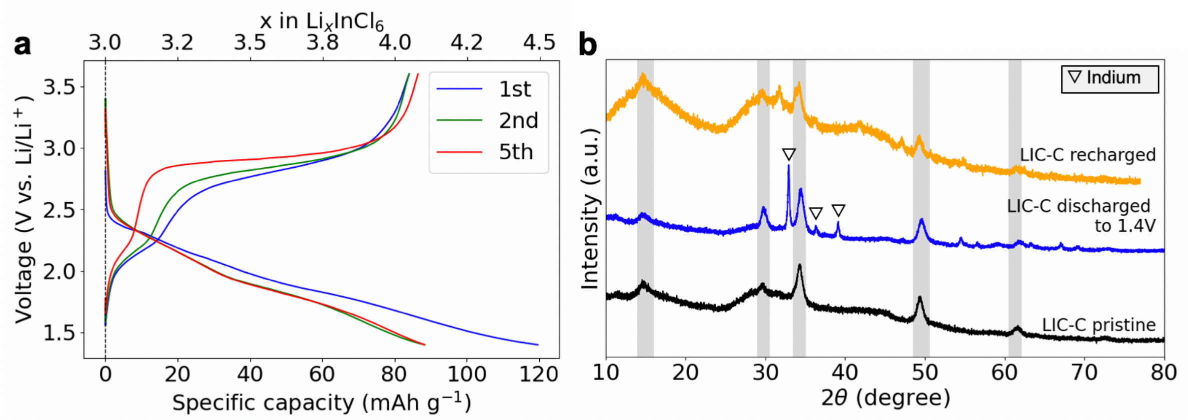

Figure 4.8: Galvanostatic cycling of LIC. a, The galvanostatic cycling data of annealed LIC-C ball-milled at 400 rpm. **b,** X-ray diffraction patterns of the pristine compound before cycling, after the first discharge to 1.4 V, and after the first recharge to 3.6 V.

The first observation to make from Figure 4.8a is that the reduction potential was measured at 2.5 V, which aligns well with previously reported values of 2.5 - 2.8 V[27],[101],[103]. When the half-cell is cycled down to 1.4 V, indium metal forms, as evidenced by the distinct indium metal peaks at $2\theta = 33.0°$, 36.3°, and 39.1° (Figure 4.8b). These peaks disappear upon recharging, suggesting that the process of indium metal formation is reversible. This is further supported by the voltage profile, which shows 93% capacity retention in the first cycle and full capacity retention in subsequent cycles–indicative of a reversible process. To evaluate the effect of Zr^{4+}-substitution in LIC, LIZC was cycled over two voltage ranges: 1.4 V - 3.6 V, consistent with the conditions used for LIC, and 0.6 V - 3.6 V, as used for LZC. Moreover, LIZC was discharged to various depths of discharge. The resulting galvanostatic profiles and the corresponding XRD patterns are presented in Figure 4.9.

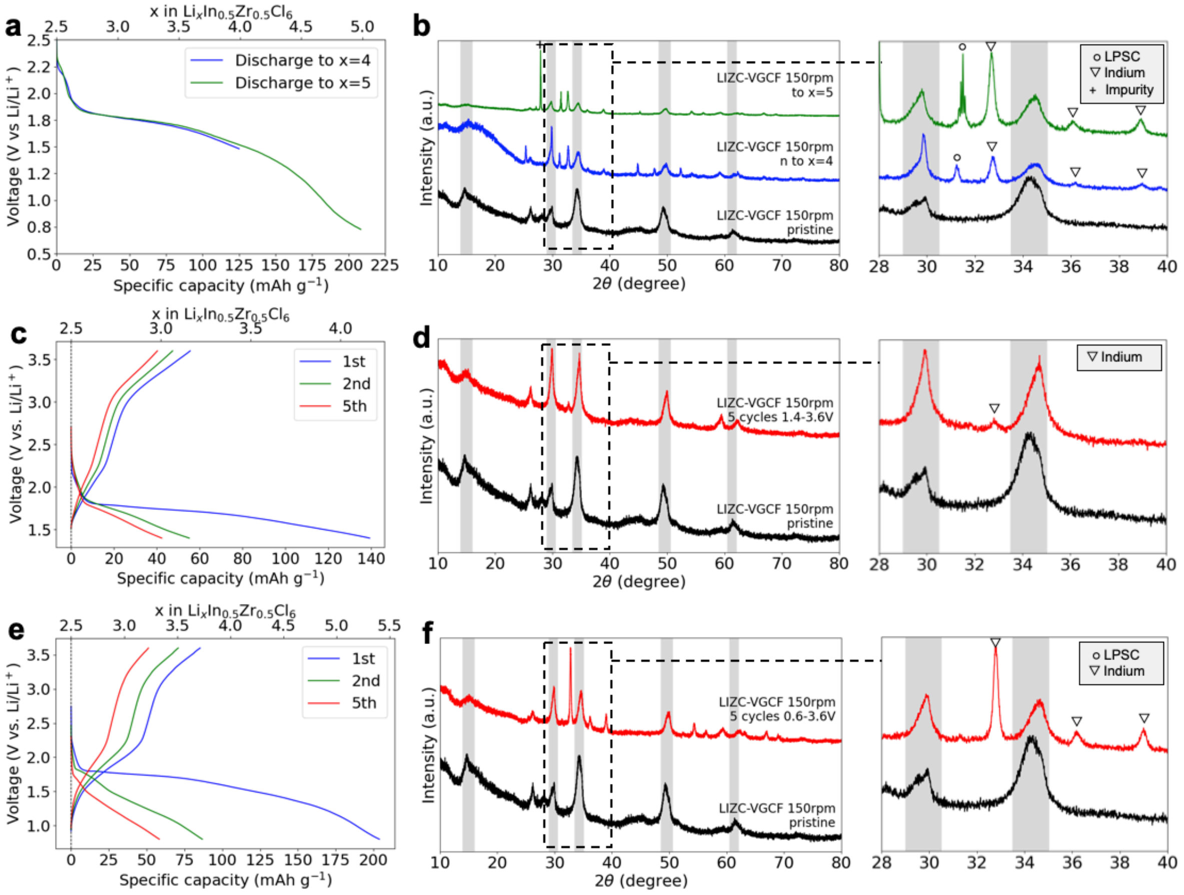

Figure 4.9: Galvanostatic profiles and corresponding X-ray diffraction patterns of LIZC. a,b, Galvanostatic discharge to x = 4 and x = 5 with the X-ray diffraction pattern at both depths of discharge. **c,d,** Galvanostatic cycling over 1.4 V - 3.6 V with the XRD pattern of the pristine sample and recharged sample. **e,f,** Galvanostatic cycling over 0.6 V - 3.6 V with the XRD pattern of the pristine sample and recharged sample.

First, Figure 4.9a shows an onset reduction voltage of 2.3 V–very close to that of LIC (2.5 V) and significantly larger than that of LZC (1.7 V). This observation is consistent with the findings of Wu *et al.* [20], who reported that in halide solid-state electrolytes, the reduction potential is typically governed by the more electronegative cation.

Further, as with LIC, indium metal formation upon discharge to both x = 4 (1.5 V) and x = 5 (0.7 V) is confirmed by diffraction peaks at $2\theta = 33.1°, 36.3°, 39.0°$ and $54.4°$, as seen in Figure 4.9b. Similarly to LIC, these indium metal peaks disappear upon recharging after cycling down to 1.4 V, as shown in Figure 4.9c,d, suggesting reversible indium deposition.

However, in contrast to LIC, LIZC suffers from a 60% capacity loss during the first cycle, followed by a gradual ongoing capacity loss in subsequent cycles. The underlying cause of this capacity loss remains unclear. One potential clue lies in the increased intensity of the peak at 59°–a minor reflection in the characteristic monoclinic spectrum–which increases in intensity upon discharge and remains present upon recharge (Figure 4.9b,d). In the LiCl diffraction pattern, this 59° peak appears with a higher relative intensity than in the monoclinic spectrum. This suggests the possibility of irreversible LiCl formation. Yet, under dry and inert conditions, LiCl formation is typically accompanied by the formation of indium metal. The absence of indium metal peaks in the recharged sample complicates this interpretation, and raises the hypothesis that, upon recharging, indium may not recrystallise to its original monoclinic structure form but instead forms an amorphous state that cannot be detected by means of XRD.

Further, extending the cycling window to 0.6 V - 3.6 V resulted in the loss of reversible behaviour, as evidenced by the persistence of indium metal peaks in the post-cycling XRD (Figure 4.9e,f). Deep discharge thus facilitates the decomposition of LIZC to an extent that its original structure cannot be recovered upon recharging.

4.2.3. Exploring low-voltage behaviour of LIZC through computational methods

DFT and AIMD simulations were utilised as atomistic tools to gain deeper insight into the low-voltage behaviour of LIZC during lithiation. For this purpose, a 2 × 1 × 2 supercell was constructed, with Zr^{4+} and In^{3+} each filling half of the metal cation positions–of which one *4g* position–in line with the reported structure of LIZC[9]. Figure 4.10 presents the convex hull, the corresponding voltage profile, and the results of AIMD simulations conducted at 400 K over a 100 ps period.

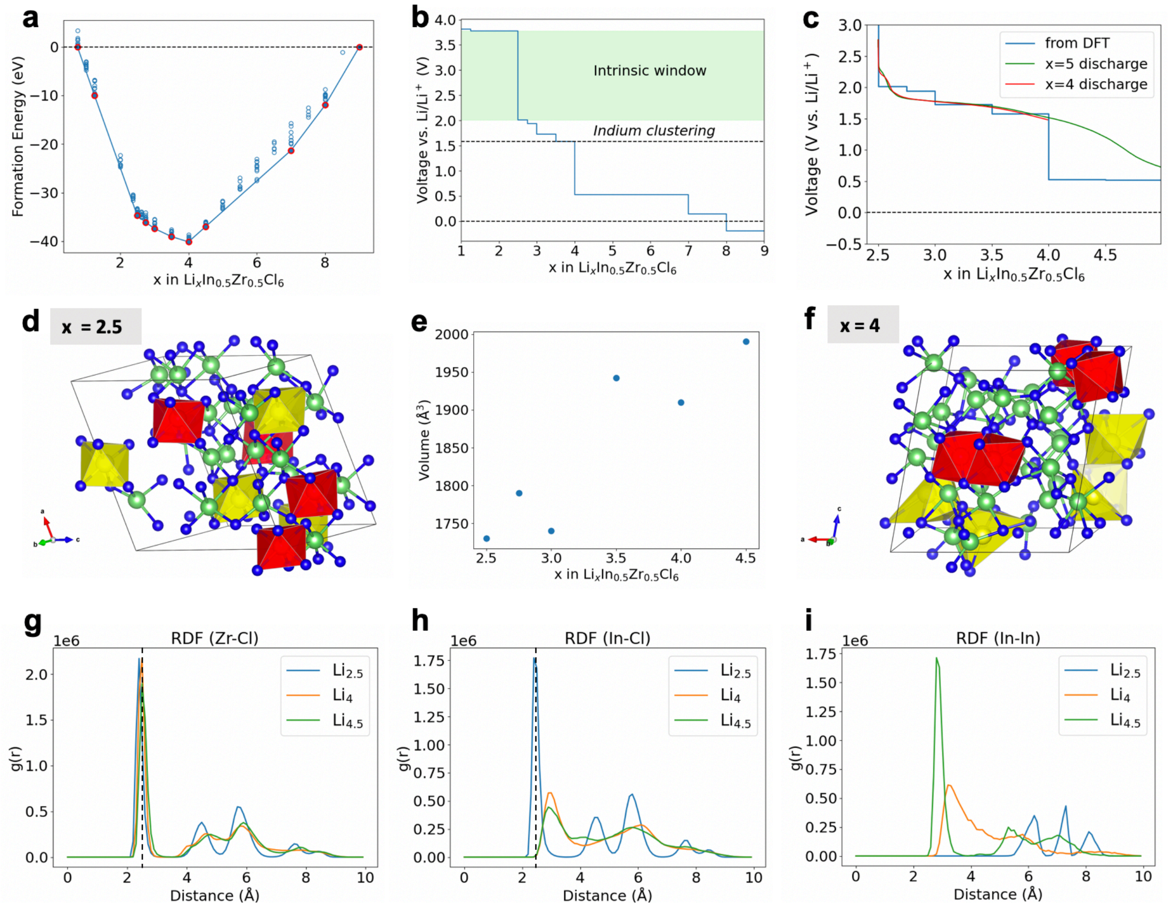

Figure 4.10: Stability window of LIZC as defined by DFT and MD calculations. a, Formation energies of $Li_xIn_{0.5}Zr_{0.5}Cl_6$ with respect to the completely delithiated and lithiated states. The convex line follows the lowest energy path–indicating the stable configurations along the range. **b,** Corresponding voltage profile indicating the intrinsic window and the voltage of 1.6 V where indium clustering is observed. **c,** The calculated voltage profile compared to the experimentally obtained discharge curves. **d,f,** Configurations after a 100 ps AIMD simulation at 400 K of the **(d)** unlithiated $Li_{2.5}In_{0.5}Zr_{0.5}Cl_6$ phase and **(e)** $Li_4In_{0.5}Zr_{0.5}Cl_6$ compound where decomposition in the form of indium clustering is observed. Zirconium is shown in red, indium in yellow, chlorine in blue and lithium in green. **e,** Evolution of the volume of stable structures on the convex hull, which shows a rapid increase in volume beyond x = 3. **g-i** Radial distribution frequency plots of 100 ps AIMD simulations at 400 K, comparing **(g)** Zr-Cl, **(h)** In-Cl, and **(i)** In-In distances.

DFT calculations presented in Figure 4.10a-c predict the intrinsic reduction limit of LIZC at 2.0 V–only slightly lower than the value of 2.3 V that is experimentally observed. Moreover, AIMD simulations reveal that structural breakdown is expected between lithium concentrations of x = 2.5 and x = 4, corresponding to a voltage range of 2.0 - 1.6 V (Figure 4.10d,f). This is further supported by the analysis of volumetric changes in the stable relaxed structures, which show a rapid volumetric expansion at x = 3.5, associated with a voltage of 1.7 V, that may indicate structural instability (Figure 4.10e). RDF analysis further shows that while zirconium cations maintain their octahedral coordination upon reduction–indicated by the retention of the peak at 2.3 Å in the Zr-Cl RDF plot–indium octahedra break and start to cluster, evidenced by the lengthening of the average In-Cl bond at 2.3 Å and a shift of the In-In distance to lower values (Figure 4.10g-i). This aligns closely with experimental observations, where indium metal is detected upon discharge beyond a lithium concentration of x = 4.

As a final computational investigation, the density of electronic states (DOS) was calculated for both LIZC and LIC at various stable lithiation levels, to identify any electronic states that may be involved in the decomposition process during lithiation. The complete results are presented in Figure A.4 and Figure A.5, for LIC and LIZC, respectively.

In the case of LIC, indium s-orbitals introduce deep electronic trap states within the bandgap immediately upon lithiation, indicating electron localisation on indium atoms[104]. As the lithium content is increased, both the number and the energy range of these trap states expands, including in the structure with x = 4.25, i.e. the lithiation level where reversible decomposition is observed experimentally. The trap states lie below the Fermi energy level and can therefore be assumed to be almost fully occupied[104]. An increase in indium s-states below the Fermi energy thus reflects the increased absorption of electrons into indium s-orbitals, indicating initiation of reduction.

In LIZC, indium s-orbitals also form deep electronic trap states within the bandgap right upon lithiation. As in LIC, these states exhibit widening both in energy range and number of states at higher levels of lithiation, while remaining below the Fermi energy–again indicating electron localisation and the onset of lithium reduction. However, zirconium d-orbitals are also starting to become more available for electrons upon lithiation. Initially, at x = 3, only a small number of states appears below the Fermi energy (at x = 3), but upon lithiation to x = 4 and beyond, zirconium provides a continuous band of available states around the Fermi energy. Unlike the localised indium trap states, this behaviour is indicative of (semi)-metallic behaviour, where electronic conduction is enabled[104]. This density of states analysis suggests that indium contributes localised energy states associated with its reduction and the structural breakdown of its octahedra, whereas zirconium supports electron transport while retaining its octahedral coordination over a wider lithiation range.

Overall, these results demonstrate that LIZC undergoes the same decomposition as LIC upon cycling beyond 1.4 V. Consequently, it does not offer improved anodic stability over LIC, with its experimentally determined intrinsic reduction potential of 2.3 V being only marginally lower than that of LIC (2.5 V). Importantly, DOS analysis suggests that zirconium adds electronic states that enable the delocalised absorption of electrons into the conduction band, which increases electronic conductivity but prevents breakdown. In contrast, indium adds localised trap states within the bandgap that initiate its reduction and induce structural collapse.

4.3. High-entropy zirconium(IV)-based halide electrolytes

This section examines the low-voltage behaviour of the Zr-based high-entropy compounds H5 ($Li_{2.8}MCl_6$, with M = In, Lu, Sc, Yb, Zr in equimolar ratio) and H4, which features the same set of metal cations, but excludes In^{3+}. The analysis begins with computational predictions, followed by the synthesis of both compounds and an experimental evaluation of their stability at low voltages.

4.3.1. Low-voltage behaviour in high-entropy electrolytes: a computational exploration

This section first presents some computational results for the H5 compound, obtained within the research group. It is important to highlight that the 2 × 1 × 2 monoclinic supercell contains eight cationic positions, making it impossible to include each of the five cations (In^{3+}, Lu^{3+}, Sc^{3+}, Yb^{3+} and Zr^{4+}) in an equimolar ratio. Consequently, each H5 supercell contains two cations at lower concentrations. This results in a general composition of $Li_aM1_{0.25}M2_{0.25}M3_{0.25}M4_{0.125}M5_{0.125}Cl_6$ where a = 2.75 if Zr^{4+} is one of M1, M2, or M3, and a = 2.875 if Zr^{4+} is among the less concentrated species M4 or M5. To evaluate how the cationic ratio affects the stability window, the formation energies and the corresponding voltage profiles upon partial (de)lithiation for various cationic ratios are presented in Figure 4.11.

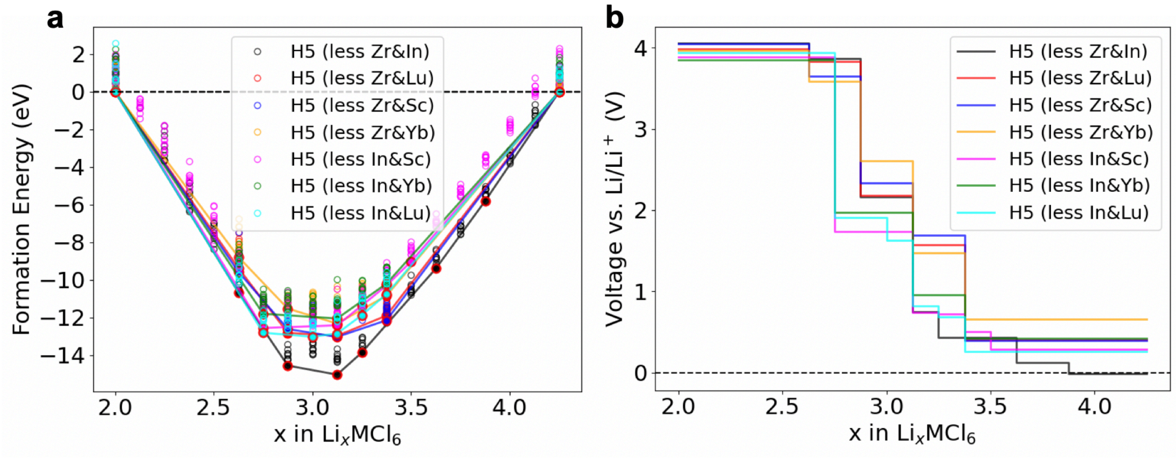

Figure 4.11: Formation energies and corresponding voltages during partial (de)lithiation for various metal cation ratios in H5. Each line corresponds to a supercell in which two metal cations are present in a reduced concentration of 0.125 instead of 0.25. **a,** Formation energies of the different H5 structures, referenced against their energies at x = 2 and x = 4.25. The convex lines follow the lowest formation energy paths, indicating stable phases upon lithiation. **b,** Voltage profiles corresponding to transitions between stable phases on the convex hull.

Two key observations can be drawn from Figure 4.11. First, the intrinsic reduction potential highly depends on the specific cation ratio used and varies between 1.7 and 2.7 V for the screened compositions. This suggests that the reduction stability is highly affected by the intrinsic properties of the cations, rather than arising primarily from entropic stabilisation of the crystal, as proposed in previous work[37],[38]. In contrast, the oxidation potential remains relatively consistent across the different structures, falling in the narrower range of 3.6 to 3.9 V. This supports previous findings that the oxidation potential in halide SEs primarily depends on the electronegativity of the halogen anion[7].

Second, the compounds containing less In^{3+} exhibit the best reduction stability. This aligns with previous findings that the reduction potential in halide SEs primarily depends on the electronegativity of the central metal cation: a lower electronegativity tends to shift the reduction potential of the electrolyte to higher voltages[20]. Among the five metals considered, indium has in fact the highest electronegativity of 1.78, compared to scandium (1.36), zirconium (1.33) and lutetium (1.27)[105].

To this end, indium was completely excluded from the structure, yielding the H4 compound. A useful consequence of this omission is that the 2 × 1 × 2 supercell can now achieve an equimolar distribution of the remaining cations (Lu^{3+}, Sc^{3+}, Yb^{3+} and Zr^{4+}). Therefore, a full convex hull was constructed for H4 and its corresponding voltage profile was calculated, the results of which are presented in Figure 4.12.

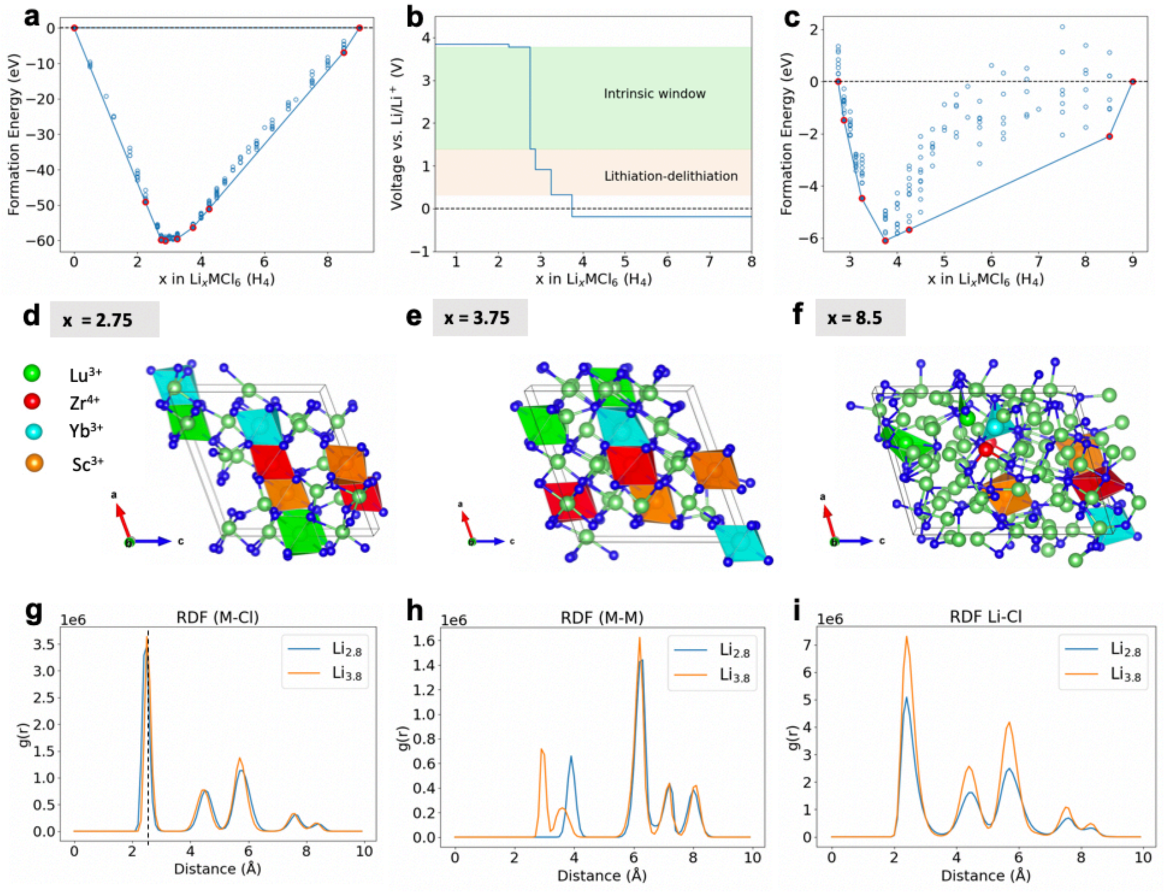

Figure 4.12: Stability window of H4 as defined by DFT and MD calculations. a, Formation energies of $\mathrm{Li}_x\mathrm{MCl}_6$ with respect to the completely delithiated and lithiated states. The convex line follows the lowest energy path–indicating the stable configurations along the range. **b,** Corresponding voltage profile indicating the intrinsic window and lithiation/delithiation region, where lithium insertion is possible without destroying the monoclinic structure. **c,** The reduction part of the convex hull, where $\mathrm{Li}_{2.75}\mathrm{MCl}_6$ and $\mathrm{Li}_9\mathrm{MCl}_6$ are taken as references. **d,e,** Configurations after a 100 ps AIMD simulation at 400 K of the **(d)** unlithiated $\mathrm{Li}_{2.75}\mathrm{MCl}_6$ compound and the **(e)** $\mathrm{Li}_{3.75}\mathrm{MCl}_6$ compound in the lithiation/delithiation region. **f** Configuration of $\mathrm{Li}_{8.5}\mathrm{ZrCl}_6$ after DFT, showing structural decomposition. **g-i** Radial distribution frequency plots from 100 ps AIMD simulations at 400 K comparing **(g)** M-Cl, **(h)** M-M, and **(i),** Li-Cl distances with M = Lu, Sc, Yb, Zr.

The DFT calculations presented in Figure 4.12a-c predict the intrinsic stability window of H4 to reach down to 1.4 V. Therefore, the complete removal of In^{3+} from the structure further improves the theoretical intrinsic reduction stability compared to the H5 compositions studied, which exhibit lower stability limits ranging from 1.7 to 2.7 V (Figure 4.11). Furthermore, a molecular dynamics simulation at 400 K of $\mathrm{Li}_{3.75}\mathrm{MCl}_6$–formed at the voltage plateau at 0.3 V–revealed no signs of structural degradation over a simulation period of 100 ps, suggesting that H4 may remain stable down to 0.3 V (Figure 4.12d,e). This structural stability is further supported by the radial distribution frequency plots shown in Figure 4.12g-i. For example, the M-Cl plot shows a persistent sharp peak at 2.3 Å for both the unlithiated structure and $\mathrm{Li}_{3.75}\mathrm{MCl}_6$, indicating strong and well-defined octahedral coordination between the Zr and Cl atoms is maintained upon lithiation. In contrast, the $\mathrm{Li}_{8.5}\mathrm{MCl}_6$ phase formed at a higher lithiation level–corresponding to a potential of -0.2 V–shows advanced structural breakdown, even prior to MD simulation (Figure 4.12f).

As with LZC, the impact of introducing the *4g* site–and the associated increase in configurational disorder–on the electrochemical behaviour of H4 was checked. To this end, the computational analysis was repeated using a configuration in which all metal cations were positioned at the *2a* sites. The resulting energy landscape, voltage profile and intrinsic stability window were found to be nearly identical to those of the original configuration that has one cation placed at the *4g* site (Figure A.6). Moreover, the voltage range over which lithiation/delithiation behaviour is expected remained unchanged. A plausible explanation for this insensitivity is that the presence of multiple different cations already introduces a high degree of disorder to the structure. As a result, the addition of an additional source of positional disorder–through occupation of an alternative Wyckoff site–has little effect on the overall structural disorder and thus on the electrochemical properties of the material.

4.3.2. Synthesis of the high-entropy compounds H4 and H5

The H4 and H5 compounds were synthesised according to the usual two-step method: high-speed ball milling followed by annealing. An annealing temperature of 260 °C for 12 hours was used, which is based on synthesis parameters used in literature for a similar high-entropy compound[38]. The XRD patterns in Figure 4.13 provide XRD patterns on H4 and H5 at various synthesis stages.

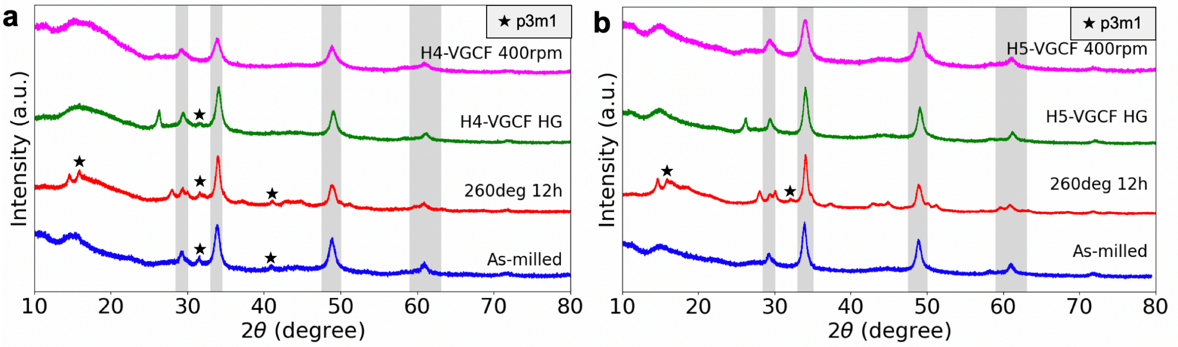

Figure 4.13: X-ray diffraction patterns of high-entropy compounds at different synthesis stages. a,b XRD patterns of **(a)** H4 and **(b)** H5 after ball milling, annealing, and after mixing with VGCF by means of hand-grinding (HG) and ball milling (400 rpm). The as-milled sample was used for mixing with VGCF. Peaks characteristic of the monoclinic structure show up in the shaded regions, possible P3m1 phases are indicated with stars.

For the H4 composition, ball milling yields a mixed-phase structure, consisting of a major monoclinic phase, as evidenced by characteristic monoclinic peaks in the shaded regions. In addition, a minor trigonal phase is present, with reflections at $2\theta = 31.5°$ and $40.9°$. Although subsequent annealing may slightly improve crystallinity, the minor trigonal phase remains present, and some other peaks appear, which could originate from impurities or the formation of a different minor phase.

In contrast, the H5 compound exhibits a single-phase monoclinic structure with characteristic monoclinic reflection peaks directly after ball milling. This may be attributed to the smaller cationic radius of indium, that drives the expected phase to the monoclinic form[7]. However, as with H4, annealing introduces additional reflections, of which the reflections at $2\theta = 15.9°$ and $31.5°$ might be attributed to a partly trigonal phase. The other peaks, for example those appearing in the 43° to 47° region, might again be caused by impurities or the conversion into a different minor phase.

Given these observations, the as-milled samples were selected for further study in both cases. Subsequent processing of the as-milled samples with VGCF–either by hand grinding or high-speed ball milling–preserved the monoclinic phase for both high-entropy compounds. The only notable difference was the sharp carbon peak at $2\theta = 26.2°$ observed in the XRD pattern of the hand-ground samples, which was significantly reduced in intensity in the ball-milled counterpart. This reduction may be attributed to ball milling that reduces the long-range order of the VGCF particles, for example by shortening the length of the VGCF rods, thereby reducing peak intensity[106].

4.3.3. Experimental low-voltage performance of H4 and H5

The ionic conductivities of the high-entropy compounds were first evaluated by means of PEIS. Both as-milled compounds exhibit respectable values of 0.2 mS/cm (Figure A.8 and Table A.2)–just exceeding the commonly accepted threshold of 10^{-4} S/cm for viable solid electrolytes[12]. However, these conductivity values are approximately one order of magnitude lower than those reported in previous work for the annealed H5 compound[7]. This difference may be attributed to the annealing process, as annealed compounds are frequently reported to show improved ionic conductivity compared to their ball-milled counterparts, due to their higher degree of crystallinity[18]. The more crystalline compounds generally have less defects that can form barriers to Li^+-diffusion and have larger grain sizes, which reduces grain boundary resistance[107]. Indeed, the annealed H4 sample synthesised in this work shows a higher ionic conductivity of 0.9 mS/cm compared to the as-milled sample (Figure A.8 and Table A.2). Electronic conductivities, determined using DC polarisation (Figure A.7 and Table A.1), were found to be 2×10^{-10} S/cm for H4 and 4×10^{-10} S/cm for H5–both sufficiently low to mitigate the risk of self-discharge[13].

Having established that both high-entropy compounds show acceptable ionic and electronic conductivity values, their low-voltage stability is assessed. To this end, half-cells that use the Li_xMCl_6-VGCF mixture as a cathode are cycled and XRD measurements are taken of the pristine, discharged and recharged sample to monitor any crystallographic changes. The discharge profiles and corresponding XRD patterns for H4 and H5 are presented in Figure 4.14.

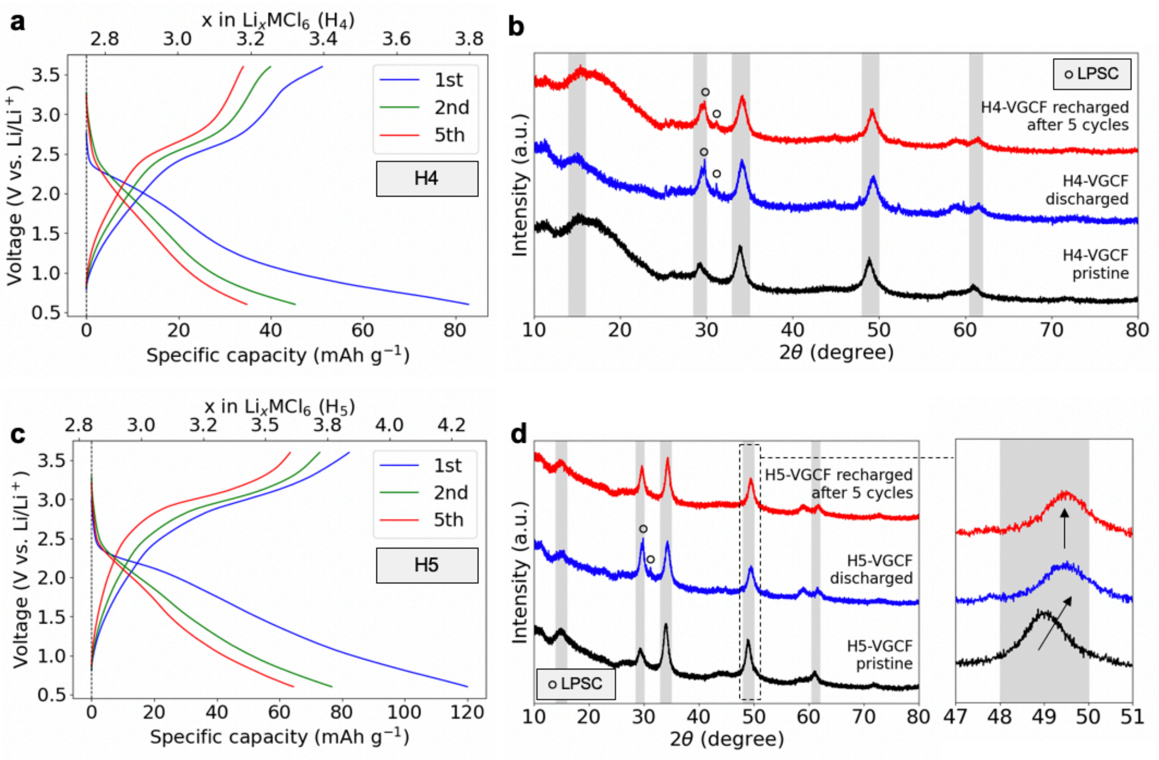

Figure 4.14: Galvanostatic cycling behaviour of high-entropy compounds. The compounds were ball milled with VGCF at 400 rpm. Half-cells were cycled at a current of 200 μA = 255 μA/cm^2 = 6.7 mA/g. **a,c** Voltage profiles during galvanostatic cycling between 0.6 and 3.6 V for the **(a)** H4 and **(c)** H5 compound, showing the first, second and fifth cycles. **b,d** X-ray diffraction patterns of the pristine sample, sample discharged to 0.6 V after the first cycle, and the recharged sample after 5 cycles for the **(b)** H4 and **(d)** H5 compound, showing a peak shift to higher 2θ values upon discharge.

The first observation to make from Figure 4.14a,c is that both high-entropy compounds exhibit an initial onset potential around 2.6 V–significantly larger than the computationally predicted intrinsic reduction values of 1.4 V for H4 and an average of 2.2 V for the various H5 configurations (Figure 4.12 and Figure 4.11). This indicates that, in practice, both compounds are more readily reduced than the DFT calculations predict. Moreover, although computational predictions suggested that removing indium would significantly enhance the intrinsic reduction stability, experimental results reveal little difference between the H4 and H5 compounds in this respect.

Furthermore, both high-entropy compounds can accommodate more lithium than predicted when cycled down to 0.6 V, corresponding to 1.0 and 1.4 moles of lithium/electrons per mole H4 and H5 during the first cycle, respectively. Both values are significantly higher than what is expected from the predicted voltage profile obtained from DFT in Figure 4.12. However, capacity quickly decays upon subsequent cycling. The H4 compound loses 58% of its initial capacity over five cycles, with 46% lost during the first cycle, and the H5 compound shows a 46% capacity loss over five cycles, of which 38% during the first cycle (Figure 4.14a,c). The combination of excessive lithiation and irreversible capacity loss could both indicate decomposition behaviour during cycling.

Despite these possible indicators of decomposition, the XRD patterns of both the discharged and recharged compounds retain the characteristic monoclinic reflections–observable in the shaded regions–which are almost identical to the pristine materials (Figure 4.14). Crucially, no additional reflections appear that can be attributed to crystalline metallic forms of any of the cations in the structure (M^0).

However, one clear structural change that can be observed in the XRD spectra of both compounds is the shift of the peak at $2 = 49°$ to higher angles, indicative of lattice contraction (Figure 4.14c,d). This contraction was also reported in previous work by Cheng *et al.* [33] and may arise from the stronger Coulombic attraction between Li^+ and the anionic Cl^- framework, leading to a reduction in the interlayer distance[7]. Le Bail refinement of the H5 compound confirmed this lattice contraction and also revealed that the lattice in fact did not recover its original volume after recharging (Figure A.9). This irreversible contraction suggests that even if lithium is inserted into the monoclinic structure, it is not completely extracted, aligning with the irreversible behaviour observed in the voltage profiles in Figure 4.14a,c.

This presents a complex situation in which the voltage profiles and irreversible contraction of the lattice evidenced in the XRD pattern point toward possible irreversible decomposition, yet no evidence in the form of decomposition products is found. One possible explanation is the presence of transport limitations of electrons and/or Li^+, which is affected by the interface area between the electronically conductive VGCF and the ionically conductive Li_xMCl_6. To test the effect of reducing the interface area between VGCF and the high entropy materials, hand-ground composites were also subjected to cycling. The results provided in Figure A.10 indicate that these samples exhibit virtually no reversible capacity when cycled over the same voltage window, with the XRD patterns indicating no structural changes. This result indeed suggests that poor interfacial contact may kinetically hinder lithium transport, thereby preventing effective and reversible lithiation/delithiation behaviour.

To further assess the role of transport limitations, the H5 sample was also cycled at a significantly lower discharge current of 20 μA. In addition, the cut-off voltage was lowered to 3.0 V to ensure oxidation of the electrolyte is prevented. The results are presented in Figure 4.15.

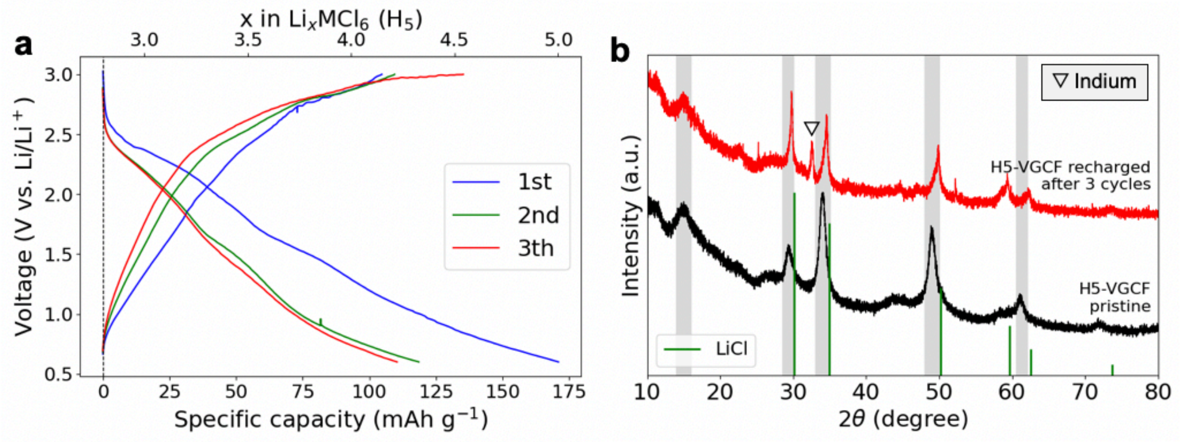

Figure 4.15: Galvanostatic cycling behaviour of H5 at 20 μA. Slow cycling corresponded to a current of 26 $\mu A/cm^2 = 1.3$ mA/g over a range of 0.6 to 3.0 V. **a,** Voltage profile during galvanostatic cycling showing the first, second and third cycle. **b,** X-ray diffraction patterns of the pristine sample and the recharged sample with a reference pattern of LiCl.

Figure 4.15a demonstrates that the ten-fold reduction in discharge current resulted in an increase in first-cycle capacity–from 120 mAh/g to 171 mAh/g–consistent with the hypothesis that transport limitations limit electrochemical behaviour of the cathode. In addition, the XRD pattern of the recharged sample now contains reflections corresponding to metallic indium, as well as LiCl (Figure 4.15b). Thus, the H5 compound does not undergo reversible lithiation and delithiation, but instead undergoes decomposition into LiCl and metallic indium. The lack of structural breakdown observed in Figure 4.14b and d may therefore not be caused by lithiation/delithiation behaviour but might instead arise from transport limitations that prevent bulk structural breakdown.

These results therefore demonstrate that incorporating zirconium into a high-entropy environment does not enhance reduction stability, as the compounds exhibit poor intrinsic reduction stabilities and lack clear evidence of a favourable reversible lithiation/delithiation region.

5

Conclusions

This work set out to engineer monoclinic zirconium(IV)-based halide solid electrolytes and study their low-potential behaviour. To this end, three key structures were investigated: (i) an isolated zirconium system (Li_2ZrCl_6), (ii) the aliovalently substituted compound $Li_{2.5}In_{0.5}Zr_{0.5}Cl_6$, and (iii) a multi-cation high-entropy compound $Li_{2.75}MCl_6$ (M = Sc, Lu, Yb, Zr). Each of these compounds was successfully synthesised and studied using a combination of computational and experimental methods.

A key distinction was made between (i) the intrinsic electrochemical stability window, where no redox activity occurs, and (ii) an extended lithiation/delithiation region, in which the structure is reduced without undergoing decomposition.

First, we found that monoclinic Li_2ZrCl_6 demonstrates a wide lithiation/delithiation region, where lithium can be reversibly stored down to at least 0.6 V vs. Li/Li^+ without its monoclinic structure breaking down. This behaviour–which was consistently observed both experimentally and computationally–contributes to lithium storage capacity that may enhance the energy density of the battery. Thermodynamic calculations further revealed that an increased configurational disorder causes redox activity to start at a higher voltage, but leaves the voltage window over which reversible lithiation/delithiation is predicted unaltered, thus maintaining the material's compatibility with low-voltage anodes.

In contrast, the aliovalently substituted compound $Li_{2.5}In_{0.5}Zr_{0.5}Cl_6$ did not exhibit improved intrinsic reduction stability with respect to its single-metal counterparts. More importantly, upon cycling down to 1.4 V vs. Li/Li^+ the compound undergoes the same metallic indium formation that was demonstrated in Li_3InCl_6. This decomposition behaviour was predicted computationally, and experiments provided an additional key insight that this metal formation appears to be partly reversible.

Third, computations predicted improved stability against reduction enabled by the integration of zirconium in a multi-cation environment–showing both good intrinsic reduction stability and a wide window of non-destructive lithiation/delithiation behaviour. However, the experimental results contradict these predictions, as the multi-cation compounds synthesised in this study exhibit poor intrinsic reduction potentials of 2.6 V vs. Li/Li^+. Although no crystalline decomposition products were detected upon discharge to lower potentials, the continued loss of capacity indicated a lack of a reversible lithiation/delithiation mechanism. Slow discharge further revealed an eventual breakdown in the indium-containing high-entropy compound $Li_{2.8}MCl_6$ (M = In, Sc, Lu, Yb, Zr), indicating that neither the intrinsic properties of zirconium nor entropic effects can effectively stabilise the compound to suppress degradation at low potentials.

This study addressed the thermodynamic aspects of electrochemical stability, revealing how specific structural and compositional features govern the behaviour of zirconium-based halide electrolytes under low-potential conditions. Notably, it revealed the ability of monoclinic Li_2ZrCl_6 to support reversible lithiation without structural degradation–an uncommon and valuable trait that enhances compatibility with low-voltage anodes. We suspect that zirconium's tetravalent oxidation state plays a key role in enabling this valuable trait, as it may accommodate excess electrons during lithiation without disrupting its octahedral coordination. However, the inability to replicate this behaviour in aliovalent or multi-cation systems, despite favourable computational predictions, highlights a critical gap in our understanding of complex chemistries and the limitations of current modelling approaches. These findings underscore the need to complement thermodynamic insights with a deeper exploration of kinetic effects, which clearly influence the onset and reversibility of degradation. Furthermore, degradation product characterisation in this study was limited to crystalline phases, leaving the role of amorphous or metastable species unresolved. Addressing these limitations is essential for translating fundamental stability trends into practical design rules for next-generation solid electrolytes.

5.1. Directions for future research

Future studies may therefore explore the kinetic effects and include the identification of amorphous or metastable species, which aids our understanding of the mechanisms governing low-potential behaviour. Techniques such as nuclear magnetic resonance (NMR), X-ray photolectron spectroscopy (XPS), and scanning electron microscopy (SEM) could provide insight into amorphous degradation products, local chemical environments, oxidation states, and morphologies. Such insights are essential to uncover the mechanistic pathways driving low-voltage behaviour and will aid the design of halide solid electrolytes with improved reduction stability, enabling integration with high-capacity anodes in safer, energy-dense solid-state batteries.

References

[1] Intergovernmental Panel on Climate Change, *Climate Change 2021: The Physical Science Basis. Contribution of Working Group I to the Sixth Assessment Report of the Intergovernmental Panel on Climate Change*. 2021. [Online]. Available: `https://www.ipcc.ch/report/ar6/wg1/`.

[2] W. J. Ripple, C. Wolf, T. M. Newsome, P. Barnard, and W. R. Moomaw, "World scientists warning of a climate emergency," *BioScience*, vol. 70, no. 1, pp. 8–12, 2019. DOI: `10.1093/biosci/biz088`. [Online]. Available: `https://academic.oup.com/bioscience/article/70/1/8/5610806`.

[3] International Energy Agency, *World Energy Outlook 2024*. 2024. [Online]. Available: `https://www.iea.org/reports/world-energy-outlook-2024`.

[4] International Energy Agency, *Batteries and Secure Energy Transitions*. 2024. [Online]. Available: `https://www.iea.org/reports/batteries-and-secure-energy-transitions`.

[5] M. Li, J. Lu, Z. Chen, and K. Amine, "30 years of lithium-ion batteries," *Advanced Materials*, vol. 30, no. 33, p. 1 800 561, 2018.

[6] H. Kwak *et al.*, "Emerging halide superionic conductors for all-solid-state batteries: Design, synthesis, and practical applications," *ACS Energy Letters*, vol. 7, no. 5, pp. 1776–1805, 2022. DOI: `https://doi.org/10.1021/acsenergylett.2c00438`. [Online]. Available: `https:https://pubs.acs.org/doi/full/10.1021/acsenergylett.2c00438`.

[7] Q. Wang *et al.*, "Designing lithium halide solid electrolytes," *Nature Communications*, vol. 15, no. 1, p. 1050, 2024. DOI: `10.1038/s41467-024-45258-3`. [Online]. Available: `https://www.nature.com/articles/s41467-024-45258-3`.

[8] K. Tuo, C. Sun, S. Liu, and S. Liu, "Recent progress in and perspectives on emerging halide superionic conductors for all-solid-state batteries," *Electrochemical Energy Reviews*, vol. 6, no. 1, p. 17, 2023. DOI: `https://doi.org/10.1007/s41918-023-00179-5`. [Online]. Available: `https://link.springer.com/article/10.1007/s41918-023-00179-5`.

[9] B. Helm *et al.*, "Exploring aliovalent substitutions in the lithium halide superionic conductor liinzrcl (0 x 0.5)," *Chemistry of Materials*, vol. 33, no. 11, pp. 4028–4038, 2021. DOI: `10.1021/acs.chemmater.1c01348`. [Online]. Available: `https://pubs.acs.org/doi/10.1021/acs.chemmater.1c01348`.

[10] E. van der Maas *et al.*, "Re-investigating the structure–property relationship of the solid electrolytes li 3- x in 1- x zr x cl 6 and the impact of in–zr (iv) substitution," *Journal of Materials Chemistry A*, vol. 11, no. 9, pp. 4559–4571, 2023.

[11] S. Salvage, *Jaaroverzicht 2023*, 2023. [Online]. Available: `https://stichtingsalvage.nl/wp-content/uploads/2024/01/Stichting-Salvage-Jaaroverzicht-2023.pdf`.

[12] J. Liu, T. Wang, J. Yu, S. Li, H. Ma, and X. Liu, "Review of the developments and difficulties in inorganic solid-state electrolytes," *Materials*, vol. 16, no. 6, p. 2510, 2023.

[13] P. Nzereogu *et al.*, "Solid-state lithium-ion battery electrolytes: Revolutionizing energy density and safety," *Hybrid Advances*, p. 100 339, 2024.

[14] S. Ai, X. Wu, J. Wang, X. Li, X. Hao, and Y. Meng, "Research progress on solid-state electrolytes in solid-state lithium batteries: Classification, ionic conductive mechanism, interfacial challenges," *Nanomaterials*, vol. 14, no. 22, p. 1773, 2024.

[15] A. Machín, C. Morant, and F. Márquez, "Advancements and challenges in solid-state battery technology: An in-depth review of solid electrolytes and anode innovations," *Batteries*, vol. 10, no. 1, p. 29, 2024.

[16] T. Asano, A. Sakai, S. Ouchi, M. Sakaida, A. Miyazaki, and S. Hasegawa, “Solid halide electrolytes with high lithium-ion conductivity for application in 4 v class bulk-type all-solid-state batteries,” *Advanced Materials*, vol. 30, no. 44, p. 1 803 075, 2018.

[17] C. Wang, J. Liang, J. T. Kim, and X. Sun, “Prospects of halide-based all-solid-state batteries: From material design to practical application,” *Science Advances*, vol. 8, no. 36, eadc9516, 2022. DOI: `10.1126/sciadv.adc9516`. [Online]. Available: `https://www.science.org/doi/10.1126/sciadv.adc9516`.

[18] B. Tao, D. Zhong, H. Li, G. Wang, and H. Chang, “Halide solid-state electrolytes for all-solid-state batteries: Structural design, synthesis, environmental stability, interface optimization and challenges,” *Chemical Science*, vol. 14, no. 33, pp. 8693–8722, 2023. DOI: `10.1039/D3SC02093B`. [Online]. Available: `https://pubs.rsc.org/en/content/articlehtml/2023/sc/d3sc02093b`.

[19] S. Wang *et al.*, “Lithium chlorides and bromides as promising solid-state chemistries for fast ion conductors with good electrochemical stability,” *Angewandte Chemie International Edition*, vol. 58, no. 24, pp. 8039–8043, 2019. DOI: `10.1002/anie.201901938`. [Online]. Available: `https://onlinelibrary.wiley.com/doi/full/10.1002/anie.201901938`.

[20] J. Wu, Li, Jiahao, X. Yao, and X. Yao, “Exploring the potential of halide electrolytes for next-generation all-solid-state lithium batteries,” *Advanced Functional Materials*, p. 2 416 671, 2024.

[21] N. Enaki *et al.*, “Composite metamaterials for biological decontamination of fluids,” in *4th International Conference on Nanotechnologies and Biomedical Engineering: Proceedings of ICNBME-2019, September 18-21, 2019, Chisinau, Moldova*, Springer, 2020, pp. 373–377.

[22] K. Wang *et al.*, “A cost-effective and humidity-tolerant chloride solid electrolyte for lithium batteries,” *Nature Communications*, vol. 12, no. 1, pp. 1–11, 2021. DOI: `10.1038/s41467-021-24697-2`. [Online]. Available: `https://www.nature.com/articles/s41467-021-24697-2`.

[23] X. Liu, F. Mi, and C. Sun, “A cost-effective ca-doped li 2 zrcl 6 halide solid electrolyte for all-solid-state lithium batteries,” *Chemical Communications*, 2025.

[24] Z. Yao *et al.*, “High ionic conductivity in li2zrcl6 via la3+ doping for all-solid-state lithium metal batteries,” *Journal of Electronic Materials*, pp. 1–8, 2024.

[25] H. Kwak *et al.*, “Li+ conduction in aliovalent-substituted monoclinic li2zrcl6 for all-solid-state batteries: Li2+ xzr1-xmxcl6 (m= in, sc),” *Chemical Engineering Journal*, vol. 437, p. 135 413, 2022.

[26] S. Y. Kim *et al.*, “Lithium ytterbium-based halide solid electrolytes for high voltage all-solid-state batteries,” *ACS Materials Letters*, vol. 3, no. 7, pp. 930–938, 2021.

[27] D. Park *et al.*, “Theoretical design of lithium chloride superionic conductors for all-solid-state high-voltage lithium-ion batteries,” *ACS applied materials & interfaces*, vol. 12, no. 31, pp. 34 806–34 814, 2020.

[28] Y. Liu, S. Wang, A. M. Nolan, C. Ling, and Y. Mo, “Tailoring the cation lattice for chloride lithium-ion conductors,” *Advanced Energy Materials*, vol. 10, no. 40, p. 2 002 356, 2020.

[29] W. Li *et al.*, “High-voltage superionic and humidity-tolerant li2. 5sc0. 5zr0. 5cl6 conductor for lithium batteries via preferred orientation,” *Chemical Engineering Journal*, vol. 455, p. 140 509, 2023.

[30] P. Ganesan *et al.*, “Fluorine-substituted halide solid electrolytes with enhanced stability toward the lithium metal,” *ACS Applied Materials & Interfaces*, vol. 15, no. 32, pp. 38 391–38 402, 2023.

[31] Q. Shao *et al.*, “New insights into the effects of zr substitution and carbon additive on li3–x er1–x zr x cl6 halide solid electrolytes,” *ACS Applied Materials & Interfaces*, vol. 14, no. 6, pp. 8095–8105, 2022.

[32] B. T. Tham, M.-S. Park, J. H. Kim, and J. Moon, “Computational design of a mixed a-site cation halide solid electrolyte for all-solid-state lithium batteries,” *Journal of Materials Chemistry A*, vol. 11, no. 29, pp. 15 968–15 978, 2023.

[33] Z. Cheng *et al.*, “Beneficial redox activity of halide solid electrolytes empowering high-performance anodes in all-solid-state batteries,” 2024. DOI: `10.26434/chemrxiv-2024-x2rld`. [Online]. Available: `https://chemrxiv.org/engage/chemrxiv/article-details/65fa01d99138d23161d10108`.

[34] B. Ouyang and Y. Zeng, “The rise of high-entropy battery materials,” *nature communications*, vol. 15, no. 1, p. 973, 2024.

[35] K.-F. Ren *et al.*, “Working principles of high-entropy electrolytes in rechargeable batteries,” *ACS Energy Letters*, vol. 9, no. 6, pp. 2960–2980, 2024.

[36] D. Li *et al.*, “High configuration entropy promises electrochemical stability of chloride electrolytes for high-energy, long-life all-solid-state batteries,” *Angewandte Chemie*, e202419735, 2024. DOI: `10.1002/ange.202419735`. [Online]. Available: `https://onlinelibrary.wiley.com/doi/10.1002/ange.202419735`.

[37] Y. Zeng *et al.*, “High-entropy mechanism to boost ionic conductivity,” *Science*, vol. 378, no. 6626, pp. 1320–1324, 2022.

[38] Z. Song *et al.*, “Promoting high-voltage stability through local lattice distortion of halide solid electrolytes,” *Nature Communications*, vol. 15, no. 1, p. 1481, 2024. DOI: `10.1038/s41467-024-45864-1`. [Online]. Available: `https://www.nature.com/articles/s41467-024-45864-1`.

[39] P. Zapp, A. Schreiber, J. Marx, and W. Kuckshinrichs, “Environmental impacts of rare earth production,” *MRS bulletin*, vol. 47, no. 3, pp. 267–275, 2022.

[40] International Renewable Energy Agency, *Constructing a Ranking of Critical Materials for the Global Energy Transition.* 2024. [Online]. Available: `https://www.irena.org/Publications/2024/Oct/Constructing-a-ranking-of-critical-materials-for-the-global-energy-transition`.

[41] E. van der Maas, “Halide solid electrolytes: From structure to properties,” 2023.

[42] T. Binninger, A. Marcolongo, M. Mottet, V. Weber, and T. Laino, “Comparison of computational methods for the electrochemical stability window of solid-state electrolyte materials,” *Journal of Materials Chemistry A*, vol. 8, no. 3, pp. 10 869–10 877, 2020. DOI: `10.1039/C9TA09401F`. [Online]. Available: `https://xlink.rsc.org/?DOI=C9TA09401F`.

[43] P. Nzereogu, A. Omah, F. Ezema, E. Iwuoha, and A. Nwanya, “Anode materials for lithium-ion batteries: A review,” *Applied Surface Science Advances*, vol. 9, p. 100 233, 2022.

[44] J. Lu, Z. Chen, F. Pan, Y. Cui, and K. Amine, “High-performance anode materials for rechargeable lithium-ion batteries,” *Electrochemical Energy Reviews*, vol. 1, pp. 35–53, 2018.

[45] M. Khan *et al.*, “Sio2-based lithium-ion battery anode materials: A brief review,” *Journal of Electronic Materials*, vol. 51, no. 7, pp. 3379–3390, 2022.

[46] Z.-y. Feng *et al.*, “Review of silicon-based alloys for lithium-ion battery anodes,” *International Journal of Minerals, Metallurgy and Materials*, vol. 28, pp. 1549–1564, 2021.

[47] J. Asenbauer, T. Eisenmann, M. Kuenzel, A. Kazzazi, Z. Chen, and D. Bresser, “The success story of graphite as a lithium-ion anode material–fundamentals, remaining challenges, and recent developments including silicon (oxide) composites,” *Sustainable Energy & Fuels*, vol. 4, no. 11, pp. 5387–5416, 2020.

[48] Y. Zhu *et al.*, “Origin of outstanding stability in the lithium solid electrolyte materials: Insights from thermodynamic analyses based on first-principles calculations,” *ACS Applied Materials & Interfaces*, vol. 7, no. 42, pp. 23 685–23 693, 2015. DOI: `10.1021/acsami.5b07517`. [Online]. Available: `https://pubs.acs.org/doi/10.1021/acsami.5b07517`.

[49] Y. Wang, L. Ye, W. Fitzhugh, X. Chen, and X. Li, “Interface coating design for dynamic voltage stability of solid-state batteries,” *Advanced Energy Materials*, vol. 13, no. 41, p. 2 302 288, 2023.

[50] T. K. Schwietert, A. Vasileiadis, and M. Wagemaker, “First-principles prediction of the electrochemical stability and reaction mechanisms of solid-state electrolytes,” *JACS Au*, vol. 1, no. 9, pp. 1488–1496, 2021. DOI: `10.1021/jacsau.1c00228`. [Online]. Available: `https://pubs.acs.org/doi/10.1021/jacsau.1c00228`.

[51] T. K. Schwietert *et al.*, “Clarifying the relationship between redox activity and electrochemical stability in solid electrolytes,” *Nature Materials*, vol. 19, no. 4, pp. 428–435, 2020. DOI: `10.1038/s41563-019-0576-0`. [Online]. Available: `https://www.nature.com/articles/s41563-019-0576-0`.

[52] P. Lannelongue *et al.*, “Stable cycling of halide solid state electrolyte enabled by a dynamic layered solid electrolyte interphase between li metal and li3ycl4br2,” *Energy Storage Materials*, vol. 72, p. 103 733, 2024.

[53] S. Chen *et al.*, “Unraveling electrochemical stability and reversible redox of y-doped li2zrcl6 solid electrolytes,” *Energy Material Advances*, vol. 4, p. 0019, 2023.

[54] K. Wang, Z. Gu, Z. Xi, L. Hu, and C. Ma, “Li3ticl6 as ionic conductive and compressible positive electrode active material for all-solid-state lithium-based batteries,” *Nature Communications*, vol. 14, no. 1, p. 1396, 2023.

[55] K. Arbi, A. Kuhn, J. Sanz, and F. García-Alvarado, “Characterization of lithium insertion into nasicon-type li1+ xti2- xalx (po4) 3 and its electrochemical behavior,” *Journal of The Electrochemical Society*, vol. 157, no. 6, A654, 2010.

[56] A. Marko, T. Scheiber, B. Gadermaier, and H. M. R. Wilkening, “Interfacial lithiation of lithium aluminum titanium phosphate explored by 7li nmr,” *Communications Chemistry*, vol. 8, no. 1, p. 102, 2025.

[57] Y. Benabed, M. Rioux, S. Rousselot, G. Hautier, and M. Dollé, “Assessing the electrochemical stability window of nasicon-type solid electrolytes,” *Frontiers in Energy Research*, vol. 9, p. 682 008, 2021.

[58] D. H. Tan *et al.*, “Elucidating reversible electrochemical redox of li6ps5cl solid electrolyte,” *ACS Energy Letters*, vol. 4, no. 10, pp. 2418–2427, 2019.

[59] T. H. Wan and F. Ciucci, “Ab initio study of the defect chemistry and substitutional strategies for highly conductive li3yx6 (x= f, cl, br, and i) electrolyte for the application of solid-state batteries,” *ACS Applied Energy Materials*, vol. 4, no. 8, pp. 7930–7941, 2021.

[60] T. Thompson *et al.*, “Electrochemical window of the li-ion solid electrolyte li7la3zr2o12,” *ACS Energy Letters*, vol. 2, no. 2, pp. 462–468, 2017.

[61] W. D. Richards, L. J. Miara, Y. Wang, J. C. Kim, and G. Ceder, “Interface stability in solid-state batteries,” *Chemistry of Materials*, vol. 28, no. 1, pp. 266–273, 2016.

[62] A. Vasileiadis, “Modeling electrode materials,” en, *repository.tudelft.nl*, 2018. DOI: `10.4233/3a0da462-b912-4a60-9ff3-6f66b2cd0884`. [Online]. Available: `https://doi.org/10.4233/3a0da462-b912-4a60-9ff3-6f66b2cd0884`.

[63] D. S. Sholl and J. A. Steckel, *Density functional theory: a practical introduction.* 2022.

[64] W. Kohn and L. J. Sham, “Self-consistent equations including exchange and correlation effects,” *Physical review*, vol. 140, no. 4A, A1133, 1965.

[65] R. Iftimie, P. Minary, and M. E. Tuckerman, “Ab initio molecular dynamics: Concepts, recent developments, and future trends,” *Proceedings of the National Academy of Sciences*, vol. 102, no. 19, pp. 6654–6659, 2005. DOI: `10.1073/pnas.0500193102`. [Online]. Available: `https://www.pnas.org/doi/abs/10.1073/pnas.0500193102`.

[66] D. Frenkel and B. Smit, *Understanding molecular simulation: from algorithms to applications.* 2023.

[67] R. P. Feynman, “Forces in molecules,” *Physical review*, vol. 56, no. 4, p. 340, 1939.

[68] T. Ma *et al.*, “High-areal-capacity and long-cycle-life all-solid-state battery enabled by freeze drying technology,” *Energy & Environmental Science*, vol. 16, no. 5, pp. 2142–2152, 2023.

[69] N. A. Khoa *et al.*, “Synthesis of a li3- xincl6- x solid electrolyte and its application in all-solid-state batteries,” *Solid State Ionics*, vol. 421, p. 116 792, 2025.

[70] S. Luo *et al.*, “Growth of lithium-indium dendrites in all-solid-state lithium-based batteries with sulfide electrolytes,” *Nature communications*, vol. 12, no. 1, p. 6968, 2021.

[71] H. Pan *et al.*, “Carbon-free and binder-free li-al alloy anode enabling an all-solid-state li-s battery with high energy and stability,” *Science Advances*, vol. 8, no. 15, eabn4372, 2022.

[72] A. C. Lazanas and M. I. Prodromidis, “Electrochemical impedance spectroscopy a tutorial,” *ACS Measurement Science Au*, vol. 3, no. 3, pp. 162–193, 2023.

[73] BioLogic, *What is electrochemical impedance spectroscopy (eis)?* 2025. [Online]. Available: `https://www.biologic.net/topics/what-is-eis/`.

[74] S. Siracusano, S. Trocino, N. Briguglio, V. Baglio, and A. S. Aricò, "Electrochemical impedance spectroscopy as a diagnostic tool in polymer electrolyte membrane electrolysis," *Materials*, vol. 11, no. 8, p. 1368, 2018.

[75] M. S. Grewal, K. Kisu, S.-i. Orimo, and H. Yabu, "Increasing the ionic conductivity and lithium-ion transport of photo-cross-linked polymer with hexagonal arranged porous film hybrids," *Iscience*, vol. 25, no. 9, 2022.

[76] BioLogic, *Protocols for studying intercalation electrodes materials : Part i: Galvanostatic cycling with potential limitation (gcpl)*, 2005. [Online]. Available: `https://www.biologic.net/wp-content/uploads/2019/08/gitt_electrochemistry-battery-an1.pdf`.

[77] G. F. Harrington and J. Santiso, "Back-to-basics tutorial: X-ray diffraction of thin films," *Journal of Electroceramics*, vol. 47, no. 4, pp. 141–163, 2021.

[78] W. H. Bragg and W. L. Bragg, "The reflection of x-rays by crystals," *Proceedings of the Royal Society of London. Series A, Containing Papers of a Mathematical and Physical Character*, vol. 88, no. 605, pp. 428–438, 1913.

[79] A. Guinier, *X-ray diffraction: in crystals, imperfect crystals, and amorphous bodies.* 2013.

[80] A. Le Bail, H. Duroy, and J. L. Fourquet, "Ab-initio structure determination of lisbwo6 by x-ray powder diffraction," *Materials Research Bulletin*, vol. 23, no. 3, pp. 447–452, 1988.

[81] B. H. Toby and R. B. Von Dreele, "Gsas-ii: The genesis of a modern open-source all purpose crystallography software package," *Applied Crystallography*, vol. 46, no. 2, pp. 544–549, 2013.

[82] K. Momma and F. Izumi, *VESTA: Visualization for Electronic and Structural Analysis*, *Computer software*, Version 3, 2011. [Online]. Available: `https://jp-minerals.org/vesta/en/`.

[83] G. Kresse and J. Furthmüller, *VASP: Vienna Ab-initio Simulation Package*, *Computer software*, Version 6.4.0, 2024. [Online]. Available: `https://www.vasp.at`.

[84] J. P. Perdew *et al.*, "Restoring the density-gradient expansion for exchange in solids and surfaces," *Phys. Rev. Lett.*, vol. 100, p. 136 406, 13 Apr. 2008. DOI: `10.1103/PhysRevLett.100.136406`. [Online]. Available: `https://link.aps.org/doi/10.1103/PhysRevLett.100.136406`.

[85] J. P. Perdew, K. Burke, and M. Ernzerhof, "Generalized gradient approximation made simple," *Phys. Rev. Lett.*, vol. 77, pp. 3865–3868, 18 Oct. 1996. DOI: `10.1103/PhysRevLett.77.3865`. [Online]. Available: `https://link.aps.org/doi/10.1103/PhysRevLett.77.3865`.

[86] P. E. Blöchl, "Projector augmented-wave method," *Phys. Rev. B*, vol. 50, pp. 17 953–17 979, 24 Dec. 1994. DOI: `10.1103/PhysRevB.50.17953`. [Online]. Available: `https://link.aps.org/doi/10.1103/PhysRevB.50.17953`.

[87] S. Zhang, J. Ma, S. Dong, and G. Cui, "Designing all-solid-state batteries by theoretical computation: A review," *Electrochemical Energy Reviews*, vol. 6, no. 1, p. 4, 2023.

[88] Z. Wang, *VASPkit: A Pre- and Post-Processing Program for VASP Code*, *Computer software*, Version 1.2.0, 2021. [Online]. Available: `https://github.com/wangzhiw/vaspkit`.

[89] S. Nosé, "A unified formulation of the constant temperature molecular dynamics methods," *The Journal of chemical physics*, vol. 81, no. 1, pp. 511–519, 1984.

[90] W. G. Hoover, "Canonical dynamics: Equilibrium phase-space distributions," *Physical review A*, vol. 31, no. 3, p. 1695, 1985.

[91] V. Azizi, S. Smeets, A. K. Lavrinenko, and S. Ciarella, *GEMDAT: Geochemical Data Analysis Tool*, *Computer software*, Version 1.4, 2024. DOI: `10.5281/zenodo.10683188`. [Online]. Available: `https://zenodo.org/records/10683188`.

[92] S. P. Ong *et al.*, *Pymatgen: Python Materials Genomics*, *Computer software*, Version 2023.7.25, 2013. [Online]. Available: `https://pymatgen.org`.

[93] Y. Wu *et al.*, "Innovative doping strategies for li2zrcl6 solid electrolytes: A first-principles approach," *Journal of Energy Storage*, vol. 107, p. 115 017, 2025.

[94] P. Molaiyan *et al.*, "Investigation of the structure and ionic conductivity of a li3incl6 modified by dry room annealing for solid-state li-ion battery applications," *Materials & Design*, vol. 227, p. 111 690, 2023.

[95] C. Wang *et al.*, "New insights into aliovalent substituted halide solid electrolytes for cobalt-free all-solid state batteries," *Energy & Environmental Science*, vol. 16, no. 11, pp. 5136–5143, 2023.

[96] P. Vanysek, "Electrochemical series," *CRC handbook of chemistry and physics*, vol. 8, pp. 8–33, 2000.

[97] T. Ungar, "Microstructural parameters from x-ray diffraction peak broadening," *Scripta Materialia*, vol. 51, no. 8, pp. 777–781, 2004.

[98] H. Kwak *et al.*, "Na2zrcl6 enabling highly stable 3 v all-solid-state na-ion batteries," *Energy Storage Materials*, vol. 37, pp. 47–54, 2021.

[99] X. Li *et al.*, "Air-stable li 3 incl 6 electrolyte with high voltage compatibility for all-solid-state batteries," *Energy & Environmental Science*, vol. 12, no. 9, pp. 2665–2671, 2019.

[100] X. Li *et al.*, "Origin of superionic li3y1–x in x cl6 halide solid electrolytes with high humidity tolerance," *Nano letters*, vol. 20, no. 6, pp. 4384–4392, 2020.

[101] H. Wang *et al.*, "Electrochemically stable li3–x in1–x hf x cl6 halide solid electrolytes for all-solid-state batteries," *ACS Applied Materials & Interfaces*, vol. 15, no. 4, pp. 5504–5511, 2023.

[102] A. Banik, T. Famprikis, M. Ghidiu, S. Ohno, M. A. Kraft, and W. G. Zeier, "On the underestimated influence of synthetic conditions in solid ionic conductors," *Chemical science*, vol. 12, no. 18, pp. 6238–6263, 2021.

[103] C.-M. Wang, C.-H. Hsu, J.-S. Yang, and P.-C. Tsai, "Ab initio study on lithium anode interface instability and stabilization of superionic li3incl6 and li6ps5cl solid electrolytes," *Journal of Power Sources*, vol. 640, p. 236 719, 2025.

[104] H. F. Haneef, A. M. Zeidell, and O. D. Jurchescu, "Charge carrier traps in organic semiconductors: A review on the underlying physics and impact on electronic devices," *Journal of Materials Chemistry C*, vol. 8, no. 3, pp. 759–787, 2020.

[105] M. Daya, *Periodic table*, 2024. [Online]. Available: `https://ptable.com/`.

[106] S.-H. Lee, D.-S. Kang, S.-M. Lee, and J.-S. Roh, "X-ray diffraction analysis of the effect of ball milling time on crystallinity of milled polyacrylonitrile-based carbon fiber," *Carbon letters*, vol. 26, pp. 11–17, 2018.

[107] Q. Wang, Z. Shen, P. Du, Y. Zhou, P. Zhang, and Y. Liu, "New advances in solid-state electrolytes: From halides to oxyhalides," *Inorganic Chemistry Frontiers*, 2024.

A

Appendix: supporting information

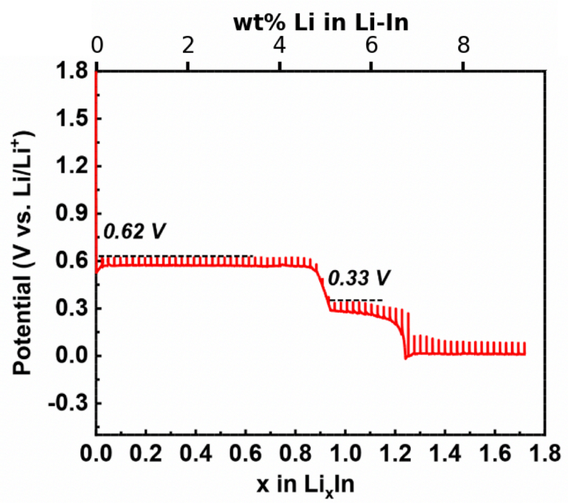

Figure A.1: Galvanostatic intermittent titration technique profile for lithiation on In foil. For various lithium concentrations x in Li$_x$In a constant current pulse of 0.2 mA cm^{-2} was applied for 1 hour, followed by a rest period of 1 hour during which the system relaxes towards equilibrium. During both phases, the potential against Li/Li$^+$ is recorded. It was found that when x $<$ 0.85 in Li$_x$In–equaling 5.9 wt% lithium–the potential of Li$_x$In stabilized at 0.62 V vs. Li/Li$^+$. Adapted from Pan *et al.* [71].

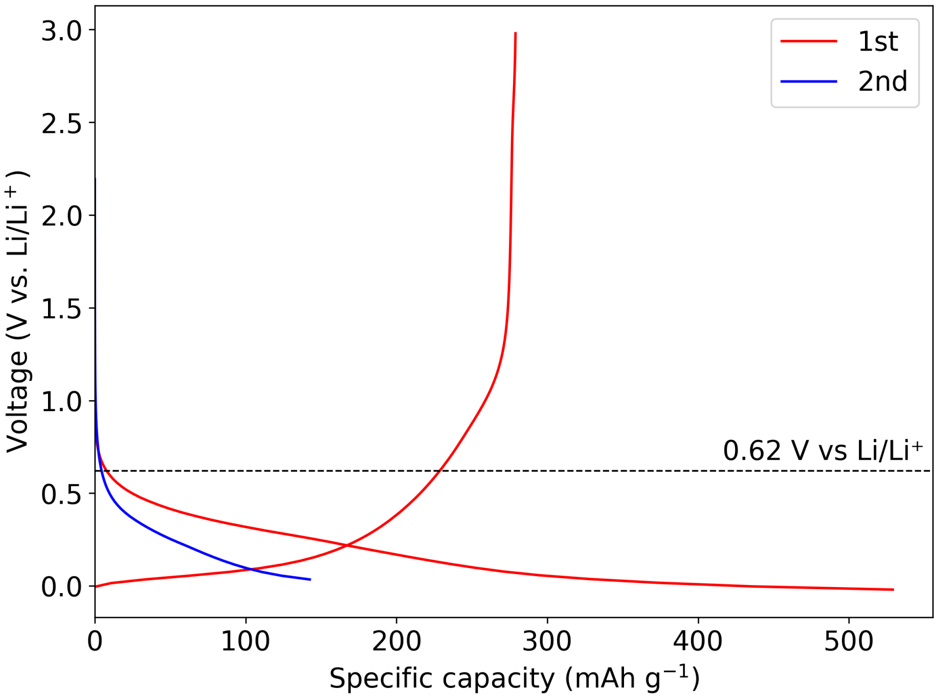

Figure A.2: Galvanostatic cycling profile of VGCF. Negligible capacity is observed above 0.62 V–the lowest cut-off voltage applied in this study during cycling–indicating that VGCF does not significantly contribute to observed half-cell capacity.

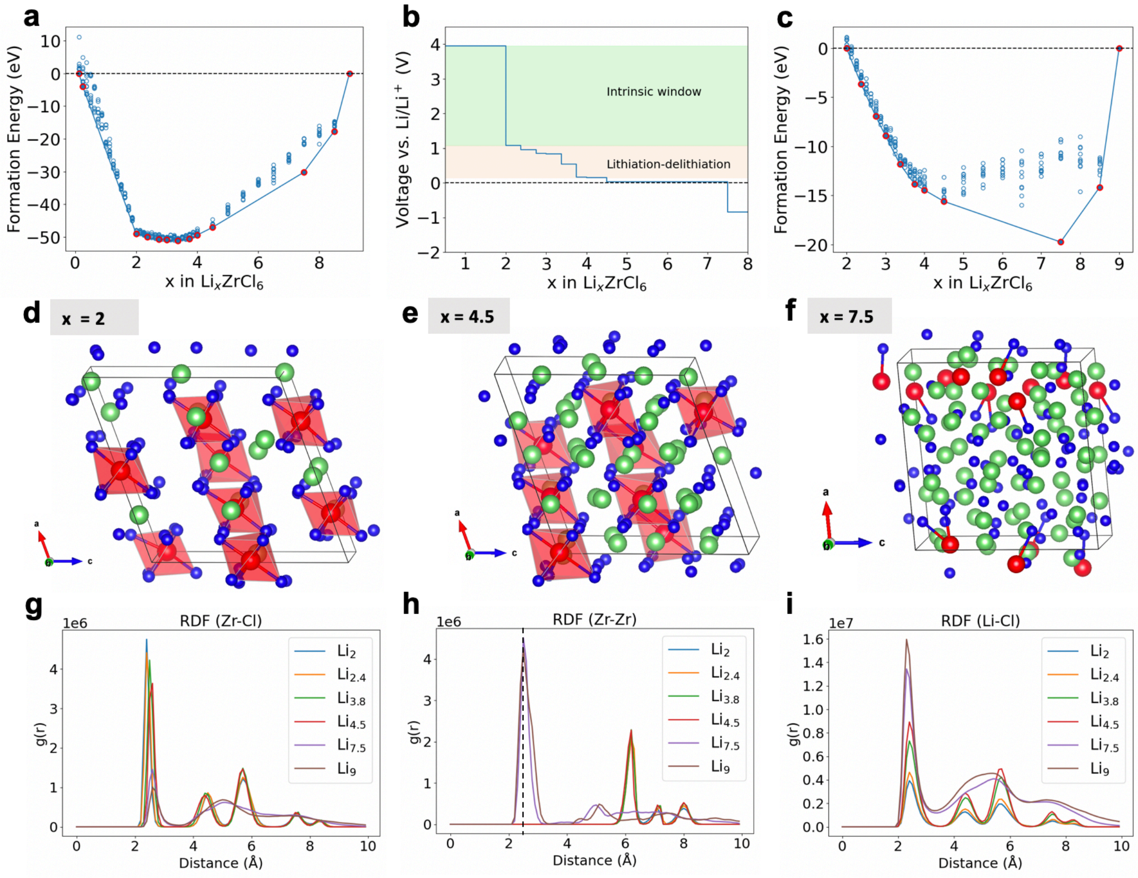

Figure A.3: Stability window of LZC with full occupation of the *2a* position as defined by DFT and MD calculations. a, Formation energies of Li_xZrCl_6 with respect to the completely delithiated and lithiated states. The convex line follows the lowest energy path–indicating the stable configurations along the range. **b,** Corresponding voltage profile indicating the intrinsic window and lithiation-delithiation region, where lithium insertion is possible without destroying the monoclinic structure. **c,** The reduction part of the convex hull, where Li_2ZrCl_6 and Li_9ZrCl_6 are taken as references. **d-f,** Configurations after a 100 ps AIMD simulation at 400 K of the **(d)** unlithiated Li_2ZrCl_6 compound, **(e)** $Li_{4.5}ZrCl_6$ compound in the lithiation-delithiation region, and **(f)** $Li_{7.5}ZrCl_6$ that shows structural decomposition. **g-i** Radial distribution frequency plots from 100 ps AIMD simulations at 400 K comparing **(g)** Zr-Cl, **(h)** Zr-Zr, and **(i)** Li-Cl distances.

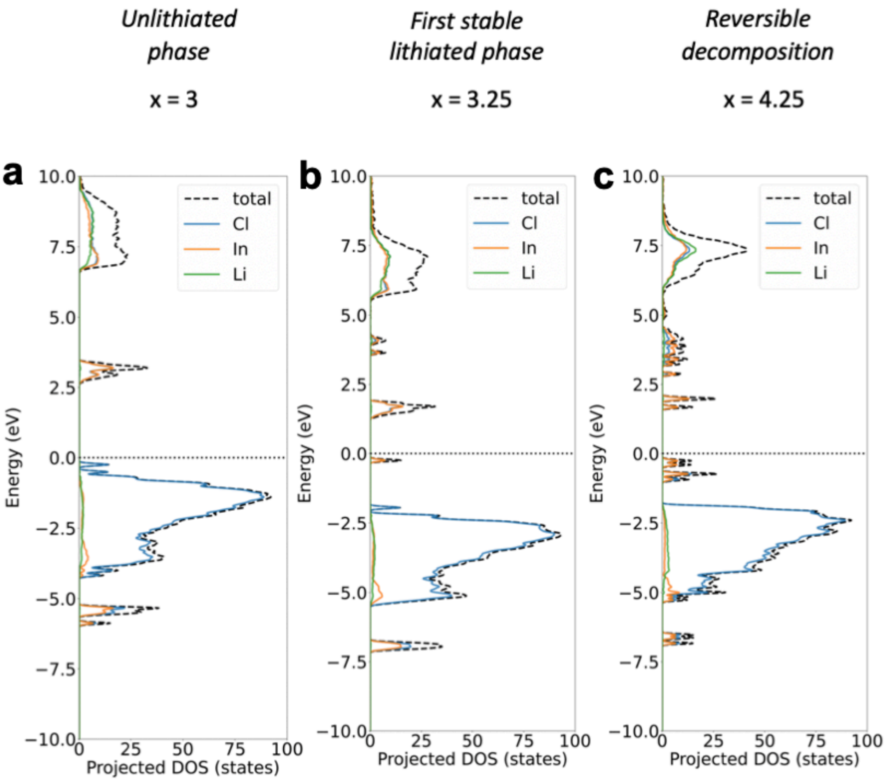

Figure A.4: Projected density of states of LIC at various lithiation levels. The DOS is plotted by element, with the Fermi level set to zero. **a,** Unlithiated phase Li_3InCl_6, showing a respectable bandgap of 2.5 eV without trap states. **b,** $Li_{3.25}InCl_6$, the first stable reduced phase, where indium introduces trap states in the middle of the bandgap that facilitate the reduction of indium. **c,** $Li_{4.25}InCl_6$, the phase formed at 1.4 V where reversible decomposition has been observed experimentally. Indium contributes more filled states.

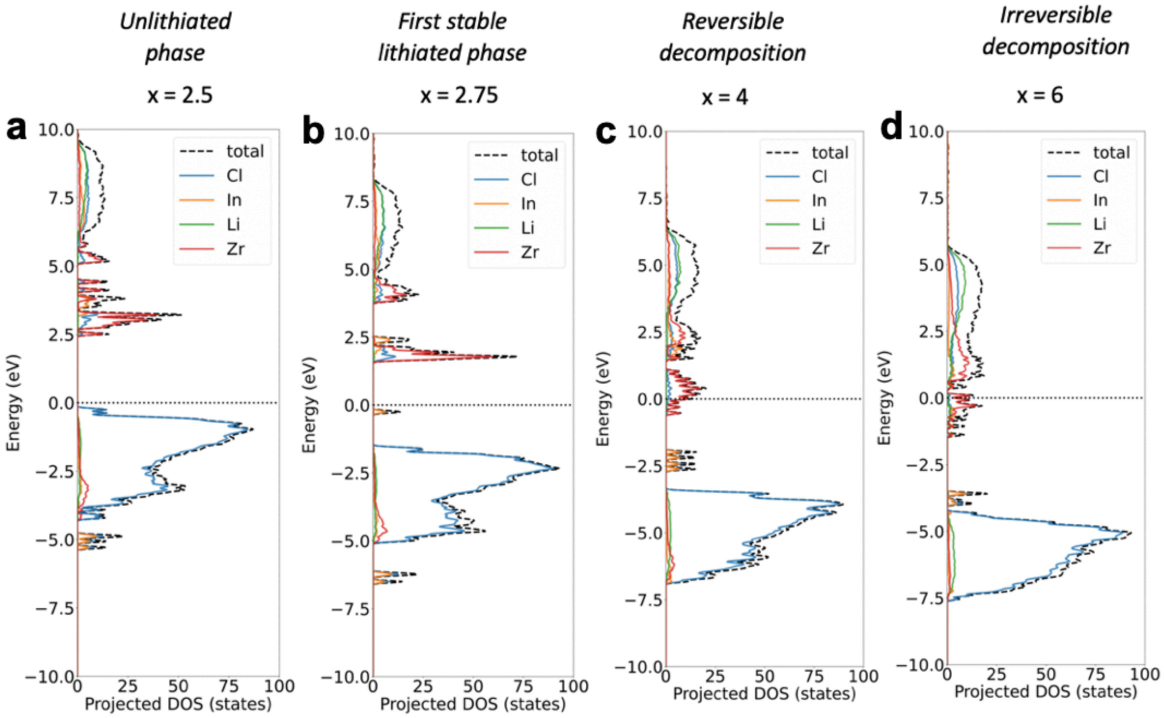

Figure A.5: Projected density of states of LIZC at various lithiation levels. The DOS is plotted by element, with the Fermi level set to zero. **a,** Unlithiated phase $Li_{2.5}In_{0.5}Zr_{0.5}Cl_6$, showing a respectable bandgap of 2.5 eV without trap states. **b,** $Li_{2.75}In_{0.5}Zr_{0.5}Cl_6$, the first stable reduced phase, where indium introduces localised trap states in the middle of the bandgap that facilitate the reduction of indium. **c,** $Li_4In_{0.5}Zr_{0.5}Cl_6$, the phase formed at 1.4 V where reversible decomposition has been observed experimentally. Indium contributes more filled states and zirconium d-orbitals become more available around the Fermi-energy level. **d,** $Li_6In_{0.5}Zr_{0.5}Cl_6$, the phase formed at 0.6 V where irreversible decomposition has been observed experimentally.

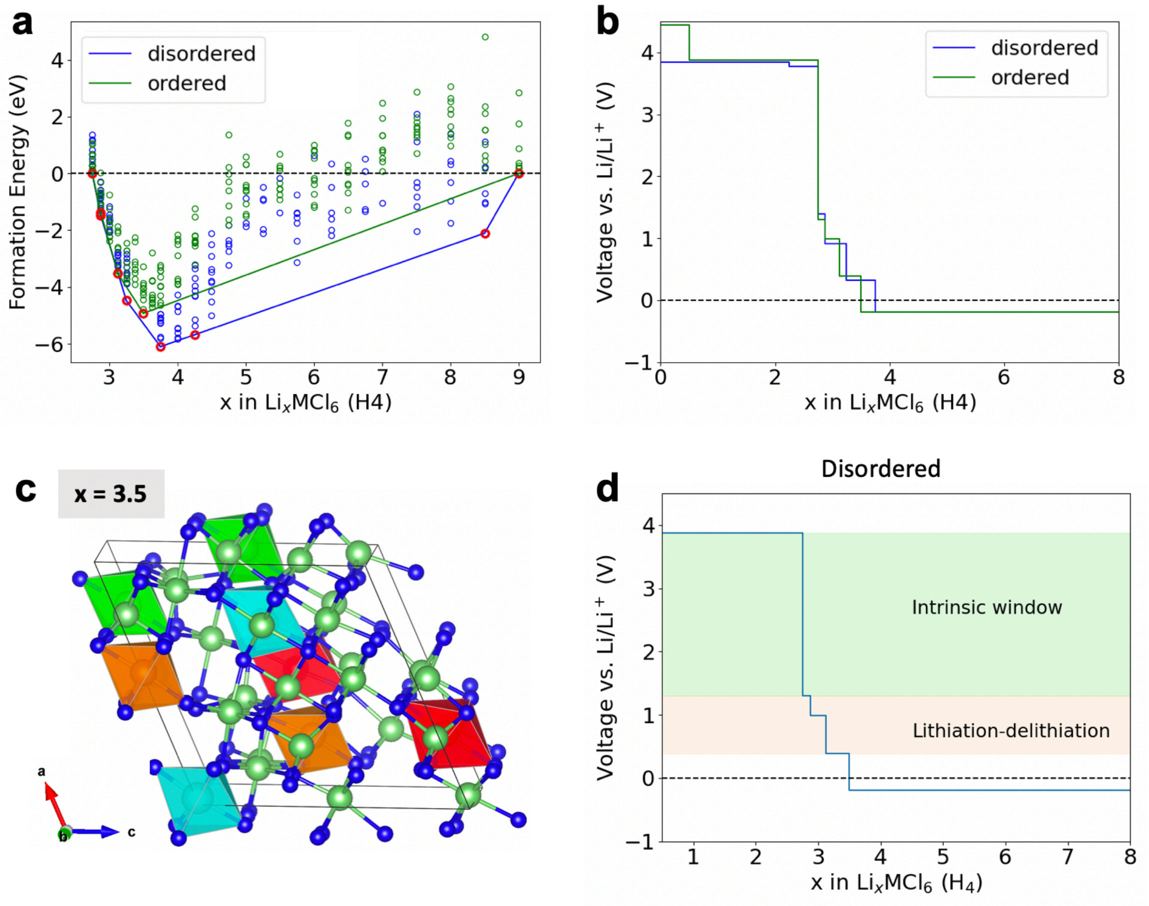

Figure A.6: Impact of cation disorder on the electrochemical stability window of H4. In the ordered configuration, all metal cations occupy the *2a* Wyckoff positions, while in the disordered variant, one metal cation is placed in the *4g* position. **a,** Formation energies of the ordered and disordered structures, referenced to $Li_{2.75}MCl_6$ and Li_9MCl_6. **b,** Corresponding voltage profiles of the ordered and disordered configurations. **c,** Configuration of the $Li_{3.5}MCl_6$ phase formed at 0.3 V, obtained after a 100 ps AIMD simulation, showing no signs of structural decomposition. **d,** Corresponding voltage profile of the ordered structure, marking the intrinsic stability window and a lithiation-delithiation region where lithium insertion is possible without destroying the monoclinic structure.

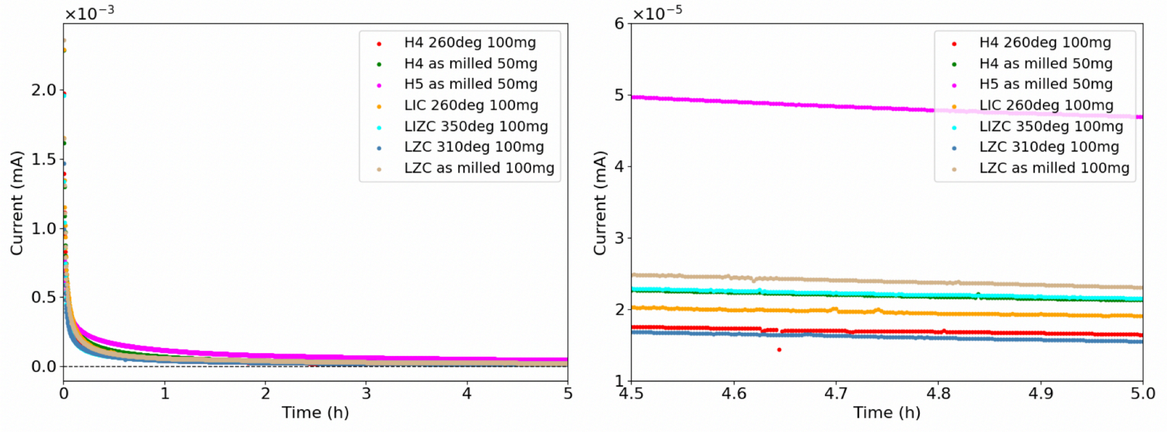

Figure A.7: DC polarisation measurements of studied halide electrolytes. A constant potential of 2.5 V was applied and the steady-state current after 5 hours was used to estimate electronic conductivity. The right figure provides a magnified view of the stabilised current region

Table A.1: Calculated electronic conductivities of studied halide electrolytes. Electronic conductivity (σ_e) values were estimated by applying applying Equation 3.2, using the steady-state current measured after 5 hours during DC polarisation, a potential of 2.5 V, and an area of 0.785 cm^2.

Compound	Mass [mg]	Thickness [mm]	Current [mA]	σ_e [S/cm]
H4 260 °C	100	0.74	1.71×10^{-5}	4×10^{-10}
H4 as-milled	50	0.36	2.1×10^{-5}	2×10^{-10}
H5 as-milled	50	0.37	4.7×10^{-5}	5×10^{-10}
LIC 260 °C	100	0.58	1.9×10^{-5}	5×10^{-10}
LIZC 350 °C	100	0.61	2.2×10^{-5}	4×10^{-10}
LZC 310 °C	100	0.53	1.5×10^{-5}	3×10^{-10}
LZC as-milled	100	0.58	2.3×10^{-5}	4×10^{-10}

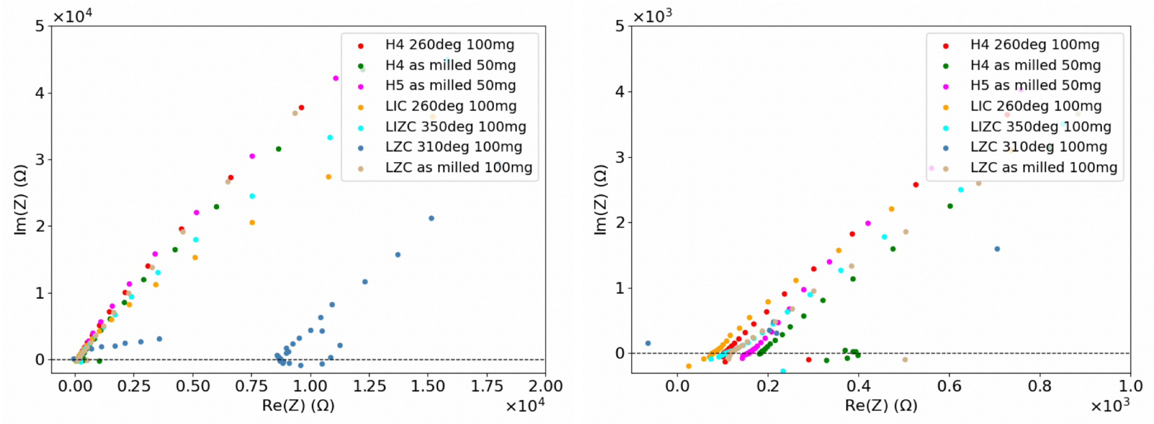

Figure A.8: The Nyquist plots of studied halide electrolytes. Frequency is swept from 7 MHz through 100 mHz with an AC amplitude of 10 mV. The figures provide a magnified view to show the low-voltage x-intercept of the least conductive compound (left) and more conductive compounds (right).

Table A.2: Calculated ionic conductivities of the studied halide electrolytes. Ionic conductivity values were estimated by means of Equation 3.1, taking the resistance as the x-intercept from the Nyquist plot in Figure A.8.

Compound	Mass [mg]	Thickness [mm]	R [Ω]	σ_i [mS/cm]
H4 260 °C	100	0.74	102	0.9
H4 as-milled	50	0.36	185	0.3
H5 as-milled	50	0.37	157	0.3
LIC 260 °C	100	0.58	77	0.9
LIZC 350 °C	100	0.61	105	0.7
LZC 310 °C	100	0.53	8734	0.01
LZC as-milled	100	0.58	117	0.6

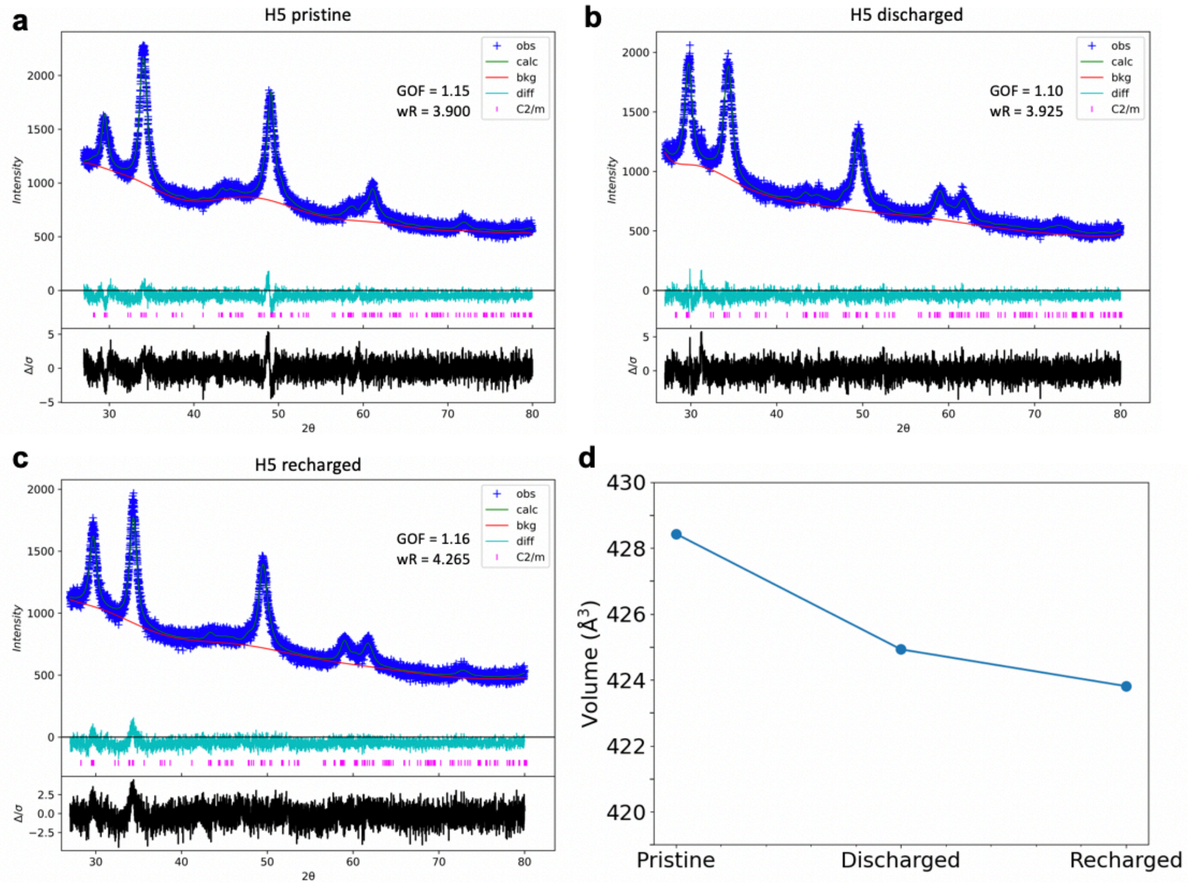

Figure A.9: Le Bail refinement results of H5 at different states of charge. a-c, Le Bail refinement of H5 in **(a)** the pristine state, **(b)** after discharge to 0.6 V, and **(b)** after recharging after 5 cycles. **d,** Volume of the unit cell of H5 at different states of charge.

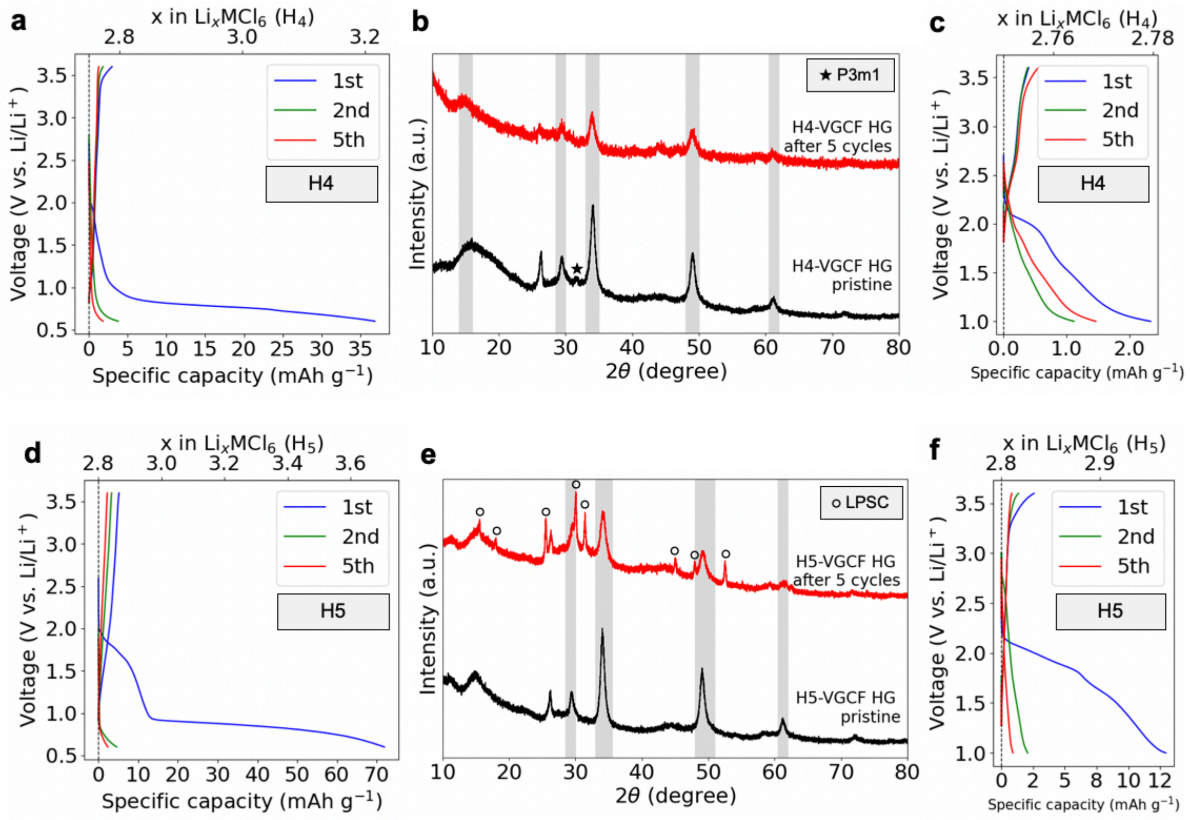

Figure A.10: Galvanostatic cycling behaviour of high-entropy compounds handground with VGCF. The Li_xMCl_6 compounds were handground with VGCF in a 5:1 ratio for 10 minutes. Half-cells were cycled at a current of 200 μA = 255 μA/cm^2 = 6.7 mA/g. **a,d** Voltage profiles during galvanostatic cycling between 0.6 and 3.6 V for the **(a)** H4 and **(d)** H5 compound, showing the first, second and fifth cycles. **b,e** X-ray diffraction patterns of the pristine sample, and the recharged sample after 5 cycles down to 0.6 V for the **(b)** H4 and **(d)** H5 compound. **c,f** Voltage profiles during galvanostatic cycling between 1.0 and 3.6 V for the **(c)** H4 and **(f)** H5 compound

Figure A.10a,d shows that the hand-ground samples of both H4 and H5 exhibit non-reversible cycling behaviour, retaining virtually no capacity during the first cycle. This remains true even when the discharge cutoff voltage is slightly raised to 1.0 V–just prior to the distinct voltage plateau at 0.9 V (Figure A.10c,f). Nevertheless, the XRD patterns of the hand-ground samples show no discernable difference between the pristine, and post-cycled samples, apart from distinct peaks stemming from argyrodite contamination. The same irreversible behaviour was however observed for LIC that was mixed at 150 rpm instead of 400 rpm. A plausible explanation for this is that hand-grinding the halide with VGCF limits interface area between VGCF and Li_xMCl_6, which introduces transport limitations that kinetically hinder electrochemical activity of the cathode. As a result, no significant phase changes are detectable by means of XRD.